Aalborg University

Design of Mechanical Systems - Master's Thesis

Kristian Hansen

Asymptotic analysis of acoustic black holes in cylindrical shells

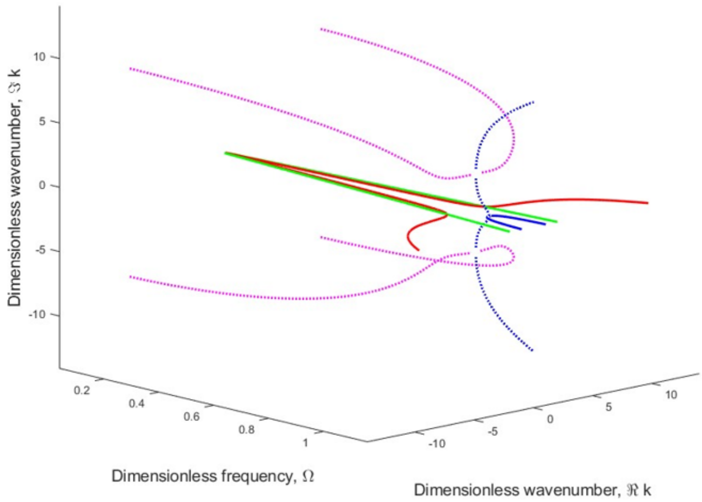

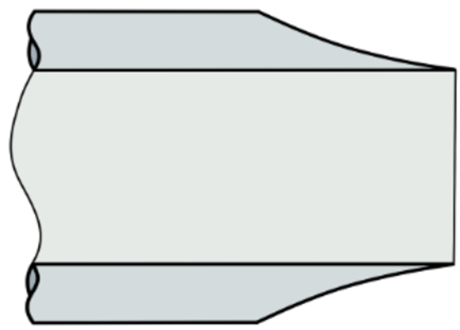

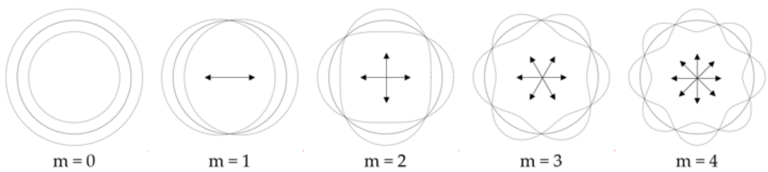

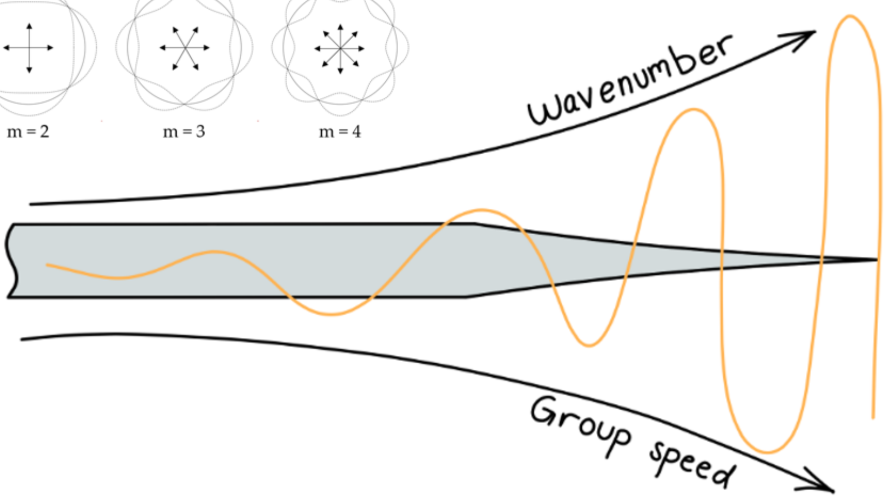

Faculty of Engineering and Science
Materials and Production
Fibigerstræde 14
9220 Aalborg Øst
Denmark

Title:

Asymptotic analysis of acoustic black holes in cylindrical shells

Project:

Design of Mechanical Systems - Master's Thesis
Mechanical Engineering & Manufacturing

Project period:

1. Feb 2022 - 16. Jun 2022

Author:

Kristian Hansen

Supervisor:

Sergey V. Sorokin

Total number of pages: 60
Number of report pages: 73

Synopsis:

Throughout this thesis, the acoustic black hole effect is investigated for cylindrical shells, using a theoretical, analytical, and academically motivated approach through the framework of thin shell theory. Asymptotic solutions to the dispersion equation for the cylindrical shell are obtained, and the acoustic black hole effect is investigated through numerical evaluation of the reflection coefficient and through the divergent nature of the anti-derivative of the asymptotic wavenumber expression. A hierarchy of models is investigated, including simple Bernoulli Euler beams, flat plates, curved plates, beams on Winkler foundations, and of course the full cylindrical shell. It is shown, that there is an analytical basis for the acoustic black hole effect in cylindrical shells and that the effect can be obtained in a similar manner as for beams and plates. An interesting property of the cylindrical shell is, however, that the effect should not be expected in the low-frequency range, even if a termination profile could be designed, resulting in sufficiently low Normalized Wave number Variation at lower frequencies.

Preface

Throughout my time at Aalborg University, I have been fascinated by the intricacies of structural vibrations and the potential for innovation in this field. The phenomena we observe are just the right balance between intuitive and absolute magic, and I am repeatedly amazed by the ways in which the behaviour of vibrating structures can be understood and harnessed for practical applications. From designing acoustic metamaterials to creating new musical instruments, the possibilities seem endless. I look forward to continuing to explore this fascinating area of study and contributing to the ongoing advancement of structural vibration research.

This report is a result of a Master's Thesis, written in the fourth and final semester of "Design of Mechanical Systems" (DMS) at Aalborg University. All figures in the report are created by the Author. References are indicated by square brackets [#] and are listed in the Bibliography at the back of the report in order of appearance. Equations are indicated by parenthesis (#). Appendices are indicated by letters and appear at the back of the report. An extensive nomenclature list can be found for each chapter on page vi.

Special thanks to Lasse Søgaard Ledet, Head of Electronics Design & Simulation at Grundfos, for his supervision during the project.

Kristian Hansen

Kristian Hansen

Summary

The project begins with an introductory examination of the acoustic black hole effect for a simple Bernoulli Euler waveguide. It is explained how the effect is obtained from a gradual reduction of the flexural rigidity of the waveguide, typically through a gradual reduction of thickness. It is explained how the mathematical model is based on assumptions related to how slowly the reduction should occur, and how a too abrupt reduction in thickness violates the model validity. It is explained how for the idealized case where the thickness of the waveguide is reduced to zero, the acoustic black hole effect can be investigated through the divergent nature of the anti-derivative of the wavenumber. For a more realistic case where a residual height is present at the tip of the acoustic black hole, a numerically evaluated reflection coefficient can be used to assess the performance of the acoustic black hole.

The cylindrical shell model is introduced and briefly explained. The dispersion equation for the shell is derived and acts as the point of departure for the subsequent acoustic black hole analysis, which is split into three separate analyses of the breathing mode ($m = 0$), the bending mode ($m = 1$) and finally the ovalling mode ($m = 2$). The analysis of these modes is performed in three steps: First, a numerical solution is obtained for the dispersion equation. Secondly, low-frequency asymptotic solutions are obtained for the purely real-valued parts of the individual dispersion branches. Thirdly, the asymptotic wave number solutions are investigated for the acoustic black hole effect. The acoustic black hole effect is not observed from this initial low-frequency analysis for any m-spectrum.

To gain a better understanding of why the effect seemed to be absent in the low-frequency range of the cylindrical shell, a more rigorous investigation is conducted, by investigating the underlying differential equations of different models, where the effect is known to be present. The analysis starts from a simple flat plate carrying flexural waves, and it is shown how the effect can be obtained for this geometry. A model of a curved plate is investigated next, and it is found that the effect is absent in this case. It is attempted to identify which differences in the differential equations may cause the effect to be present in one case, and absent in the other. It is shown how the effect can be obtained in the low-frequency range for the curved plate (and cylindrical shell) in the breathing mode if Poisson effects are neglected. It is also attempted to make the effect appear in the bending- and ovalling mode of the cylindrical shell, by the introduction of material- and kinematic assumptions, but this is not successful. To investigate why this was not successful, a modal-coefficient analysis is performed. This shows how the flexural-dominated wave in the cylindrical shell also exhibits substantial longitudinal motion in the low-frequency range. This longitudinal motion diminishes with increasing frequency, which inspires the effort to obtain a high-frequency solution for the flexural wave numbers in the model with imposed material- and kinematic assumptions. The high-frequency solution shows the acoustic black hole effect to be obtainable. The analysis then returns to the original cylindrical shell, with no material- nor kinematic assumptions. Again, modal-coefficient analysis is performed and it is found that here the flexural-dominated wave also exhibits substantial longitudinal motion in the low-frequency range, which again diminishes with increasing frequency. A high-frequency solution is found for the flexural wave numbers of the cylindrical shell, and it is shown how the acoustic black hole effect is obtainable in this frequency range, for any m-spectrum, when employing a power-law termination profile with power $n \geq 2$. As a final investigation, the acoustic black hole effect is investigated for waves propagating in the circumferential direction of the cylindrical shell. Here it is found that the effect is also present when employing a power-law termination profile with power $n \geq 2$.

Nomenclature

Abbreviations

SRQ	-	Sub-Research Question
MRQ	-	Main-Research Question
WKB	-	Wentzel–Kramers–Brillouin
NWV	-	Normalized Wave number Variation

Chapter 3

h_0	[m]	-	Height of beam outside termination profile
x_E	[m]	-	abscissa of the acoustic black hole
$h(x)$	[m]	-	x-dependent height defining termination profile
E	[Pa]	-	Young's Modulus
I	$[m^4]$	-	Area moment of inertia
x	[m]	-	Position along beam
w	[m]	-	Lateral deflection of beam
ρ	[kg/m^3]	-	Material density of beam
A	$[m^2]$	-	Area of beam
t	[s]	-	Time
k_x	$[m^{-1}]$	-	Dimensional wave number
i	[-]	-	Imaginary unit
ω	$[s^{-1}]$	-	Dimensional angular frequency
ϵ	[-]	-	Constant driving length of power-law termination profile
n	[-]	-	Exponent constant driving shape of power-law termination profile
h_r	[m]	-	Residual height at tip of termination profile
E_0	[Pa]	-	Nominal real-valued Young's Modulus
η	[-]	-	Complex proportion of Young's Modulus
R	[-]	-	Reflection Coefficient
k	[-]	-	Dimensionless wave number
Ω	[-]	-	Dimensionless Frequency

Chapter 4

m	[-]	-	Circumferential wavenumber
x	[m]	-	Position along shell
θ	[-]	-	Angular position on shell
E	[Pa]	-	Young's Modulus
ν	[-]	-	Poisson's ratio
ρ	[kg/m^3]	-	Material density of shell
u_m	[m]	-	Longitudinal motion of shell mid-plane
v_m	[m]	-	Circumferential motion of shell mid-plane
w_m	[m]	-	Radial motion of shell mid-plane
L	[m]	-	Length of shell
R_0,R	[m]	-	Mid-plane radius outside acoustic black hole
h_0,h	[m]	-	Shell thickness outside acoustic black hole
i	[-]	-	Imaginary unit
ω	[s^{-1}]	-	Dimensional angular frequency
A_j	[-]	-	Modal amplitudes $j = 1, 2, 3$
L_{ij}	[-]	-	Matrix representation of equations
k_x	[m^{-1}]	-	Dimensional wave number
k	[-]	-	Dimensionless wave number
Ω	[-]	-	Dimensionless Frequency
t	[-]	-	Dimensionless thickness parameter
c_L	[m/s]	-	Longitudinal wave speed
λ_L	[m]	-	Longitudinal wave length
f	[s^{-1}]	-	Frequency
$\bar{k}$	[-]	-	Asymptotic approximation of dimensionless wave number
x_i	[-]	-	Expansion constant $i = 0, 1...$
p_i	[-]	-	Expansion exponent $i = 0, 1...$
ϵ	[-]	-	Constant driving length of power-law termination profile
n	[-]	-	Exponent constant driving shape of power-law termination profile
h_r	[m]	-	Residual height at tip of termination profile
c_p	[-]	-	Dimensionless phase speed
c_g	[-]	-	Dimensionless group speed
E_0	[Pa]	-	Nominal real-valued Young's Modulus
η	[-]	-	Complex proportion of Young's Modulus
Ω_C	[-]	-	Dimensionless cut-on frequency
R_O	[m]	-	Outer radius of hollow cylindrical beam
R_I	[m]	-	Inner radius of hollow cylindrical beam
$R(x)$	[m]	-	Varying radius along termination profile
R_r	[m]	-	Residual radius at end of termination profile
α	[-]	-	Constant ratio between h and R

Chapter 5

W_w	[m]	-	Flexural motion of termination profile wedge
D_w	$[Nm^2]$	-	Flexural Rigidity of termination profile wedge
h_w	$[m]$	-	Height of termination profile wedge
ρ	[-]	-	Density of termination profile wedge
x	[m]	-	Lengthwise position along plate
y	[m]	-	Transverse position along plate
ν	[-]	-	Poisson's ratio
$B(x)$	[m]	-	Space dependent amplitude of solution ansatz
k_p	$[m^{-1}]$	-	Plate wavenumber
$S(x)$	[-]	-	X-dependent part of the eiconal function
k_y	$[m^{-1}]$	-	Wave number in the y-direction
i	[-]	-	Imaginary unit
E	[Pa]	-	Young's Modulus
ω	$[s^{-1}]$	-	Dimensional angular frequency
γ	[-]	-	Constant introduced for simple notation
t	[-]	-	Dimensionless thickness parameter
θ_0	[-]	-	Angular span of curved plate geometry
R_0,R	[m]	-	Mid-plane radius outside acoustic black hole
θ	[-]	-	Angular position on shell
u, v, w	[m]	-	Displacement components
m'	[-]	-	Circumferential wavenumber of curved plate
m	[-]	-	Circumferential wavenumber of cylindrical shell
k	[-]	-	Dimensionless wave number
Ω	[-]	-	Dimensionless Frequency
ϵ	[-]	-	Constant driving length of power-law termination profile
n	[-]	-	Exponent constant driving shape of power-law termination profile
L	[J]	-	Lagrangian
T_{SH}	[J]	-	Kinetic energy expression
U_{SH}	[J]	-	Potential energy expression
V_{SH}	[J]	-	External potential expression
ϵ_1	[-]	-	Axial strain
ϵ_2	[-]	-	Circumferential strain
$\bar{\omega}$	[-]	-	Shear strain
κ_1	$[m^{-1}]$	-	Bending curvature in axial direction
κ_2	$[m^{-1}]$	-	Bending curvature in circumferential direction
τ	$[m^{-1}]$	-	Twisting deformation
T_1	[N/m]	-	Axial membrane force
T_2	[N/m]	-	Circumferential membrane force
S	[N/m]	-	Shear force
M_1	[N]	-	Bending moment in axial direction
M_2	[N]	-	Bending moment in circumferential direction
H	[N]	-	Twisting moment
δ	[-]	-	Mathematical operator for first variation
t_1, t_2	[s]	-	Arbitrary boundaries for time integral
α	[m]	-	Constant ratio between h and R
Ω_C	[-]	-	Dimensionless cut-on frequency
x_i	[-]	-	Expansion constant $i = 0, 1...$
c_p	[-]	-	Dimensionless phase speed
c_g	[-]	-	Dimensionless group speed

Chapter 5: Continued

ξ	[-]	-	Modal coefficient
η	[-]	-	Re-scaling coefficient for frequency scaling approach
Ω_{rs}	[-]	-	Re-scaled dimensionless frequency
k_{rs}	[-]	-	Re-scaled dimensionless wave number
$\bar{k_{rs}}$	[-]	-	Asymptotic approximation of re-scaled dimensionless wave number
s	[-]	-	Index used to denote terms of different powers of dimensionless thickness parameter, t.

Appendix E

x	[-]	-	Non-scaled coordinate
X	[-]	-	Scaled coordinate
$f(x)$	[-]	-	Non-scaled function value at x
$F(X)$	[-]	-	Scaled function value at X
ϵ	[-]	-	Small parameter

Contents

1 Introduction

At some point during the design phase of any new machine or component, the engineer should asses the vibrational properties of his or her design. The engineer is then often forced to invest considerable effort in controlling the vibrations, often affecting the final product functionally and visually. Various methods have been used to control such mechanical vibrations, based on e.g. viscoelastic damping material, decoupling by using flexible mounts, periodicity effects, or by optimizing the design to move natural frequencies outside the operational frequency range [1]. In the last few decades, a new method is beginning to mature, namely, the *acoustic black hole*, promising to be a lightweight and efficient method for controlling structural vibrations [2, 3, 4, 5].

The term "acoustic black hole" refers to an analog of a black hole from relativistic physics. In physics, the term "black hole" refers to a singularity with such a great mass, that when anything, even light, comes too close, crossing the so-called event horizon, it is unable to escape again. An *acoustic* black hole is similar, as incoming vibrational energy is captured and (ideally) never re-released back into the structure. This allows the engineer to trap vibrational energy, at a controlled location in the structure. The acoustic black hole effect is commonly achieved, by gradually reducing the flexural rigidity of a waveguide, by a reduction of its thickness, or less commonly, by a gradual change in material properties. This in turn reduces the phase a group velocities of incoming flexural waves. For the limiting (albeit purely theoretical) case, where the flexural rigidity goes to zero, the waves are stopped never to be reflected back into the waveguide. The trapping of incoming waves in the acoustic black hole will cause the energy density to rise, which in turn results in a comparable increase in vibration amplitude. This acoustic black hole effect allows for remarkably efficient vibration mitigation, by placing a viscoelastic damping material on the acoustic black hole, to dissipate the trapped energy. The acoustic black hole effect has been investigated both analytically, experimentally, and numerically for plates and beams, see [2] and sources within. These models have provided the foundation, for exploiting the acoustic black hole effect in different mechanical systems e.g. aircraft wings [6] and turbofan blades [7]. If models of the acoustic black hole effect in cylindrical shells are developed, it would allow for the effect to be exploited in a large number of additional mechanical systems, such as piping systems, pumping stations, wastewater wells, bike frames, submarine pressure hulls, air-frames, drones, etc.

In the last couple of years, interest has begun to pick up, for the investigation of the acoustic black hole effect in cylindrical shells. In [8], the Gaussian Expansion Method is used to develop a foundation for efficient parametric analysis of annular acoustic black holes in cylindrical shells. Several configurations of acoustic black holes were investigated, showing a significant decrease in flexural vibrations compared to the uniform shell. The authors, Jie Deng Et Al., recognize that this study is only a first step, but shows the potential of the acoustic black hole effect in the context of cylindrical shells. To the knowledge of the Author, very limited (if any) analytical investigation of the acoustic black hole effect has been performed for cylindrical shells and the hope of this thesis is, to do exactly this. The thesis will act as an academically motivated investigation, of the acoustic black hole effect in a thin cylindrical shell model, through semi-analytical analysis of the dispersion equation using asymptotic approximations.

2 Problem statement

In this Chapter, the problem statement will be formulated. This will be done through the formulation of a Main Research Question (MRQ) which will then be split into three Sub Research Questions (SRQ), each of which will be answered in their respective chapters. In the introduction in Chapter 1, the concept of the acoustic black hole was described, and previous investigations of its applications in cylindrical shells were then briefly presented. From this, the Main Research Question can be formulated:

Main research question:
How can the acoustic black hole effect be modeled for elastic cylindrical shells, through the framework of thin shell theory?

In order to answer this MRQ, three SRQs are formulated as follows:

Sub Research Question #1
Getting acquainted with the acoustic black hole effect

How can the acoustic black hole effect be explained mathematically for simple waveguides like Bernoulli Euler beams, and what are the underlying assumptions? How can the performance of an acoustic black hole be quantified?

Sub Research Question #2:
Asymptotic acoustic black hole analysis of cylindrical shells

How can the acoustic black hole effect be modeled and investigated using asymptotic approximations, for a thin cylindrical shell model?

Sub Research Question #3:
Investigating the differential equations of motion

For which geometries does the acoustic black hole effect appear, and what causes the effect to be absent in some cases? Which assumptions can be employed to make the effect appear in the absent cases?

2.1 Delimitations

Delimitations have been made throughout the project, which are listed below. The list is by no means exhaustive but will be used as a natural point of departure for the discussion of potential future work after having answered the Main Research Question.

- **Delimitation 1: Industrial applicability**
  The thesis does not aim to develop acoustic black hole technology in cylindrical shells for industrial application. The thesis will act as an academically motivated analysis, not limited by the practicality of the model assumptions.
- **Delimitation 2: Experimental validation**
  No experiments have been made throughout the project, to validate the results obtained from the analysis of the acoustic black hole effect. On a few occasions, experimental work is referenced, but the Author makes an effort to point out, that all novel conclusions drawn in this thesis have no experimental backing.
- **Delimitation 3: Analysis through numerical models**
  Numerical investigation of the acoustic black hole effect is performed extensively using the Finite Element Method in literature. This thesis does not use such numerical analysis to investigate the effect or as a tool for supporting obtained results.
- **Delimitation 4: Investigation of thick shells**
  The thesis does not include an analysis of thick shells, neither in a geometrical nor acoustic sense.
- **Delimitation 5: Fluid loading**
  The thesis does not include the analysis of fluid-loaded shells, although many cylindrical shell structures used in industry are either submerged in, or filled with, fluid. In spite of this, the analysis will still be valid for cases where the fluid-structure interaction can be neglected.

3 SRQ 1: Getting acquainted with the acoustic black hole effect

In this chapter, SRQ 1 will be answered. In [9], the principle of the acoustic black hole was first described by M. A. Mironov, and in this chapter, the acoustic black hole effect will be investigated and described for a simple Bernoulli Euler beam following his example. This will serve as an introduction to the concepts, assumptions, and limitations of the model, and will act as a "plan of attack" for when the thin-walled elastic cylindrical shell will be analyzed in the later chapters. In Figure 3.1, the BE beam geometry is visualized, having an acoustic black hole termination at the right-hand side. The thickness of the beam outside the acoustic black hole is denoted h_0, and the shape of the acoustic black hole profile, henceforth called the termination profile, is defined by its instantaneous height, $h(x)$. It should be mentioned, that the figure is somewhat misleading compared to the mathematical modeling in this chapter. If one must be completely consistent, the thickness should be reduced symmetrically on both the top and bottom, so the neutral axis of the beam is in line with the tip of the acoustic black hole. It is however very typical for experimental investigations of the acoustic black hole effect, to use this type of asymmetric termination, as it simplifies the manufacturing substantially [2, 5, 10].

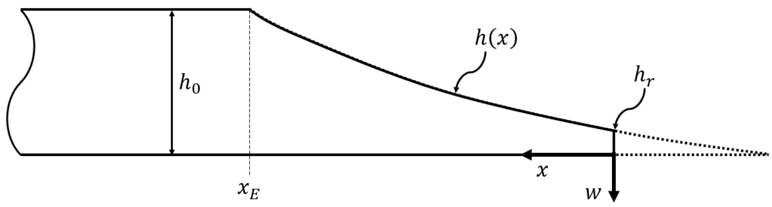

Figure 3.1: Acoustic black hole termination at the end of the beam waveguide. x_E is the abscissa of the start of the acoustic black hole, where it transitions into the homogeneous beam with height h_0. h_r is the residual height at the tip of the termination.

3.1 Acoustic black hole analysis: Mathematical model

The analysis will take point of departure in the differential equation of motion for a BE beam in bending (3.1). One can see how the usual assumption of constant flexural rigidity gives rise to the simple form, (3.2).

$$\frac{\partial^2}{\partial x^2}\left(EI\frac{\partial^2 w}{\partial x^2}\right) - \rho A\frac{\partial^2 w}{\partial t^2} = 0 \tag{3.1}$$

$$EI\frac{\partial^4 w}{\partial x^4} - \rho A\frac{\partial^2 w}{\partial t^2} = 0 \tag{3.2}$$

By the usual separation of variables and introduction of time and space harmonic solutions, one obtains the dispersion relation given as (3.3). The roots of the dispersion relation are given as (3.4). These solutions have the interesting property of dispersion, which is essential to obtain the acoustic black hole effect. Dispersion means that the wavenumber is non-linearly dependent on the frequency, resulting in waves of different frequencies traveling the waveguide at different speeds. This becomes more easily understood, when the concept of phase- and group speeds are introduced. The phase speed of a wave refers to the speed at which a peak or trough of a wave travels; i.e. the *speed* at which a given *phase* moves through space. The phase speed is given as $c_p = \frac{\omega}{k}$. The group speed refers to the speed at which modulations or "grouped packages" of the wave travels and is given as $c_g = \frac{d\omega}{dk}$. Looking at the roots in (3.4) it is seen how the phase- and group speeds are dependent on frequency, and so dispersion occurs. This means, that it is possible to have different wave speeds at different points in the waveguide, if the flexural rigidity is varied, which is the foundation for the acoustic black hole effect, c.f. Chapter 1.

$$EI\hat{k}^4 - \rho A\omega^2 = 0 \tag{3.3}$$

$$k_{1,2} = \pm\sqrt[4]{\frac{\rho A}{EI}}\sqrt{\omega}, \quad k_{3,4} = \pm i\sqrt[4]{\frac{\rho A}{EI}}\sqrt{\omega} \tag{3.4}$$

$$c_p = \frac{\omega}{k} = \sqrt{\omega}\sqrt[4]{\frac{EI}{\rho A}} \tag{3.5}$$

$$c_g = \frac{\partial\omega}{\partial k} = 2\sqrt{\omega}\sqrt[4]{\frac{EI}{\rho A}} \tag{3.6}$$

Next, the Young's Modulus, E, is assumed to be constant while the moment of inertia, I, is expressed as $I(x) = \frac{h(x)^3}{12}$, thereby assuming a rectangular cross-section with unit width. By doing this, the dispersion relations can be expressed in terms of local wave numbers †. Local wave numbers mean, that the wave numbers refer to the instantaneous cross-sectional properties. Allowing wave numbers to be a function of position obviously contradicts the earlier assumption of constant flexural rigidity, and so a condition must be formulated, to ensure the model's validity. In cases where the change in flexural rigidity is sufficiently slow along the length of the beam, the assumption of (3.2) will still result in a usable approximate solution. This condition was formulated in [9] as (3.7), stating that the change in wave number over a single wave should be much smaller than the wave number itself. In literature, the left-hand side of (3.7) is referred to as the "normalized wavenumber variation" or NWV [3]. An acceptable value of NWV is somewhat debatable, but it is mentioned in [11], that an NWV of less than 0.3 satisfies the condition of (3.7) to an acceptable degree, allowing the model to give usable results. This method for modeling the system stems from WKB analysis, which is an asymptotic method for obtaining approximate analytical solutions to linear differential equations with varying coefficients [12, 13]. The underlying theory of the WKB method is however beyond the scope of this project.

$$\frac{dk_x}{dx}\frac{1}{k_x^2} \ll 1 \tag{3.7}$$

Rewriting (3.4) using $I(x)$, one obtains an expression for the localized wave number along the beam, (3.8). From this equation, it is seen, that when the height reduces to zero the local wave number grows to infinity, consequently reducing the phase speed of incoming flexural waves to zero. The group speed is then obtained as (3.9). Here it is also seen, how the group speed goes to zero as the thickness decreases to zero. As the energy transmission occurs at the group speed, the energy transmission halts, and the incoming vibrational energy is accumulated in the cross-section where c_g tends to zero [1]. In this idealized case, wave reflection will never occur, and energy trapped by the acoustic black hole will never be re-released back into the structure. In [9], Mironov presented how a power-law profile given as $h(x) = \epsilon x^n$ could be used to achieve this black hole effect for a simple beam. Here ϵ is a constant† and n is a positive rational number.

$$k_x = \sqrt[4]{\frac{\rho 12 h(x)}{Eh(x)^3}}\sqrt{\omega} \Leftrightarrow \sqrt[4]{\frac{12\rho}{Eh(x)^2}}\sqrt{\omega} \tag{3.8}$$

$$\frac{\partial\omega}{\partial k_x} = c_g = 2\sqrt{\omega h(x)}\sqrt[4]{\frac{E}{12\rho}} \tag{3.9}$$

The power-law profile, results in a reflection coefficient of 0 for $n \geq 2$ for a simple BE beam, but for all practical cases, a residual thickness, h_r, will be present at the tip of the profile, so the actual profile may be expressed as $h(x) = \epsilon x^n + h_r$, giving a significant non-zero reflection coefficient for all powers of n. This means, that in practical applications, the acoustic black hole effect is not sufficient to mitigate vibrations and sound from a structure, as energy will still be able to propagate losslessly in the structure. Because of this, the acoustic black

†The area, $A(x)$, will therefore naturally also be a function of x.

†ϵ is often given indirectly by a predetermined length of the termination profile.

hole effect is used in combination with a lossy material, to dissipate the energy accumulated in the acoustic black hole. The acoustic black hole should therefore be seen as a method for slowing down the waves while energy is being dissipated before they are again re-released back into the structure.

As waves are still being reflected from the acoustic black hole, the reflection coefficient is used as a practical measure of acoustic black hole performance [11]. The reflection coefficient is a scalar between 0 and 1, describing how much of a wave is reflected on incident of a non-homogeneity. The reflection coefficient, R, of the acoustic black hole is determined by the decrease in amplitude, of a wave entering the acoustic black hole at $x = x_E$ until it returns to $x = x_E$ after having reflected at the tip at $x = 0$ (see Figure 3.1 on page 3). Mathematically, the reflection coefficient is formulated as (3.10). As the system until now has been assumed lossless, with a purely real-valued Young's Modulus, E, this integral would always equal 1, assuming $h_r \neq 0$. To introduce some amount of material loss, the Young's Modulus will be assumed in the form $E = E_0(1 - i\eta)$, where η will be taken as some small value ($\eta = 0.05$). In a real-world scenario, the material loss is usually insufficient to obtain desirable damping, and the damping is instead achieved by adding a layer of viscoelastic material to the acoustic black hole. Additionally, the amount of material loss is typically dependent on frequency, but for the sake of simplicity, the damping will be modeled as constant material loss in this example.

$$R = exp\left(-2\int_{x_E}^{x_S} \Im(k)dx\right) \tag{3.10}$$

In the idealized case, where $h_r = 0$, the acoustic black hole effect can be investigated analytically quite easily. The task is, to investigate which termination profiles cause the integral of k_x to diverge. Looking at 3.10, and acknowledging the commutative property of $\Im$, one can see how a divergent integral of k_x would result in a reflection coefficient of zero for even the smallest amount of material dampening. One may also gain some intuition of the acoustic black hole effect, simply by considering what a divergent integral of k_x means physically: an infinite number of oscillations along the termination profile. The analytical analysis is performed for the BE beam by substituting the power law profile expression into (3.8), to obtain (3.11). Integration with respect to x then gives (3.12), where it can be seen that setting $n \geq 2$ causes the integral to diverge. Again, this assumes the integral to include the singularity at $x = 0$ which is equivalent to having $h_r = 0$.

$$k_x = \sqrt[4]{\frac{12\rho\omega^2}{E\epsilon^2 x^{2n}}} \Leftrightarrow \sqrt[4]{\frac{12\rho\omega^2}{E\epsilon^2}} x^{-n/2} \tag{3.11}$$

$$\int k_x dx = \sqrt[4]{\frac{12\rho\omega^2}{E\epsilon^2}} \frac{1}{1-n/2} x^{1-n/2} \tag{3.12}$$

3.2 Acoustic black hole analysis: Choosing termination profile

The mathematical framework for designing an acoustic black hole for a BE beam has now been explained. The task is now to determine the termination profile, to minimize the reflection coefficient while keeping the model limitations, assumptions, and physical dimensions of the geometry in mind. Several shape functions have been investigated, to describe the termination profile e.g. power-law functions [9], trigonometric, Gaussian [12] and optimal profiles derived based on variational principles [11, 14], of course resulting in different performances. The earlier analytical investigations of the acoustic black hole effect in waveguides like plates and beams have resorted to the power-law profile, following the example of M.A. Mironov in [9]. For this reason, the power-law profile will be used throughout this thesis. The power-law profile has three parameters to be determined, all affecting the performance of the acoustic black hole. The three parameters are ϵ defining the length of the profile, the n-value defining the slope of the profile, and h_r defining the residual height of the profile at the tip. A decrease in the reflection coefficient can thus be achieved in three ways when considering (3.10). The length of the profile can be increased, effectively increasing the bounds in the integral of (3.10), the n-value can be increased, resulting in a more abrupt termination of the waveguide, or h_r can be reduced, resulting in a profile which better resembles the termination profile formulated by Mironov [9]. It is not reasonable to model the acoustic black hole profile with a large n-power, as it will increasingly violate the requirement of small normalized wavenumber variation. An extreme example, with a large n-power, will cause the termination profile to look like a simple 90° cut, which will reflect practically all the incoming energy; equation (3.10) would erroneously still predict a very low reflection coefficient.

Increasing the length or decreasing h_r may result in the design being difficult to install and manufacture, and may decrease the structural rigidity of the geometry. In an attempt to obtain a compact acoustic black hole design with a large effective length, studies have attempted to coil up the termination profile, in the shape of an Archimedean spiral. This has proven possible for beam-like waveguides but comes at the cost of increased complexity in manufacturing. A final consideration comes from the fact, that the reflection coefficient will be dependent on frequency. The acoustic black hole should therefore be designed toward attenuating frequencies in the desired frequency range.

The task of designing the profile is a balancing act between obtaining a low reflection coefficient for the desired frequencies while keeping the NWV small and the geometry manufacturable and sufficiently rigid[††].

As a simple example, the reflection coefficient and NWV are calculated for an acoustic black hole in a BE beam using (3.10) and the left-hand side of (3.7). The beam has a termination profile given by: $h_0 = 50\,\text{mm}$, $h_r = 5\,\mu\text{m}$, $x_E = 1\,\text{m}$ with varying n-powers. A complex Young's Modulus with $\eta = 0.05$ is used. Figure 3.2 shows the reflection coefficient and NWV for frequencies $\Omega \in [0, 5]$. The NWV is calculated at $x = x_E$, as this is the location of the largest value. Here, it is immediately seen, that larger n-powers result in lower reflection coefficients, but simultaneously result in a greater violation of the WKB assumption (3.7).

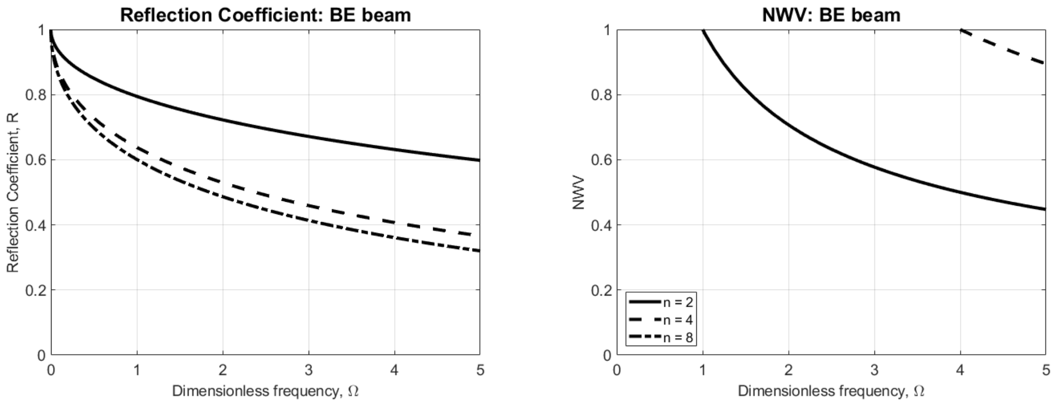

Figure 3.2: Reflection Coefficient and NWV of example acoustic black hole termination on BE beam.

Next, the reflection coefficients are calculated for profiles with $n = 2$, with different values for h_r. In Figure 3.3 it is seen, how a smaller residual height will result in a lower reflection coefficient, with practically no effect on the NWV. There is a slight difference in NWV between the 3 h_r-values, but as the overall shape of the termination profile is largely independent of h_r when close to zero, the 3 graphs are seen to lie on top of each other.

[††]In practice, the task of designing termination profiles is often tackled by numerical optimization around a finite element model, or based on the matrix transfer method see e.g. [15].

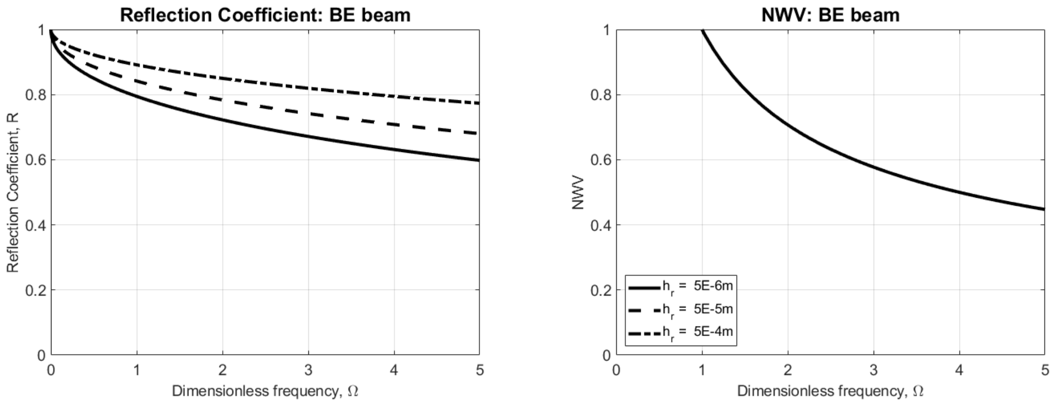

Figure 3.3: Reflection Coefficient and NWV for various residual heights, h_r, at the tip of the termination profile.

Finally, the reflection coefficients are calculated for profiles with $n = 2$ and $h_r = 5 \times 10^{-6}$ m, with varying profile lengths. In Figure 3.4 it is seen, how a longer termination profile results in a lower reflection coefficient, while also lowering the NWV.

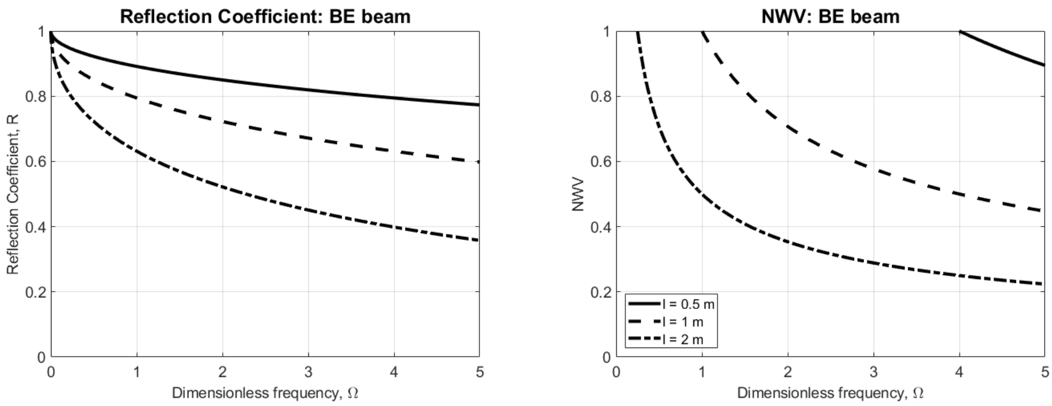

Figure 3.4: Reflection Coefficient and NWV for various termination profile lengths.

A quick note should be made on the validity of the results obtained in this section. It is well known, that the elementary Bernoulli Euler beam theory gives poor predictions of wave-phenomenon at higher frequencies. Comparing the elementary theory to a higher order theory, e.g. the Timoshenko–Ehrenfest beam theory, the elementary theory is shown to diverge as early as $\Omega = 0.3$, giving increasingly poorer results with higher frequencies [14]. Despite this use and abuse of the Bernoulli-Euler model, the simple example shows how the acoustic black hole performance, i.e. the reflection coefficient, is highly dependent on the power-law profile, as well as the frequency range of interest. For $n > 2$ the calculated reflection coefficient is small, indicating great performance, but the associated NWV is so large that the underlying assumptions of the model are violated. It is seen in Figure 3.4, that for $l = 2m$, the NWV reaches reasonable values of ≈ 0.3 at around $\Omega = 3$. The observation, that the calculated acoustic black hole effect is only representative above a certain frequency, is supported by observations made in all experimental investigations [2]. It is observed from experiments, that no wave absorption is achieved below a given frequency, loosely dependent on the characteristic length of the acoustic black hole.

3.3 Answering SRQ 1

How can the acoustic black hole effect be explained mathematically for simple waveguides like Bernoulli Euler beams, and what are the underlying assumptions?
How can the performance of an acoustic black hole be quantified?

In this chapter, the acoustic black hole effect was investigated, in the context of Bernoulli Euler beam theory. Taking offset in the differential equations of motion, the dispersion equation was obtained. Due to the simple nature of the dispersion equation, closed-form solutions were obtained directly for wave numbers as a function of frequency. The wave numbers were then expressed as local wave numbers by expressing the flexural rigidity of the beam as a function of position. This contradicted an earlier assumption, and the condition of low normalized wavenumber variation was introduced, to ensure the validity of the model. The process of choosing a termination profile for the acoustic black hole was discussed. Here it was found, that designing a termination profile is a balancing act between obtaining a low reflection coefficient for the frequency range of interest while keeping the NWV low, to not violate the underlying assumptions. Structural rigidity should also be kept in mind when determining the termination profile if the industrial applicability is considered. The geometry by nature becomes very thin at the tip of the acoustic black hole. In these cases yielding and buckling may become of concern in the structure. Typically the termination profile is determined using numerical optimization, but recent studies have tackled the problem more rigorously for beam waveguides by employing variational approaches. The performance of an acoustic black hole can be determined by the reflection coefficient, which is a scalar between 0 and 1, indicating how much of an incident wave is reflected. Alternatively, for idealized cases, the performance can be assessed by the divergent nature of the anti-derivative of the wavenumber, for a given termination profile. A simple calculation of reflection coefficients was made for the Bernoulli-Euler beam using different power-law termination profiles. This was done assuming a material loss in the form of a complex Young's Modulus. It was found that the reflection coefficient is highly dependent on the termination profile, as well as the frequency range of interest, which is supported by experimental investigations. It was found, that the length of the acoustic black hole has a large effect on the obtained reflection coefficient, while also reducing the NWV. Changing the power of the power-law profile can also greatly decrease the predicted reflection coefficient but at the cost of violating the underlying model assumptions thereby invalidating the results. Finally, reducing the residual height at the tip of the acoustic black hole can decrease the predicted reflection coefficient, without affecting the NWV measurably.

SRQ 2: Asymptotic acoustic black hole analysis of cylindrical shells 4

In this chapter, SRQ 2 will be answered, by analyzing the acoustic black hole effect using naive asymptotic approximations. The cylindrical shell model will now be presented, for the case of no internal fluid loading. First, the geometry, as well as parameters and notation is presented. Next, the differential equations of motion are presented, from where the dispersion equation is derived. From here, approximate solutions to the dispersion equation are obtained for individual m-spectrum, based on asymptotic approximations. These asymptotic approximations are then used to analyze the acoustic black hole effect, by the calculation of phase- and group speed expressions, together with reflection coefficients and associated NWV for acoustic black hole terminations. The investigation will be performed on individual m-spectrum, indicated in Figure 4.1. The analysis will consider $m = 0, 1, 2$, to investigate the simplest cases of the breathing mode ($m = 0$), beam-like motion ($m = 1$), and finally deformation of the cross-section profile by the ovalling mode ($m = 2$). These m-spectra represent the circumferential wavenumber in the shell, and determine the deformation of the cross-section. Several m-spectra are visualized in Figure 4.1.

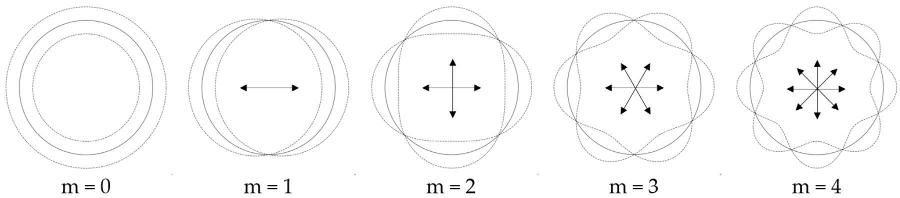

Figure 4.1: Circumferential modes (m-spectrum) for the cylindrical shell.

Figure 4.2 shows the cylindrical shell model with dimensional parameters and notation illustrated. Though not indicated in the figure, the project will base itself on the analysis of thin-walled cylindrical shells under small deformation, thereby taking offset in Love's first approximation. All displacements are expressed in terms of the deformation of the middle surface (indicated by the dashed circle in the figure), and gradients thereof, resulting in the position along the shell being given by only two coordinates: x and θ. As indicated in the Figure, the model has 3 independent displacement components: u_m, v_m, w_m, representing the longitudinal, circumferential, and radial displacements of the middle surface respectively. The material is assumed to be linearly elastic with material constants E, ν, and ρ as the Young's modulus, Poisson's ratio, and material density respectively.

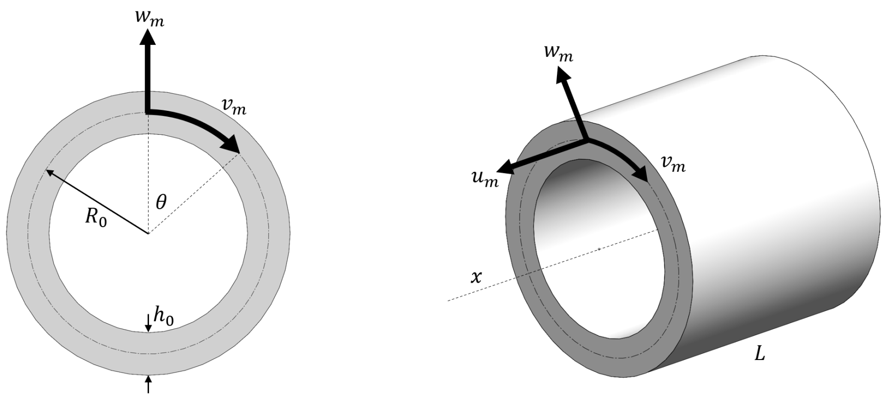

Figure 4.2: Cylindrical shell model with dimensional parameters and notation illustrated. Mid-surface displacement components (u_m, v_m, w_m), mid-surface coordinates (x, θ), dimensional parameters (L, h_0, R_0). The geometry illustrated in the figure is not representative of the model assumptions, and the ratio between shell thickness and radius will be much smaller in the analyzed geometries.

The differential equations of motion for a thin-walled cylindrical shell from the Goldenveizer-Novozhilov theory are readily available from literature, see e.g. [16, 17], and are presented here as (4.1, 4.2, 4.3). The equations are in the homogeneous form (assuming no forcing) and the length, L, is assumed infinite to disregard boundary conditions. In the equations, a time-harmonic dependence has also been assumed for the 3 displacement components, in the form of $exp(-i\omega t)$ where i is the complex number, ω is the dimensional angular frequency and t is time. This time dependency is omitted from the equations for simplicity, but all solutions are still time-harmonic in nature. The displacement terms (u_m, v_m, w_m) are in all the following derivations in the form of amplitudes as a function of the longitudinal coordinate, x.

$$-\frac{d^2u_m}{dx^2} + \frac{1-\nu}{2}\frac{m^2}{R^2}u_m - \frac{1+\nu}{2}\frac{m}{R}\frac{dv_m}{dx} - \frac{\nu}{R}\frac{dw_m}{dx} - \frac{\rho\omega^2(1-\nu^2)}{E}u_m = 0 \tag{4.1}$$

$$\begin{aligned}&\frac{1+\nu}{2}\frac{m}{R}\frac{du_m}{dx} - \frac{1-\nu}{2}\frac{d^2v_m}{dx^2} + \frac{m^2}{R^2}v_m - \frac{h^2}{12}\frac{2(1-\nu)}{R^2}\frac{d^2v_m}{dx^2} + \frac{h^2}{12}\frac{m^2}{R^4}v_m\\ &+\frac{m}{R^2}w_m + \frac{h^2}{12}\frac{m^3}{R^4}w_m - \frac{h^2}{12}\frac{(2-\nu)m}{R^2}\frac{d^2w_m}{dx^2} - \frac{\rho\omega^2(1-\nu^2)}{E}v_m = 0\end{aligned} \tag{4.2}$$

$$\begin{aligned}&\frac{\nu}{R}\frac{du_m}{dx} + \frac{m}{R^2}v_m + \frac{h^2}{12}\frac{m^3}{R^4}v_m - \frac{h^2}{12}\frac{(2-\nu)m}{R^2}\frac{d^2v_m}{dx^2} + \frac{1}{R^2}w_m\\ &+\frac{h^2}{12}\frac{d^4w_m}{dx^4} - \frac{h^2}{12}\frac{2m^2}{R^2}\frac{d^2w_m}{dx^2} + \frac{h^2}{12}\frac{m^4}{R^4}w_m - \frac{\rho\omega^2(1-\nu^2)}{E}w_m = 0\end{aligned} \tag{4.3}$$

From these differential equations, the dispersion equation is readily obtained from assuming a space-harmonic solution for the displacement amplitudes $u_m(x)$, $v_m(x)$, $w_m(x)$, and solving for non-trivial solutions. The space-harmonic solution will be in the form of $A_j exp(ik_x x)$ where k_x is the dimensional wavenumber with units $[m^{-1}]$. From this ansatz, the equations of motion condense to (4.4, 4.5 4.6).

$$k_x^2A_1 + \frac{1-\nu}{2}\frac{m^2}{R^2}A_1 - \frac{1+\nu}{2}\frac{m}{R}A_2ik_x - \frac{\nu}{R}A_3ik_x - \frac{\rho\omega^2(1-\nu^2)}{E}A_1 = 0 \tag{4.4}$$

$$\begin{aligned}&\frac{1+\nu}{2}\frac{m}{R}A_1ik_x + \frac{1-\nu}{2}A_2k_x^2 + \frac{m^2}{R^2}A_2 + \frac{h^2}{12}\frac{2(1-\nu)}{R^2}A_2k_x^2 + \frac{h^2}{12}\frac{m^2}{R^4}A_2\\ &+\frac{m}{R^2}A_3 + \frac{h^2}{12}\frac{m^3}{R^4}A_3 + \frac{h^2}{12}\frac{(2-\nu)m}{R^2}A_3k_x^2 - \frac{\rho\omega^2(1-\nu^2)}{E}A_2 = 0\end{aligned} \tag{4.5}$$

$$\begin{aligned}&\frac{\nu}{R}A_1ik_x + \frac{m}{R^2}A_2 + \frac{h^2}{12}\frac{m^3}{R^4}A_2 + \frac{h^2}{12}\frac{(2-\nu)m}{R^2}A_2k_x^2 + \frac{1}{R^2}A_3\\ &+\frac{h^2}{12}A_3k_x^4 + \frac{h^2}{12}\frac{2m^2}{R^2}A_3k_x^2 + \frac{h^2}{12}\frac{m^4}{R^4}A_3 - \frac{\rho\omega^2(1-\nu^2)}{E}A_3 = 0\end{aligned} \tag{4.6}$$

These equations are cast into matrix form, having introduced the non-dimensional parameters as presented in (4.8). From here the non-trivial solutions are found by equating $|L|= 0$.

$$L_{jl}A_j = 0; j, l = 1, 2, 3 \tag{4.7}$$

$$\begin{aligned}L_{11} &= k^2 + \frac{1-\nu}{2}m^2 - \Omega^2\\ L_{22} &= \frac{1-\nu}{2}k^2 + m^2 + t^2 2(1-\nu)k^2 + t^2m^2 - \Omega^2\\ L_{33} &= 1 + t^2(k^2+m^2)^2 - \Omega^2\\ L_{12} &= -L_{21} = \frac{1+\nu}{2}mik\\ L_{13} &= -L_{31} = \nu ik\\ L_{23} &= L_{32} = m + t^2m^3 + t^2(2-\nu)mk^2\end{aligned}$$

$$k = k_x R \qquad t^2 = \frac{h^2}{12R^2} \qquad \Omega^2 = \frac{\omega^2 R^2}{c_L^2} = \frac{\rho(1-\nu^2)\omega^2 R^2}{E} \tag{4.8}$$

4.1 Investigating the breathing mode: $m = 0$

First, the breathing mode of the cylindrical shell is investigated. For the special case of $m = 0$, (4.5) decouples from the remaining two equations, resulting in a system where the torsional wave is independent of the longitudinal and bending waves. As this torsional wave is dispersionless, it has little interest in the context of acoustic black holes, and will be condensed from the set of equations. This means, that the characteristic equation reduces to $L_{11}L_{33} - L_{13}L_{31} = 0$, which is given in non-dimensional parameters as (4.9).

$$(k^2 - \Omega^2)(1 + t^2k^4 - \Omega^2) + \nu^2 k^2 = 0 \tag{4.9}$$

As discussed in Chapter 3 the next step is to obtain a closed-form expression for the dispersion characteristics, given by the roots of (4.9). Unfortunately, it is no trivial matter to do analytically, and numerical solutions, such as the one presented in Figure 4.3, are therefore commonly sought. The numerical solution is found, including the second decoupled equation, to get a fuller picture. This numerical solution gives little in terms of usable information for the study of acoustic black holes, and therefore a semi-analytical solution is sought in the form of a naive asymptotic expansion later.

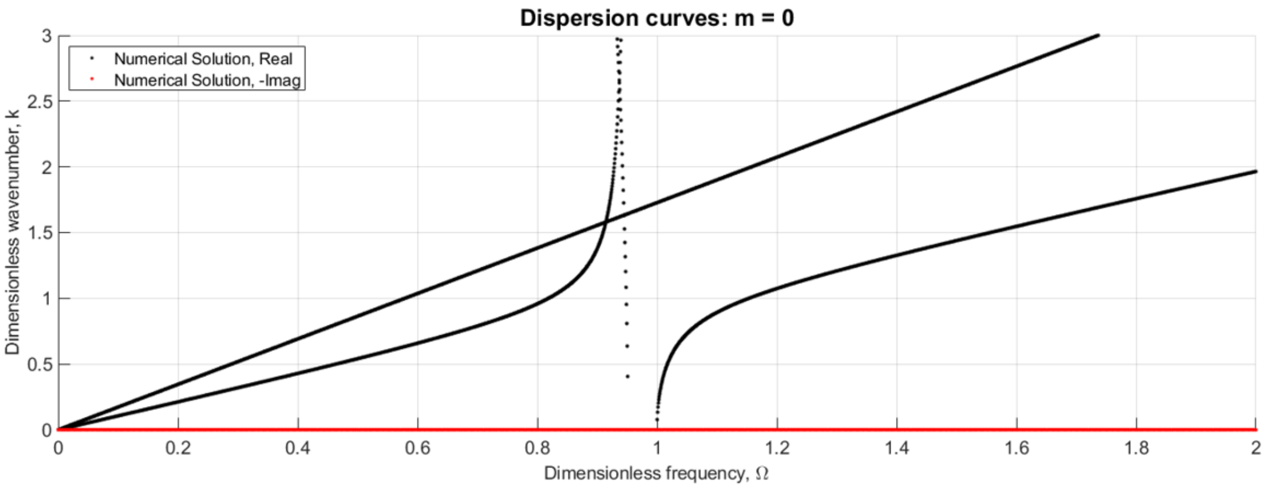

Figure 4.3: Numerical solution for dispersion curves for a cylindrical shell. Circumferential mode m = 0. Torsional branch included.

Before diving into the asymptotic expansions, however, the dispersion characteristics of the breathing mode will be discussed briefly, to get a better understanding of the physical intuition that lies behind the numerical solution in Figure 4.3. Looking at the figure, it seems as if 3 distinct branches are present indicated in black; two of which originate from zero, and one of which cuts on at $\Omega = 1$. This is however not the entire picture: as the dispersion equation is an 8^{th} order polynomial in k, there will be 8 roots for every frequency, and so 8 branches exist. It is however difficult to understand the nature of the dispersion branches from a simple 2D representation, and so a 3D plot is made in Figure 4.4 (Several full-page figures can be found in Appendix C). In the figure, the 8 branches are seen color coded for easy referencing. Solid lines represent purely real-valued wave numbers, while dashed lines indicate the wavenumber to have a non-zero complex component.

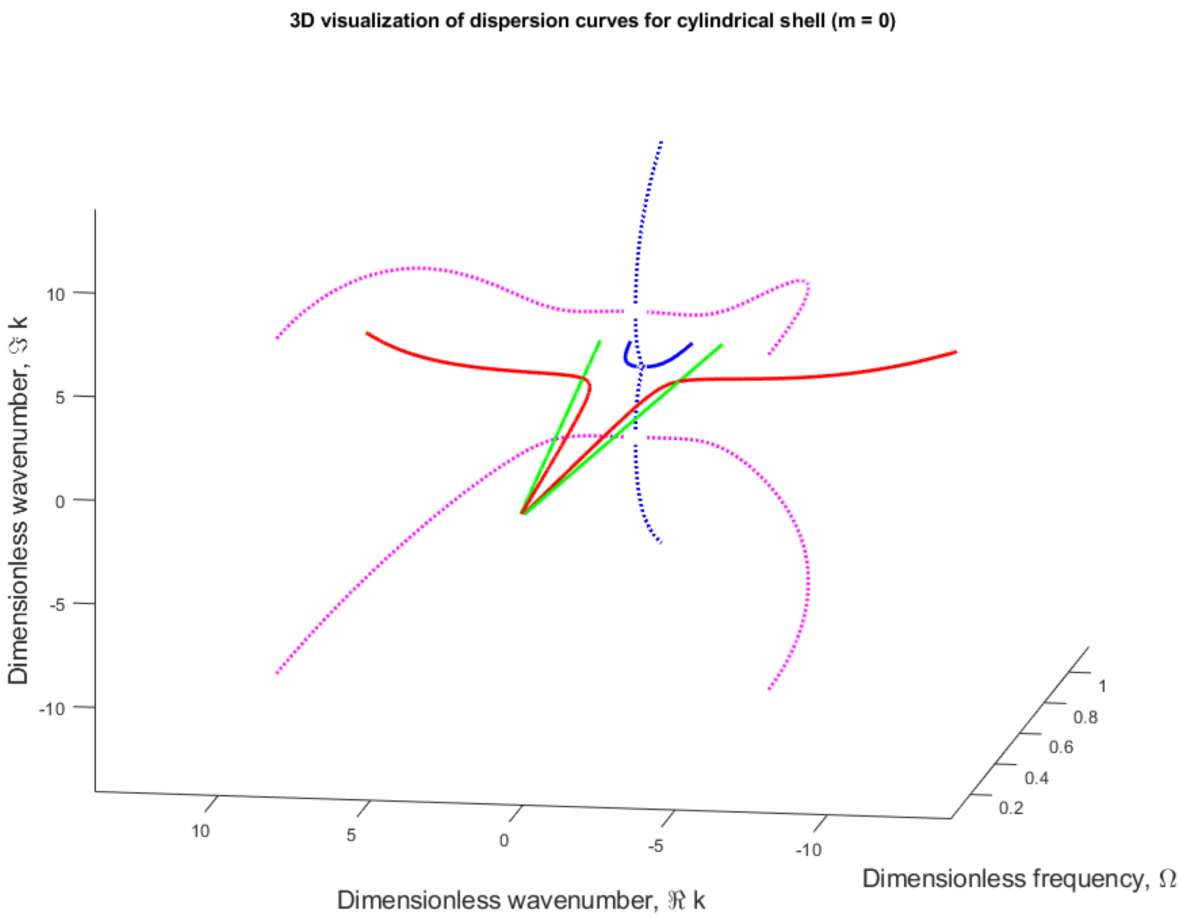

Figure 4.4: 3D visualization of dispersion branches for cylindrical shell (m = 0).

The green branch represents a purely torsional wave, and is completely dispersionless and uncoupled from the other branches, as mentioned earlier.

The red branch also originates from zero and represents a wave which is dominated by longitudinal motion (u-motion). As opposed to the green branch, it is not possible to call it a "pure longitudinal wave", as the first and third equations of (4.7) are coupled by Poisson-effects. Any motion in the u-direction will therefore inevitably couple with motion in the w-direction. Just before $\Omega = 1$, the red branch bends sharply upwards, and the wave motion transitions from predominantly longitudinal, to being dominated by flexural motion. This transition has been observed both experimentally and numerically [18]. The frequency $\Omega = 1$ is called the "ring frequency", and its physical interpretation can be understood through some simple algebra in (4.10). Here it is seen, that the ring frequency is the frequency where the longitudinal wavelength equals the circumference of the shell resulting in a breathing resonance occurring.

$$\Omega = 1 = \frac{\omega R}{c_L} \Leftrightarrow 2\pi f R = c_L \Leftrightarrow 2\pi R = \frac{\lambda_L f}{f} = \lambda_L \tag{4.10}$$

The magenta and blue branches are very interesting in nature and must be explained together. Beginning from $\Omega = 0$, the magenta branches are complex-valued, up to around $\Omega = 0.95$, representing an attenuating near-field flexural wave. At around $\Omega = 0.95$, both pairs of the magenta branches "collide", as the real component of the wavenumber goes to zero. It can be seen how the four complex waves transition to four purely imaginary evanescent waves (dotted blue). Two of these waves become increasingly complex with higher frequencies, but the remaining two branches meet at $\Omega = 1$, to become two purely real-valued propagating waves. It is one of these waves which are visualized to cut on at $\Omega = 1$ in Figure 4.3.

4.1.1 Asymptotic expansions for $m = 0$

Now, asymptotic expansions will be employed to obtain closed-form approximate solutions to the dispersion equation. Asymptotic approximations are based on expressing the solution as a truncated series expansion which may even be divergent in nature [19]. The method of asymptotic expansions is widely used in applied mathematics and engineering, for solving complex algebraic equations, integrals, and partial differential equations. Even in situations such as the one in this project, where numerical results are available, the asymptotic approximations provide much more than just a simple curve fit, as the obtained solution is directly tied to the nature of the problem. The obtained solution therefore often gives very useful insight into the nature of the true solution to the problem [19]. The solution to (4.9) will be sought based on the theory presented in [20], where the so-called expansion method will be applied. The idea behind this method is, to formulate the expansion around some small parameter in the equation denoted ϵ. The series will then be made as a sum of terms with ever increasing powers of ϵ. The approximate solution will then be a function of this expansion parameter; $\bar{k}(\epsilon)$, and will be in the form of (4.11).

$$\bar{k}(\epsilon) = x_0\epsilon^{p_0} + x_1\epsilon^{p_1} + ...; \qquad p_i < p_{i+1} \tag{4.11}$$

Depending on the required accuracy of the approximation, more or fewer terms can be included in the expansion.† To apply the method, the expression in (4.11) is substituted into (4.9), and the equation is expanded in order to identify the terms of greatest relative magnitude assuming, of course, $\epsilon \ll 1$. This means, that e.g. a term at the ϵ^1-power will be greater than a term at the ϵ^2-power, and so the latter may be disregarded, while still resulting in a good approximation around $\epsilon = 0$. The higher order terms are disregarded in the expanded solution, leaving only terms of large relative magnitude containing the unknown scalar, x_i. x_i is then determined based on this truncated expression, and the process is repeated for terms of large relative magnitude containing x_{i+1}. For examples of application the reader is directed to [20].

Choosing the powers for the expansion series, p_i is not a systematic process but more in the nature of trial and error. In [20], a method is presented for determining the expansion series systematically, but the method quickly becomes impractical for complex systems. Instead, the expansion series will be determined by trial and error, supported by a visual comparison between the asymptotic solution and the numerical solution in Figure 4.3.

First order asymptotic approximation for $m = 0$.

Looking at (4.9), the last term contains ν^2 which will serve as the expansion parameter, as for many common engineering materials $\nu^2 \ll 1$. An expansion is proposed in the form of $\bar{k}(\epsilon) = x_0$ (with $p_0 = 0$), and more terms can be added subsequently if necessary.

Equation (4.9) becomes (4.12) with the assumed solution for $\bar{k}$. Disregarding terms above order $\mathcal{O}(\nu^0)$ one clearly sees, the roots being equivalent to the roots of either of the remaining parenthesis in (4.13). The roots are then given as (4.14).

$$(\bar{k}^2 - \Omega^2)(1 + t^2\bar{k}^4 - \Omega^2) + \nu^2\bar{k}^2 = 0 \tag{4.12}$$

$$(x_0^2 - \Omega^2)(1 + t^2 x_0^4 - \Omega^2) = 0 \tag{4.13}$$

$$x_0 = \pm\Omega; \qquad \pm\frac{(\Omega^2 - 1)^{1/4}}{\sqrt{t}}; \qquad \pm i\frac{(\Omega^2 - 1)^{1/4}}{\sqrt{t}} \tag{4.14}$$

Firstly, the solution $x_0 = \pm\Omega$ is purely real-valued, meaning it refers to freely propagating waves in the positive and negative x-direction. Secondly, the solution is dispersionless, which means it gives little in terms of usable information when studying the acoustic black hole effect. Because of this second point, a second term is required in the asymptotic approximation, in order to capture some dispersion phenomenon. The last 4 solutions in

†More terms can also be added to the expansion subsequently after an expansion has already been calculated for a given number of terms. In fact, this is often how the expansion method is applied in practice.

(4.14) represent 4 waves; two propagating and two evanescent one of each going in the positive and negative x-direction. Secondly, the solution has dispersion, as there is a non-linear relation between wavenumber and frequency. Thirdly, at the limit where $\Omega = 0$, the solution is non-zero representing a solution branch that does not originate from zero. Because of this, the asymptotic expansion will only be sought for the branch associated with $x_0 = \pm\Omega$.

Second order asymptotic expansion

Having determined the first term in the asymptotic expansion, the second term can now be added. This will be done for the solution where $x_0 = \Omega$, to capture some dispersion phenomenon. The second order asymptotic expansion will be assumed in the form $\bar{k} = x_0 + x_1\nu^2$[††].

Setting $x_0 = \Omega$, and expanding (4.9) one obtains the terms in (4.15). x_1 is determined by balancing terms at order $\mathcal{O}(\nu^2)$.

$$\begin{Bmatrix}\nu^2 & \nu^4 & \nu^6 & \nu^8 & \nu^{10} & \nu^{12}\end{Bmatrix} \begin{Bmatrix} \Omega^2 + 2\Omega x_1 - 2\Omega^3 x_1 + 2\Omega^5 t^2 x_1 \\ x_1^2 + 2\Omega x_1 - \Omega^2 x_1^2 + 9\Omega^4 t^2 x_1^2 \\ x_1^2 + 16\Omega^3 t^2 x_1^3 \\ 14\Omega^2 t^2 x_1^4 \\ 6\Omega t^2 x_1^5 \\ t^2 x_1^6 \end{Bmatrix} = 0 \tag{4.15}$$

$$\begin{aligned} &\Omega^2 + 2\Omega x_1 - 2\Omega^3 x_1 + 2\Omega^5 t^2 x_1 = 0 \\ &x_1 = \frac{\Omega}{2(1 - \Omega^2 + \Omega^4 t^2)} \end{aligned}$$

And so the second order asymptotic expansion is found in the form (4.16).

$$\bar{k}(\nu) = \Omega + \frac{\nu^2\Omega}{2(1 - \Omega^2 + \Omega^4 t^2)} \tag{4.16}$$

The left side of Figure 4.5 shows the asymptotic approximation overlaid with the numerical solution, this time without the torsional branch. The approximation is plotted for $\nu = 0.2$ and will give increasingly good results with decreasing ν. The figure shows how the approximation gives excellent results away from $\Omega = 1$. The branch originating from zero starts to diverge from the numerical solution as it approaches $\Omega = 1$, and begins to give very poor results at $\Omega > 1$. This is more easily seen to the right in Figure 4.5, where the asymptotic approximation grows to infinity. The branch cutting on at $\Omega = 1$ is also captured well by the approximation away from $\Omega = 1$. The approximation continues to give good results for increasing Ω for the bending branch. This would indicate, that the obtained approximation is valid for two different dispersion branches, in different intervals. It is seen how the first term in the asymptotic expansion dominates away from $\Omega = 1$, while the second term becomes dominant around $\Omega = 1$.

[††]It was also attempted to find the second term in the form of $x_1\nu$, but it yielded no correct expansion.

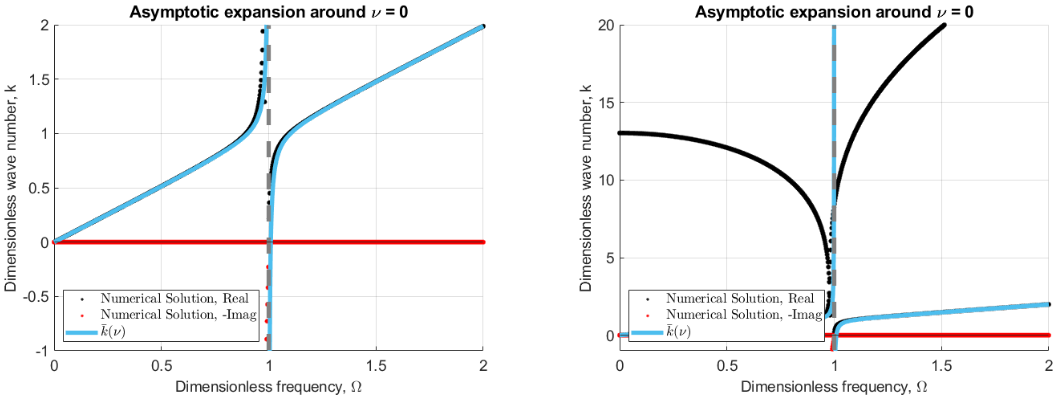

Figure 4.5: Asymptotic approximation overlaid numerical solution of dispersion curves. Cylindrical shell, breathing mode ($m = 0$), $\nu = 0.2$.

4.1.2 Analyzing acoustic black hole effect for m = 0

Having validated the accuracy of the asymptotic expansion against the numerical solution, the acoustic black hole effect can be investigated. The termination profile of the shell is visualized in Figure 4.6, showing how the shell thickness, $h(x)$ decreases towards zero, just as was done for the simple BE beam in Chapter 3. The shape of the termination profile is assumed in the form $h(x) = \epsilon x^n + h_r$. Again, the figure is not entirely representative of the mathematical model, as the thickness reduction should be performed symmetrically, to retain the same mid-surface radius.

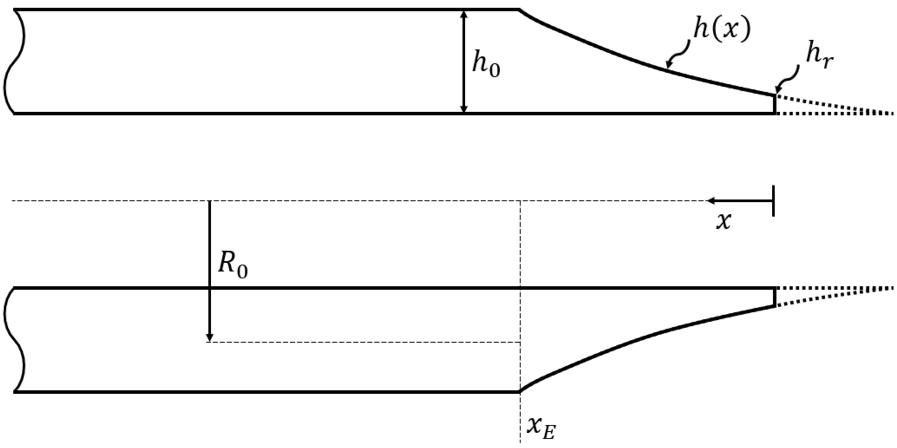

Figure 4.6: Acoustic black hole termination on the cylindrical shell. Termination is unsymmetrical despite the mathematical model indicating symmetry.

First, expressions for phase- and group speeds can be derived as (4.17) and (4.18) respectively. As was mentioned in Chapter 3, the acoustic black hole effect arises from the phenomenon, that the group velocity tends to zero with decreasing flexural rigidity; in this case driven by the change in shell thickness. Looking at (4.18), it is apparent that the equation does not reduce to zero when $t \to 0$. This means, that the acoustic black hole effect likely does not appear to a usable extent, for the breathing mode of an elastic cylindrical shell in the low-frequency range, if a termination profile where $h \to 0$ is used. In (4.19), the group speed is evaluated, for the limiting case of $t \to 0$ and it is here apparent that the group speed only reaches zero when $\Omega = 1$.

$$c_p = \frac{\Omega}{\bar{k}} = \frac{1}{\frac{v^2}{2\,(t^2\,\Omega^4 - \Omega^2 + 1)} + 1} \tag{4.17}$$

$$c_g = \frac{\partial \Omega}{\partial \bar{k}} = \frac{1}{\frac{v^2}{2\,(t^2\,\Omega^4 - \Omega^2 + 1)} + \frac{v^2\,\Omega\,(2\,\Omega - 4\,t^2\,\Omega^3)}{2\,(t^2\,\Omega^4 - \Omega^2 + 1)^2} + 1} \tag{4.18}$$

$$c_g\bigg|_{t=0} = \frac{1}{\frac{\Omega^2 \nu^2}{(\Omega^2 - 1)^2} - \frac{\nu^2}{2\Omega^2 - 2} + 1} \tag{4.19}$$

The reflection coefficient and associated NWV are presented in Figure 4.7, for a termination profile with $n = 2$. As in Chapter 3, the material loss is modeled as a complex Young's Modulus, $E = E_0(1 - i\eta)$. The Figure shows the reflection coefficients and associated NWV for a termination profile given by $h(x) = \epsilon x^n + h_r$ with the dimensions presented in Table 4.1. As a reminder, the reflection coefficient and NWV are calculated using (3.10) on page 5 and the left-hand side of (3.7) on page 4 respectively.

h_0	0.005 m	Shell thickness outside acoustic black hole
h_r	5×10^{-6} m	Shell thickness at tip of acoustic black hole
R_0	0.2 m	Shell radius outside acoustic black hole
l	0.2 m	Termination profile length
η	0.05	Complex material loss
n	2	Power-law termination profile power

Table 4.1: Dimensions for analyzed cylindrical shell with power-law termination profile, and complex Young's modulus.

The decrease in group speed around $\Omega = 1$ is also reflected in the obtained reflection coefficients, where a distinct dip is seen around this frequency. The NWV is almost zero for all frequencies, due to the dispersionless nature of the approximate solution away from $\Omega = 1$. No change in h_0, R_0, l, or n-value gave results significantly different from the ones presented in Figure 4.7.

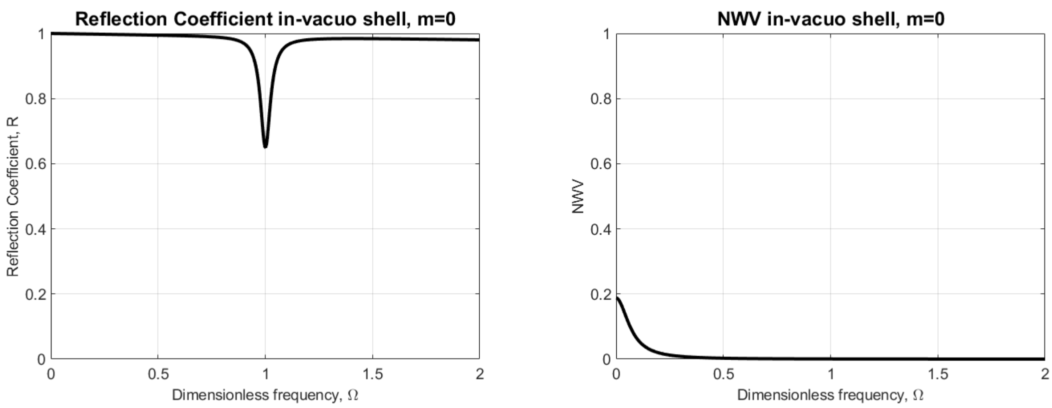

Figure 4.7: Reflection Coefficient and NWV for power-law termination profile on the cylindrical shell ($m = 0$).

It is only possible to obtain the acoustic black hole effect, if one is able to affect the group speed of incoming waves, by varying the dimensions of the waveguide. As was discussed at the beginning of Section 4.1, the wave-motion of the branch starting at the origin is dominated by longitudinal motion up to $\Omega = 1$, and so is the branch cutting on at $\Omega = 1$, above $\Omega = 1$. If the cylindrical shell is viewed as a simple bar, transmitting longitudinal waves, it is well known that the wave speed in independent of the cross-section, and so a typical acoustic black hole termination profile, where the flexural rigidity is reduced, would not affect the group speed of incoming waves. The obtained asymptotic approximation describes the dispersion characteristics in these regions where longitudinal motion is dominant, and so it is to be expected, that no acoustic black hole effect is observed from the employed termination profile.

4.2 Investigating the bending mode: $m = 1$

To investigate the bending mode, we return to the dispersion equation, (4.7 on page 10). Setting $m = 1$, it is seen how the second equation no longer decouples from the system, and thus the characteristic polynomial to be investigated will come from the full 3-by-3 system. The full expressions quickly become impractical to both write and read and are omitted from the report for this reason. Numerically obtained dispersion curves for the bending mode, $m = 1$, for the cylindrical shell, are presented in Figure 4.8.

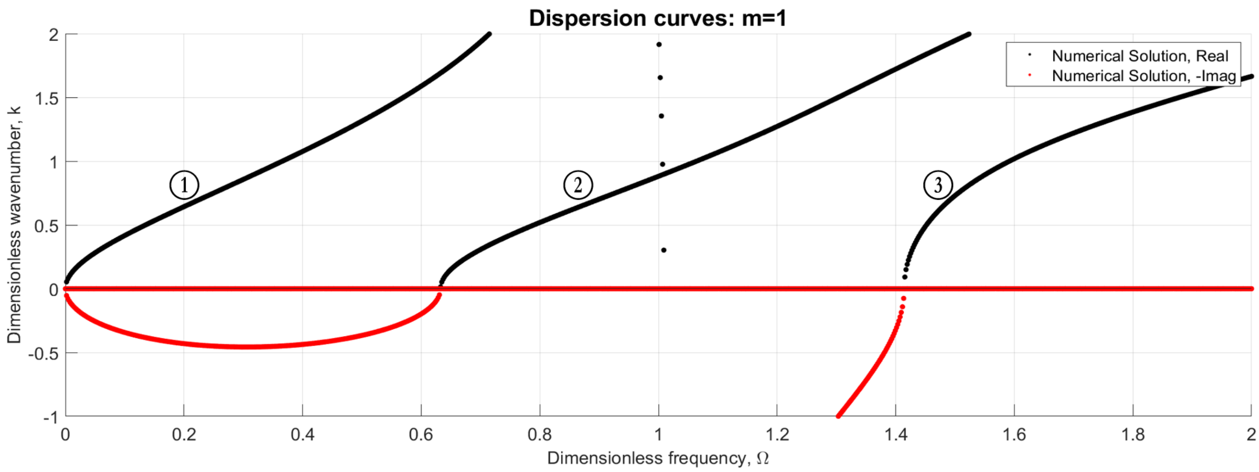

Figure 4.8: Numerical solution for dispersion curves for the cylindrical shell. Circumferential mode m = 1.

4.2.1 Asymptotic expansion for $m = 1$

When the breathing mode was analysed, a suitable expansion parameter was determined from inspection of the individual terms in the dispersion equation. For the case of the bending mode, this is impractical due to the complexity of the dispersion equation. Instead, the problem will be tackled in a different way, by using Ω as the expansion parameter itself. A unique asymptotic approximation is then found for each of the 3 purely real sections of the dispersion branches in Figure 4.8[†].

To find the expansion for the first branch, originating at $\Omega = 0$, Ω is chosen as the expansion parameter. Similarly, to find the expansion for the second branch, $(\Omega - \Omega_{1.CutOn})$ is chosen as the expansion parameter. By using these "offset" Ω-values as perturbation parameters, the asymptotic expansions will still be developed around a small parameter, even though the dispersion branch does not originate from $\Omega = 0$.

The expansion series will be determined by trial and error, supported by a visual comparison between the asymptotic solution and the numerical solution in Figure 4.8.

Asymptotic expansion for the first branch

The expansion series for the first branch will now be determined, based on the general form presented earlier as (4.11) on page 13. Looking at the first branch in Figure 4.8, it is clear that the solution starts from the origin. Because of this, and the fact that the expansion parameter is chosen as Ω, this immediately excludes the possibility of a constant term; $p_0 = 0$. All 3 of the dispersion branches have a group speed of zero at their cut-on frequency, hinting towards the first terms being in the form of a root function; square root, cubic root, etc. It is also seen, that around $\Omega = 0$, the first branch has a tendency reminiscent of a square-root function. Away from the origin, the dispersion branch bends upwards, reminiscent of a polynomial term of power greater than unity. Because of these observations, an expansion is attempted in the form of (4.20) [††].

$$\bar{k}(\Omega) = x_0\Omega^{\frac{1}{2}} + x_1\Omega^{\frac{3}{2}} \tag{4.20}$$

[†] An expansion around $\nu = 0$ was proposed and attempted, but it yielded no usable results for the bending mode.
[††] This proposed expansion was a result of extensive trial and error.

Substituting the first term of (4.20) into the dispersion equation, and evaluating terms at order $\mathcal{O}(\Omega^2)$, the x_0 factor is determined as (4.21).

$$x_0 = \left(\frac{-2}{\nu^2 t^2 + \nu^2 - t^2 - 1}\right)^{1/4} \tag{4.21}$$

Substituting both terms of (4.20) into the dispersion equation, and evaluating terms at order $\mathcal{O}(\Omega^3)$, the x_1 factor is determined as (4.22), which is so intricate it is unusable for any further analytical investigation. The term is however usable for the specific task of numerically determining the reflection coefficient of an acoustic black hole later.

$$x_1 = -\frac{-2\,\nu^2\,t^2 + 2\,\nu^2 - 4\,\nu\,t^4\,{x_0}^4 - 4\,\nu\,t^2\,{x_0}^4 + 7\,\nu\,t^2 + 3\,\nu + 4\,t^4\,{x_0}^4 + 4\,t^2\,{x_0}^4 - 9\,t^2 - 5}{4\,x_0\,(t^2+1)^2\,(\nu-1)^2\,(\nu+1)} \tag{4.22}$$

The asymptotic approximation is overlaid with the numerical solution for the first branch in Figure 4.9, using both the first and the second terms. It can be seen how the first term closely follows the numerical solution up to around $\Omega = 0.05$. Adding the second term makes the approximation follow the upwards trend of the numerical solution, giving a usable approximation up to around $\Omega = 0.5$.

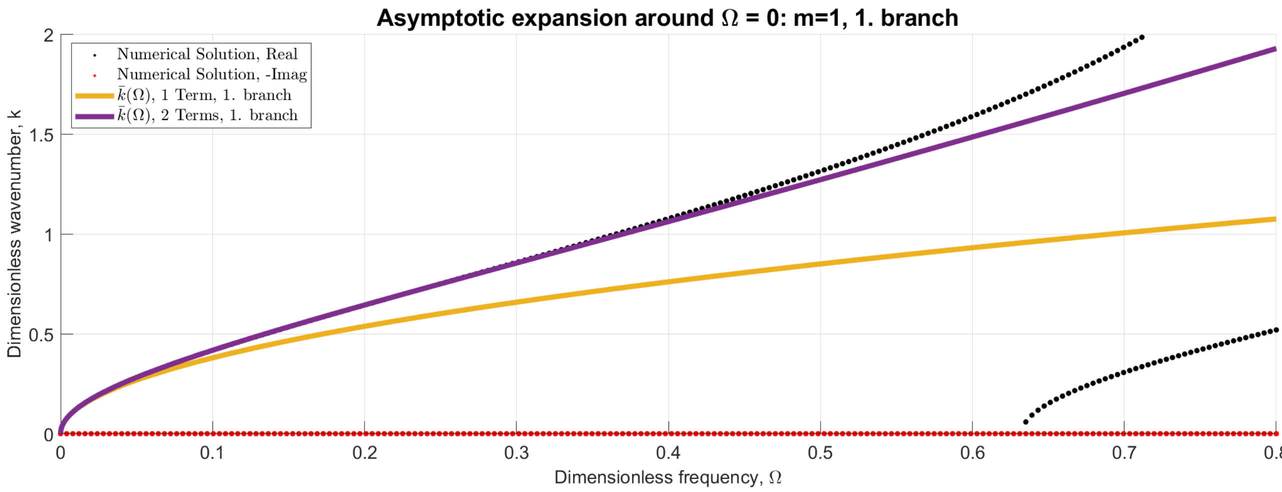

Figure 4.9: Asymptotic approximation for the first branch overlaid with the numerical solution ($m = 1$).

Asymptotic expansion for the second branch

Continuing the analysis for the second branch, one must determine a specific cut-on frequency for the second branch. This is simply done, by solving the dispersion equation (4.7) for Ω, setting $k = 0$. The Dispersion equation for the cylindrical shell is an 8^{th} order polynomial in k, but only a 6^{th}-order polynomial in Ω. Due to the symmetry of the problem, this 6^{th}-order polynomial in Ω can be expressed as a bi-cubic polynomial, allowing for an analytical solution to easily be obtained. The 6^{th}-order polynomial is given as (4.23), which can be reduced to the 3^{rd}-order polynomial as (4.24), where $\Omega_{SQR} = \Omega^2$.

$$\Omega^6 + \Omega^4\left(\frac{\nu}{2} - 2t^2 - \frac{5}{2}\right) + \Omega^2(1 - \nu + t^2 - \nu t^2) = 0 \tag{4.23}$$

$$\Omega_{SQR}^3 + \Omega_{SQR}^2\left(\frac{\nu}{2} - 2t^2 - \frac{5}{2}\right) + \Omega_{SQR}(1 - \nu + t^2 - \nu t^2) = 0 \tag{4.24}$$

The roots of this 3^{rd}-order polynomial are given by the expressions in (4.25). Referring to Figure 4.8 it is obvious which root corresponds to which cut-on frequency.[†]

$$\Omega_{C1} = 0; \qquad \Omega_{C2} = \sqrt{\frac{1}{2} - \frac{\nu}{2}} \approx 0.6325; \qquad \Omega_{C3} = \sqrt{2t^2 + 2} \approx 1.4142 \tag{4.25}$$

Just as for the first branch, the second branch has zero group speed at its cut-on frequency, indicating the first term should be a root function. The shape of the second branch resembles that of the first branch, and so the first term in the expansion is proposed as a square-root function. As mentioned earlier, the expansion parameter will be Ω, but offset with its cut-on frequency, Ω_{2C}, given in (4.26).

$$\bar{k}(\Omega - \Omega_{C2}) = x_0 \left(\Omega - \sqrt{\frac{1}{2} - \frac{\nu}{2}}\right)^{\frac{1}{2}} + x_1 \left(\Omega - \sqrt{\frac{1}{2} - \frac{\nu}{2}}\right)^{\frac{3}{2}} \tag{4.26}$$

Performing the expansion with the proposed solution of (4.26), and balancing terms at order $\mathcal{O}(\Omega^2)$, the solution for x_0 is found as (4.27). The second term is determined by assuming the same expansion as for the first branch and by balancing terms at order $\mathcal{O}(\Omega^3)$. Again, due to its size, the second term is so complex, it is impractical for any further analytical manipulation. Due to its size, the term is only presented in Appendix A, where all the asymptotic expansions from this chapter can be found listed. The asymptotic approximation is overlaid with the numerical solution for the second branch in Figure 4.10, using both the first and the second term.

$$x_0 = 2^{3/4} \sqrt{\frac{(1-\nu)^{1/2}(4t^2 + \nu + 3)}{5\nu^2 + 2\nu t^2 + 2\nu - 10t^2 - 7}} \tag{4.27}$$

It can be seen in the figure, how the first term gives an expansion that traces the numerical solution up to around $\Omega = 0.7$, and how adding the second term gives an approximation that traces the solution up to around $\Omega = 1.1$.

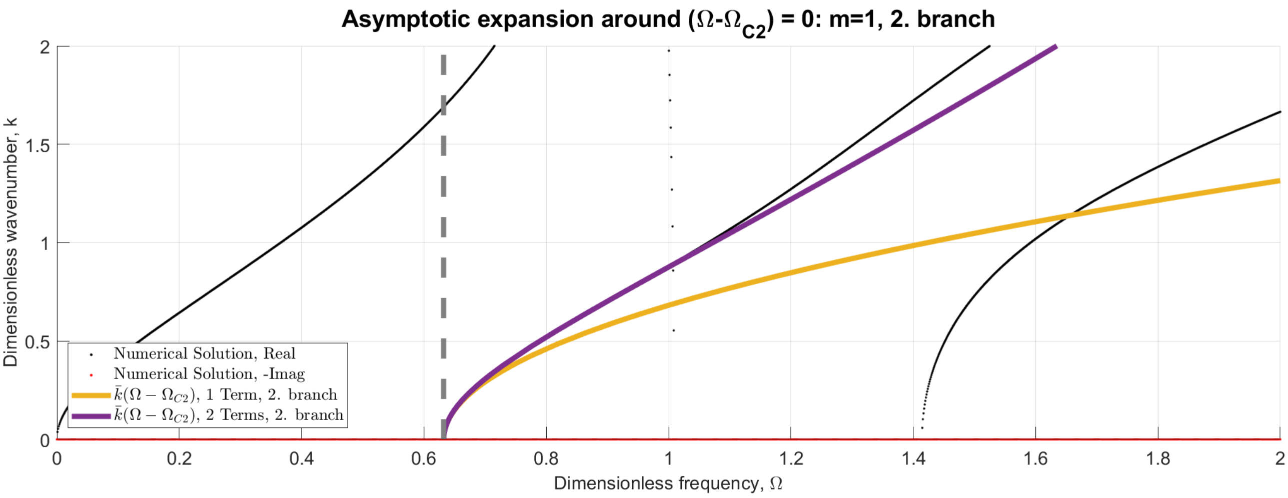

Figure 4.10: Asymptotic approximation for the second branch overlaid with the numerical solution ($m = 1$).

Asymptotic expansion for the third branch

Continuing the analysis for the third branch, the proposed expansion will be repeated from before but for the cut-on frequency Ω_{C3}. This proposed expansion is written out as (4.28).

$$\bar{K}(\Omega - \Omega_{C3}) = x_0 \left(\Omega - \sqrt{2t^2 + 2}\right)^{\frac{1}{2}} \tag{4.28}$$

[†]The cut-on frequencies are evaluated using values from Table 4.1.

Performing the expansion for the third branch, and disregarding terms above order $\mathcal{O}(\Omega^2)$ the solution for x_0 is found as (4.29). The first term is deemed sufficient to describe the dispersion curve, and the second term is therefore not determined. The asymptotic approximation is overlaid with the numerical solution for the third branch in Figure 4.11.

$$x_0 = 2^{3/4}\sqrt{\frac{(t^2+1)^{1/2}(4t^2+\nu+3)}{-2\nu^2t^2+2\nu^2-8\nu t^4-3\nu t^2+\nu+16t^4+13t^2+1}} \tag{4.29}$$

It can be seen how the asymptotic approximation traces the numerical solution up to around $\Omega = 1.45$, from where it starts over-predicting the wave numbers. The general trend beyond $\Omega = 1.45$ is still very similar to the numerical solution, and so the solution is deemed sufficient to obtain information on the acoustic black hole performance.

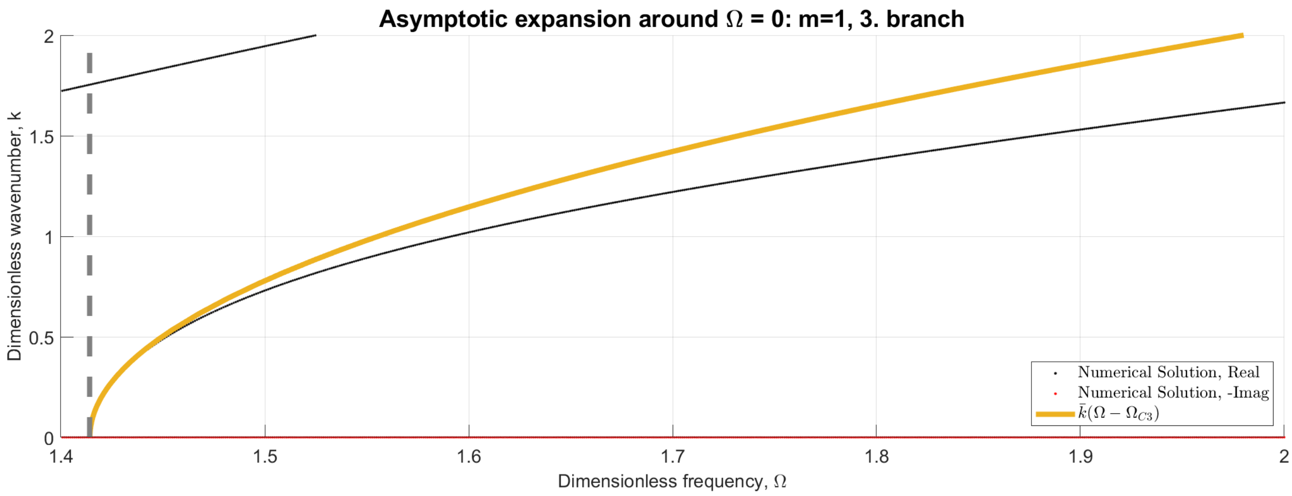

Figure 4.11: Asymptotic approximation for the third branch overlaid with the numerical solution ($m = 1$).

4.2.2 Analyzing acoustic black hole effect for $m = 1$

Having obtained asymptotic approximations for the bending mode, $m = 1$, the acoustic black hole effect can now be investigated. Before investigating the effect through asymptotic approximations, two simplified models are investigated to get a better understanding of the bending mode. First, the vibrations of a simple Bernoulli Euler beam are investigated much like what was done in Chapter 3, having a hollow circular cross-section. Next, a reduced-order model of the beam-like vibrations of a cylindrical shell is investigated. Following these, the asymptotic approximations will be used to analyze the acoustic black hole effect for $m = 1$.

4.2.2.1 The Bernoulli Euler beam model

The analysis will be performed, for a simple beam with a hollow circular cross-section. The dispersion relations for the BE beam were derived as (3.3) on page 4, and are repeated here for convenience as (4.31).

$$EI\hat{k}^4 + \rho A\omega^2 = 0 \tag{4.30}$$

$$k_{1,2} = \pm\sqrt[4]{\frac{\rho A}{EI}}\sqrt{\omega}, \qquad k_{3,4} = \pm i\sqrt[4]{\frac{\rho A}{EI}}\sqrt{\omega} \tag{4.31}$$

The area, A, and moment of inertia, I, for the cross-section of a cylindrical shell are given as (4.32). Here R_O and R_I are the outside and inside radius respectively, while h and R are the shell thickness and mid-surface radius as usual.

$$A = \pi 4(R_O^2 - R_I^2) = 2\pi R h \tag{4.32}$$

$$I = \frac{\pi}{4}(R_O^4 - R_I^4) = \frac{\pi R h(4R^2 + h^2)}{4} \tag{4.33}$$

Substituting the expressions for A and I into the real positive root of (4.31), one obtains (4.34). From here, phase and group speeds are determined as (4.35) and (4.36) respectively. It is seen how the phase and group speeds do not go to zero, for vanishing small shell thicknesses $h \to 0$. This indicates, that in the Bernoulli-Euler framework, the shell is still predicted to attain some bending stiffness for infinitely thin shells. In order for the model to predict a group speed of zero, both the radius, R, and the thickness, h, must go to zero.

$$k = \sqrt[4]{\frac{8\rho\omega^2}{E(4R^2 + h^2)}} \tag{4.34}$$

$$c_p = \frac{\omega}{k} = \frac{\omega^{1/2}}{\sqrt[4]{\dfrac{8\rho}{E(4R^2 + h^2)}}} \tag{4.35}$$

$$c_g = \frac{\partial \omega}{\partial k} = \sqrt[4]{\frac{2E(4R^2 + h^2)}{\rho}}\sqrt{\omega} \tag{4.36}$$

The acoustic black hole effect is now calculated using a termination profile similar to the one presented in Figure 4.6 and Table 4.1 on page 16, where $h \to 0$. This resulted in reflection coefficients very close to unity for all frequencies, indicating no acoustic black hole effect appearing from this type of termination profile. To investigate the acoustic black hole effect in the framework of this simple beam model, a new termination profile is proposed, where the ratio between h and R is kept constant, while gradually reducing both following a power law profile. This will essentially reduce the geometry to a hollow fiber at the tip of the acoustic black hole. The termination profile is presented as (4.37), where it can be seen how a constant ratio between h and R is maintained throughout the termination profile. The termination profile is defined by the parameters presented in Table 4.2, and is visualized in Figure 4.12, though not to scale.

$$R(x) = \epsilon x^n + R_r; \qquad h(x) = \frac{h_0}{R_0} R(x) \tag{4.37}$$

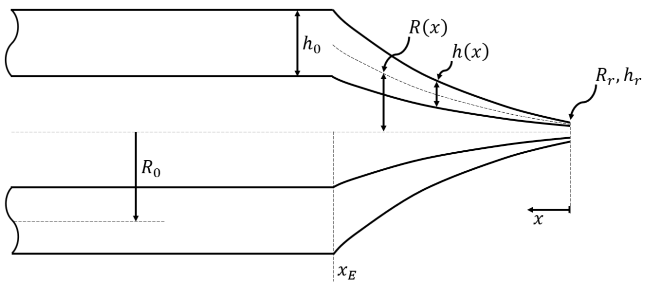

Figure 4.12: Termination profile of cylindrical shell where $h, R \to 0$, while ratio h/R is kept constant.

l	2 m	Termination profile length
h_0	0.005 m	Shell thickness outside acoustic black hole
R_0	0.2 m	Shell radius outside acoustic black hole
$\frac{h_0}{R_0}$	0.025	Constant ratio between shell thickness and radius
R_r	0.01 m	Residual radius at tip of acoustic black hole
ρ	7800 $\frac{\text{kg}}{\text{m}^3}$	Material density
E	210 MPa	Young's Modulus
η	0.05	Complex material loss
n	2	Power-law termination profile power

Table 4.2: Dimensions of analyzed cylindrical shell with power-law termination profile reducing shell to a hollow fiber.

The acoustic black hole effect is investigated using dimensional parameters for this type of termination, as it simplifies the calculations substantially compared to calculating the reflection coefficient using dimensionless parameters. The investigated frequency span is between $\omega = 0\,rad/s$ and $\omega = 5000\,rad/s$, which is equivalent to a non-dimensional frequency span of $\Omega \in [0, 0.18]$ for the given geometry presented in Table 4.2. The reflection coefficients and associated NWV are presented in Figure 4.13. Here it can be seen, how the reflection coefficient decreases with increasing frequency, reaching 0.77 at $\omega = 5000\,rad/s$. With increasing termination profile length, l, and power, n, the reflection coefficient decreased as expected. If the residual radius, R_r is set to zero, a reflection coefficient of 0 was calculated for all frequencies away from $\Omega = 0$.

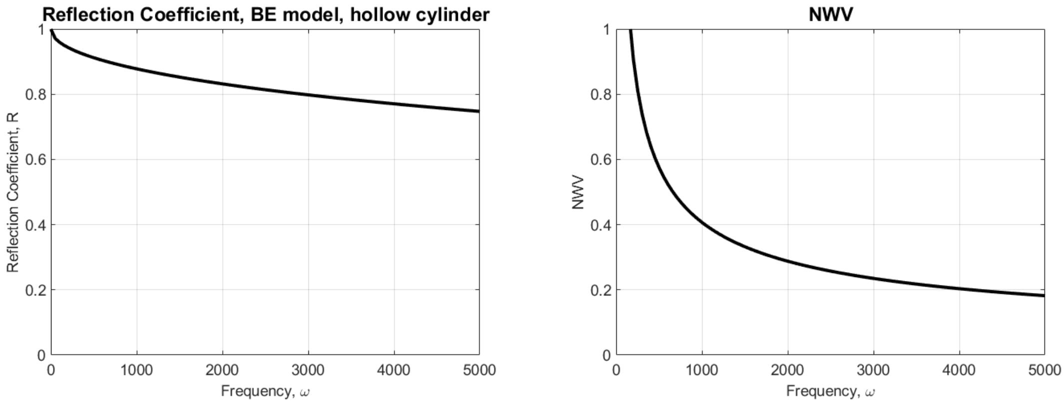

Figure 4.13: Reflection coefficient and NWV of BE-beam model with hollow circular cross-section and termination profile where $h, R \to 0$. Frequency ω in rad/s.

In this section, it was found that the elementary BE beam model requires both the radius and shell thickness to go to zero, for the group velocity to go to zero. This does not directly indicate the same to be required in the thin shell model analyzed in this chapter but hints at a flaw that might reside in the simplest of wave propagation models. To investigate this further, a reduced-order model of the beam-type motion of a cylindrical shell is investigated.

Reduced order model: Beam-type motion of cylindrical shell

In [21], a reduced-order model is presented for the beam-like motion of a cylindrical shell. The model is obtained, by assuming zero distortion of the cross-sectional shape, and by assuming a linear relationship between the slope of the shell geometry under bending, and the associated longitudinal displacements; much like the elementary Bernoulli-Euler beam theory. This reduces the 3 differential equations of motion of the original problem, to a single equation, given as (4.38), describing the simplified beam-like deflection of the cylindrical shell.

$$\frac{Eh}{1-\nu^2}\left(R^2 + \frac{h^2}{12}\right) w^{IV} + \rho h R^2 \omega^2 w^{II} - 2\rho h \omega^2 w = 0 \tag{4.38}$$

Assuming a space-harmonic solution of $w = Aexp(ikx)$, the dispersion equation and its roots are readily obtained as (4.39) and (4.40). Here, the unit-less quantities introduced in (4.8 on page 11) are employed again. Also, the parameter, $\alpha = \frac{h}{R}$, is introduced describing the ratio between shell thickness and radius. As (4.39) is a 4^{th}-order polynomial in k, 4 roots are found, two of which represent traveling waves and two of which represent evanescent waves.

$$\frac{Eh}{1-\nu^2}\left(R^2 + \frac{h^2}{12}\right) k^4 - \rho h R^2 \omega^2 k^2 - 2\rho h \omega^2 = 0 \tag{4.39}$$

$$k_{1,2} = \pm\sqrt{-\frac{6\left(\Omega\sqrt{\Omega^2 + \frac{2\,\alpha^2}{3} + 8} - \Omega^2\right)}{\alpha^2 + 12}}\,; k_{3,4} = \pm\sqrt{\frac{6\left(\Omega\sqrt{\Omega^2 + \frac{2\,\alpha^2}{3} + 8} + \Omega^2\right)}{\alpha^2 + 12}} \tag{4.40}$$

From (4.40), the phase and group speeds can be determined as (4.41) and (4.42) respectively.

$$c_p = \sqrt{\frac{\Omega\,\alpha^2 + 12\,\Omega}{6\,\Omega + 6\,\sqrt{\Omega^2 + \frac{2\,\alpha^2}{3} + 8}}} \tag{4.41}$$

$$c_g = \sqrt{\frac{\Omega\,(\alpha^2+12)\left(\Omega + \frac{\sqrt{3}\,\sqrt{3\,\Omega^2+2\,\alpha^2+24}}{3}\right)(3\,\Omega^2 + 2\,\alpha^2 + 24)}{2\left(3\,\Omega^2 + \alpha^2 + \sqrt{3}\,\Omega\,\sqrt{3\,\Omega^2 + 2\,\alpha^2 + 24} + 12\right)^2}} \tag{4.42}$$

The nature of the phase and group speed expressions can now be investigated, for vanishingly small physical dimensions of the shell. As the parameter $\alpha = \frac{h}{R}$ was introduced, the phase and group speed expressions are not given directly in terms of R and h, but setting $\alpha = 0$ is equivalent to setting $h = 0$. It is seen, that for $\alpha \to 0$, neither the group- nor phase speeds are predicted to go to zero for the reduced order model of the beam-like motion of a cylindrical shell, indicating that this type of termination profile is insufficient for obtaining the acoustic black hole effect. It was realized earlier, when investigating the group speed of bending waves for a BE beam with a hollow circular cross-section, that both the radius and shell thickness must go to zero, for a group speed of zero to be predicted. To investigate if this is also the case for the reduced order model, (4.41) and (4.42) must be investigated somewhat cleverly. One can investigate the limiting case of $(h, R) \to 0$, by assuming α to be constant and letting $R \to 0$, which will cause the shell thickness to also go to zero, $h \to 0$. Now one realizes, that the non-dimensional frequency Ω is equal to the dimensional frequency multiplied by the radius, R[†]. This means, that the action of letting $R \to 0$, is equivalent to letting $\Omega \to 0$, keeping α constant. For this limiting case, both (4.41) and (4.42) go to zero. This means, that both the elementary BE beam model, and the reduced order model for the cylindrical shell predict a group speed to become zero *only* if both the shell radius, R, and shell thickness, h, go to zero.

The reflection coefficient and NWV are now calculated for the reduced order model. Again, a termination profile is used where α is kept constant while reducing R and h following a power-law profile, see Figure 4.12. The parameters are identical to the ones presented in Table 4.2 on page 21, however with the addition of $\nu = 0.33$. The reflection coefficient and associated NWV for the reduced order model are presented in Figure 4.14. Here it is seen, that the results are practically identical to the ones obtained for the simple BE beam model in Figure 4.13 on the preceding page. It should be mentioned, that the reflection coefficients were calculated for a termination profile where only $h \to 0$, as a form of validation, but this yielded no acoustic black hole effect. In the figure it can be seen, how the reflection coefficient decreases with increasing frequency, reaching 0.77 at $\omega = 5000\,rad/s$. With increasing termination profile length, l, and power, n, the reflection coefficient decreased as expected. If the residual radius, R_r, is set to zero, a reflection coefficient of 0 was calculated for all frequencies away from $\Omega = 0$.

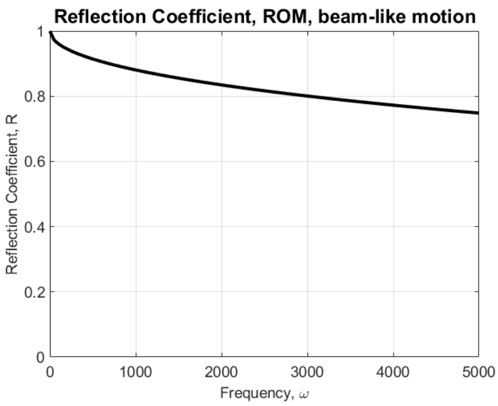

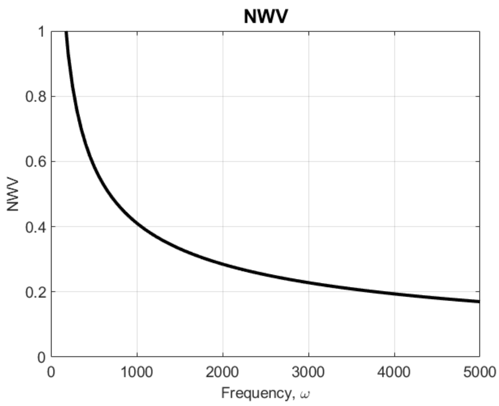

Figure 4.14: Reflection coefficient and NWV calculated for ROM of beam-like motion of cylindrical shell having termination profile where $h, R \to 0$. Frequency ω in rad/s.

[†]The non-dimensional frequency Ω is also normalized by the constant wave speed.

4.2.2.2 Analyzing the acoustic black hole effect using asymptotic approximations, $m = 1$.

At this point, having gained a better understanding of the bending mode, the acoustic black hole effect can be investigated through the asymptotic approximations for the shell model. As done previously, expressions for phase- and group speeds are derived, and afterward, reflection coefficients are determined. The analysis of the previous two simplified models of beam-like vibration showed, how both shell radius and -thickness should go to zero for the effect to occur, but this does not directly dictate, that the same holds for the full shell model, and this will be investigated in this section too.

As Ω was used as the expansion parameter for the dispersion curves of the bending mode, $m = 1$, it is very straightforward to obtain expressions for the phase- and group speeds. These are given as (4.43) and (4.44) respectively. These are, of course, general for the three branches, as the same expansion series was used for all three. For the third branch, one can simply assume $x_1 = 0$. The phase and group speeds for the 3 dispersion branches can be seen in Figure 4.15. For visual purposes, the phase and group speeds are all plotted to start from zero but should be seen as starting from their respective cut-on frequencies. As can be seen from the figure, the speeds are correctly predicted to start from zero, at their cut-on frequencies. As the frequency increases, the asymptotic approximation of the group speeds of the first two branches follow the same tendency. The third branch, however, diverges from the remaining two, as the approximation only contains a square-root term, while the first two branches also contain a $\Omega^{3/2}$-term. This means, that as the frequency increases, the group speeds of the first two branches are predicted to go to zero, while the group speed for the third branch is predicted to diverge to infinity. The nature of the predicted phase and group speeds with increasing Ω do not reflect reality and are only a result of the divergent nature of the assumed expansion series. As the first two branches contain a polynomial term with power greater than unity, the predicted group speed will inevitably be predicted to converge to zero as Ω increases. Similarly, as the third branch only contains a square root term, the group speed will inevitably be predicted to diverge to infinity as Ω increases.

$$c_p = \frac{\Omega}{\bar{k}} = \frac{\Omega}{x_0\Omega^{1/2} + x_1\Omega^{3/2}} \tag{4.43}$$

$$c_g = \frac{\partial\Omega}{\partial\bar{k}} = \frac{2\Omega^{1/2}}{x_0 + 3x_1\Omega} \tag{4.44}$$

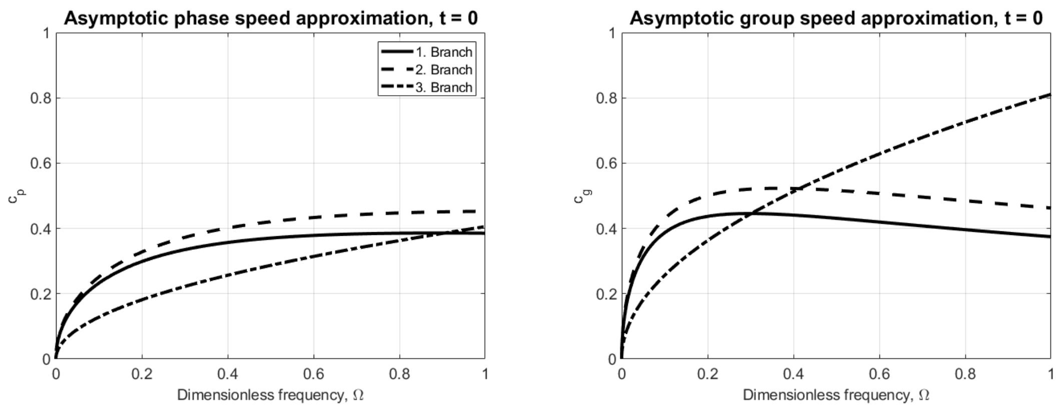

Figure 4.15: Phase- and group speeds calculated from asymptotic approximations, where $t = 0$. Each branch is presented as starting from zero but should be viewed as starting from their respective cut-on frequencies.

Figure 4.15 shows phase and group speeds for $t = 0$, equivalent to having a shell thickness of $h = 0$. Without investigating the phase and group speed expressions analytically, it is obvious from the figure, that the group speed does not go to zero for $h \to 0$. As mentioned earlier, this hints towards no acoustic black hole effect being obtained from a termination profile where only $h \to 0$. In spite of this observation, the reflection coefficient and associated NWV are calculated and presented in Figures 4.16, 4.17 and 4.18 for the first, second, and third branch respectively. The termination profile used is identical to the one used for the breathing mode, $h(x) = \epsilon x^n + h_r$ with $n = 2$. The specific parameters are listed in Table 4.1 on page 16. In the Figures, it is seen how the reflection coefficients are close to unity, for all frequencies in the range where the asymptotic approximations are representative. The associated NWV is also observed to be small for all frequencies above $\Omega = 0$. This indicates, that the employed termination profile does not give rise to the acoustic black hole effect to any meaningful extent. This is also confirmed, by a numerical parameter investigation, showing that the reflection coefficients calculated (for all of the three branches) are largely independent of n, h_r, h_0, and R_0, while being dependent on ν, l and η. No termination profile defined as $h(x) = \epsilon x^n + h_r$ would therefore result in a significant acoustic black hole effect. The only parameters which can improve the performance, and can reasonably be adjusted, are the material losses and the length of the acoustic black hole termination. These only affect the reflection coefficient, as an increase in l increases the distance the wave has to travel, and an increase in η causes a greater energy loss as it travels; not because of a cleverly chosen termination profile.

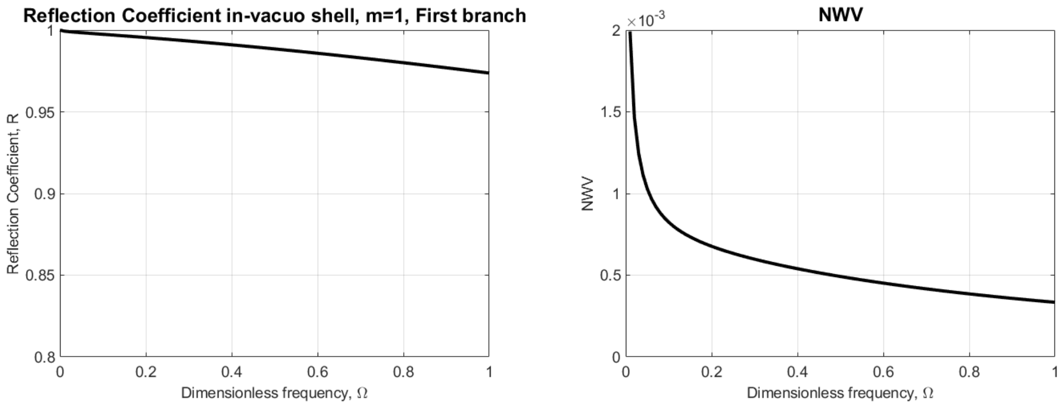

Figure 4.16: Reflection Coefficients and NWV calculated for the first branch using termination profile where $h \to 0$ ($m = 1$).

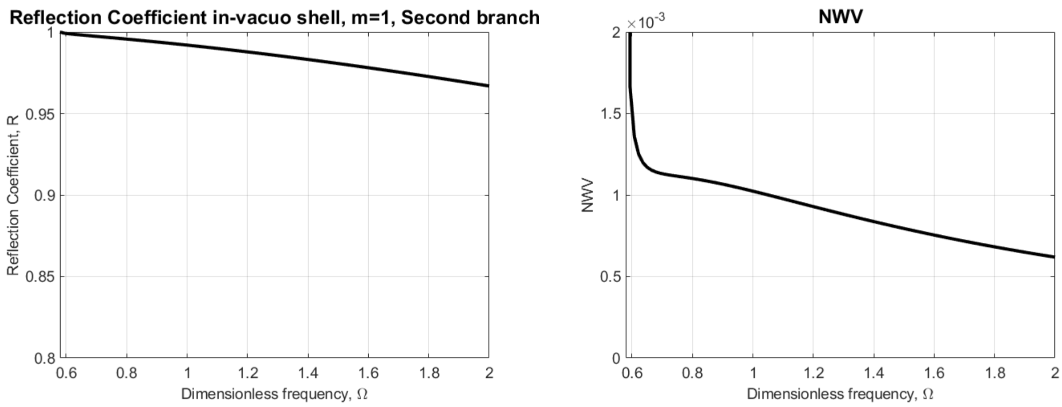

Figure 4.17: Reflection Coefficients and NWV calculated for the second branch using termination profile where $h \to 0$ ($m = 1$).

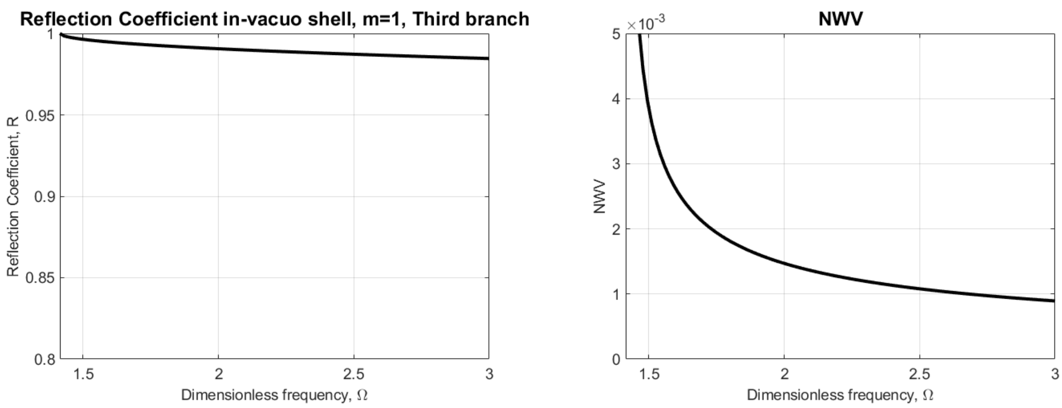

Figure 4.18: Reflection Coefficients and NWV calculated for the third branch using termination profile where $h \to 0$ ($m = 1$).

Returning to the observations made for the simple Bernoulli-Euler model and the reduced order model for beam-like vibration, it was found that the acoustic black hole effect only occurred when both the radius and thickness went to zero. Using this type of termination profile (see Figure 4.12 on page 21) for the shell model, with the properties listed in Table 4.2 on page 21 and $\nu = 0.33$, the reflection coefficient and NWV is recalculated. The reflection coefficients and NWV obtained for the first branch from this termination profile is presented in Figure 4.19. It is seen, that the results are very similar to the ones obtained for the two previous simplified models (see Figure 4.13 on page 22 and 4.14 on page 23). The same calculations are performed for the second and third branches, which also show the acoustic black hole effect. With higher frequency, the reflection coefficient and NWV reduce to zero for all 3 branches, but it happens far beyond the representative frequency range of the asymptotic approximations. The dimensional frequency range presented in the figures starts from the cut-on frequency of each branch and spans $\omega = 5000\,rad/s$. For the given geometry $\omega = 5000\,rad/s$ is approximately equivalent to 0.18 dimensionless frequency, Ω. It is also observed, that the reflection coefficient could be reduced by increasing the length of the acoustic black hole, the material loss or the n-power of the termination profile. Similarly, the reflection coefficient could be reduced by reducing the residual shell radius (and thereby residual thickness) at the tip of the acoustic black hole. This agrees with the tendencies observed for the simple BE beam analyzed in Chapter 3. Being able to affect the resulting reflection coefficient, by changing the n-power, and the residual shell radius, indicates that the termination profile in fact results in a acoustic black hole effect. For cases where the residual height is set to zero, the reflection coefficient is calculated to be zero, for all frequencies above the cut on frequency of each respective branch.

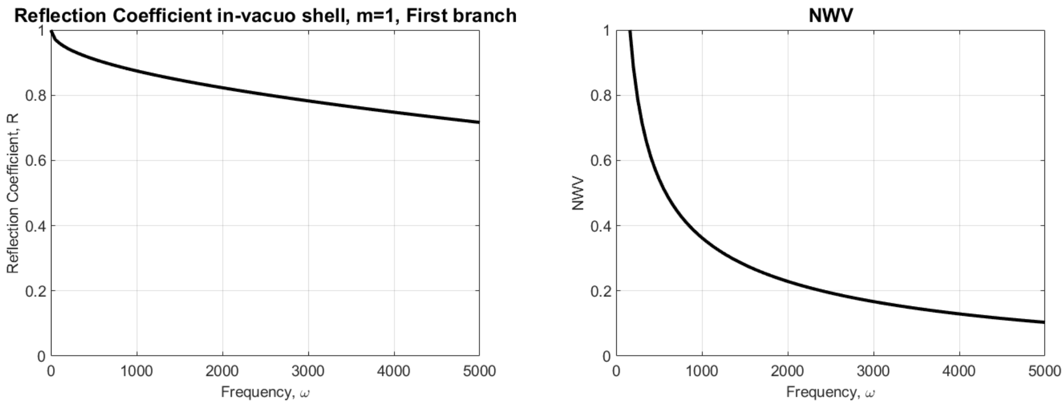

Figure 4.19: Reflection Coefficients and NWV calculated for the first branch using termination profile where $h, R \rightarrow 0$ ($m = 1$). Frequency ω in rad/s.

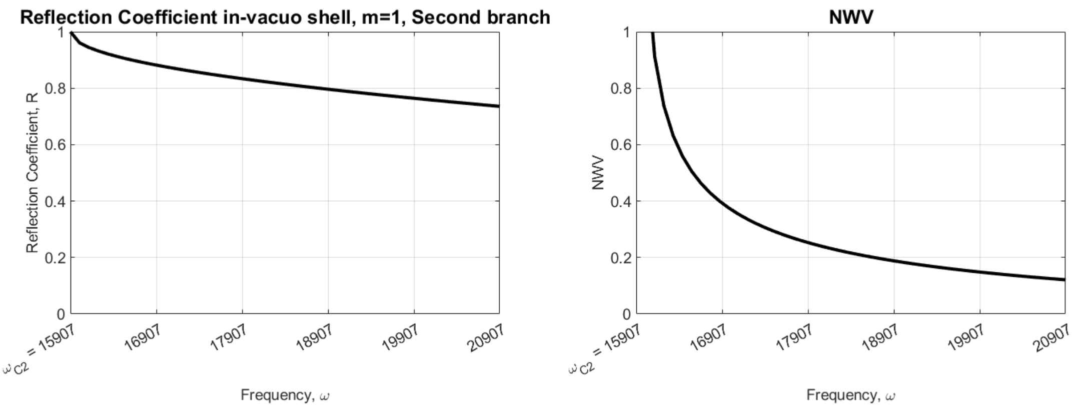

Figure 4.20: Reflection Coefficients and NWV calculated for the second branch using termination profile where $h, R \rightarrow 0$ ($m = 1$). Frequency ω in rad/s.

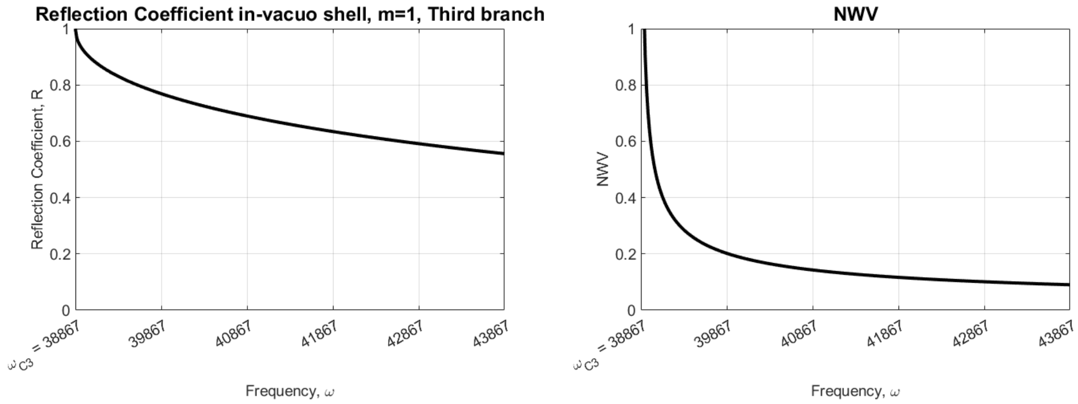

Figure 4.21: Reflection Coefficients and NWV calculated for the third branch using termination profile where $h, R \to 0$ ($m = 1$). Frequency ω in rad/s.

4.3 Investigating the ovalling mode: $m = 2$

Now, the ovalling mode, $m = 2$, is investigated. The numerical solution for the dispersion curves is presented in Figure 4.22, showing 3 purely real dispersion branches indicated by numbers from 1 to 3. The procedure for the asymptotic analysis is the same for the analysis of $m = 1$, with one difference being that no branches originate from zero for this mode. This means, that cut-on frequencies need to be determined for all 3 branches, which is done in the same manner as for $m = 1$. The resulting cut on frequencies are presented as (4.45, 4.46, 4.47), corresponding to the first, second, and third branches respectively.

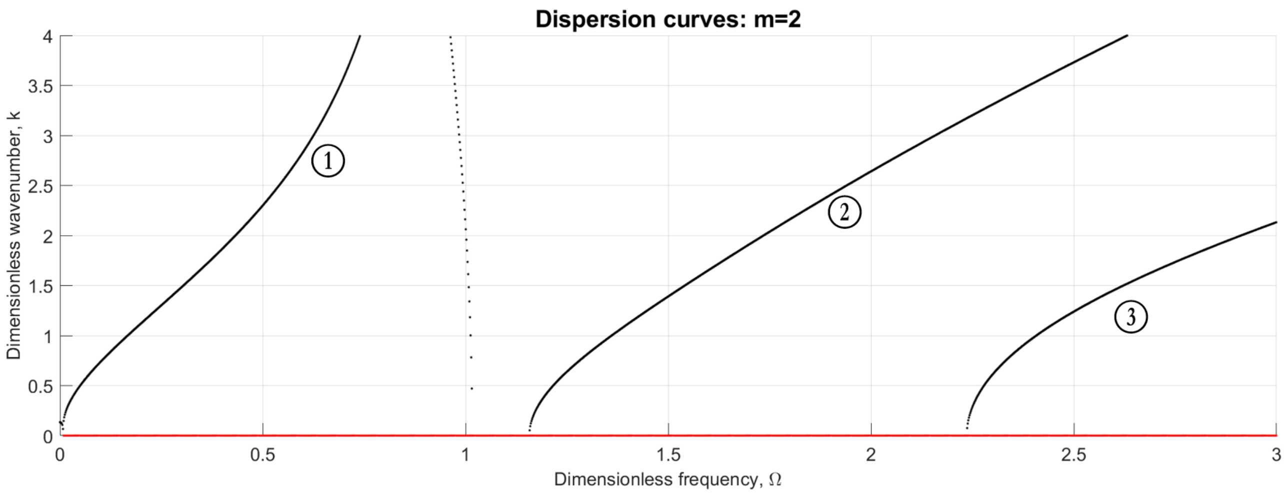

Figure 4.22: Numerical solution of dispersion branches for breathing mode, $m = 2$.

$$\Omega_{C1} = \frac{\sqrt{2}\,\sqrt{20\,t^2 - \sqrt{400\,t^4 + 56\,t^2 + 25} + 5}}{2} \approx 0.019 \tag{4.45}$$

$$\Omega_{C2} = \sqrt{2}\,\sqrt{1 - v} \approx 1.15 \tag{4.46}$$

$$\Omega_{C3} = \frac{\sqrt{2}\,\sqrt{\sqrt{400\,t^4 + 56\,t^2 + 25} + 20\,t^2 + 5}}{2} \approx 2.23 \tag{4.47}$$

4.3.1 Asymptotic expansion for $m = 2$

The asymptotic expansions are now sought for the 3 purely real branch sections of the ovalling mode. As the asymptotic analysis will be practically identical to the one performed in the previous section, only the new details of this analysis will be discussed and highlighted. The analysis is still performed using offset Ω-values as expansion parameters, as was done for $m = 1$. First, an expansion is proposed starting from the $\Omega^{\frac{1}{2}}$ power. The first expansion constant, x_0, is determined by evaluating the $\mathcal{O}(\Omega^2)$ order terms. This yielded useful expansions for the second and third branches but gave poor agreement with the first branch. This is visualized in Figure 4.23, showing how the $\Omega^{\frac{1}{2}}$-term traces the second and third branch closely, while giving poor agreement with the first branch, where the expansion overshoots the numerical solution entirely.

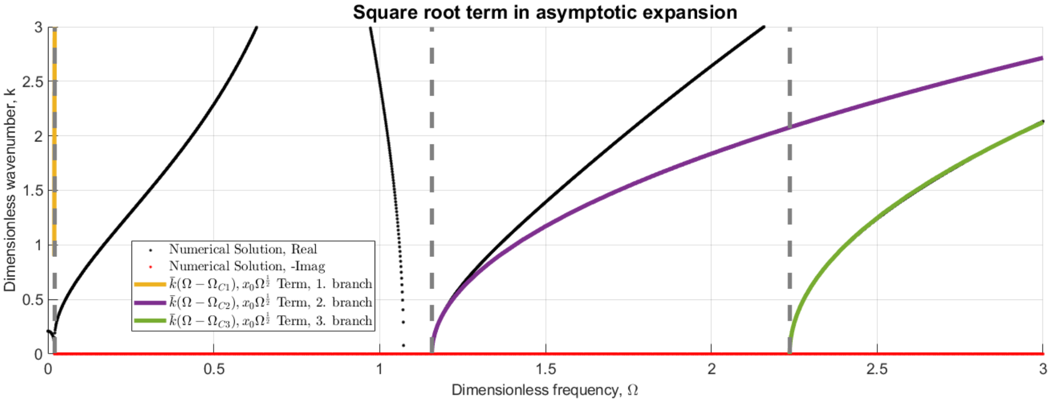

Figure 4.23: Asymptotic approximation using one term overlaid with the numerical solution.

This indicates, that the proposed expansion series starts at too large a power, and a new expansion is proposed starting at the $\Omega^{\frac{1}{4}}$ power. Again, the first expansion constant, x_0, is determined by evaluating the $\mathcal{O}(\Omega^2)$ order terms, giving good agreement with the numerical solution. The second term of the expansion series is found at the Ω^1 power, by evaluating the $\mathcal{O}(\Omega^4)$ order terms, giving the second expansion constant, x_1. The expansion series for the first branch is then found as (4.48), where the expressions for x_0 and x_1 are omitted due to their size. The asymptotic approximation can be found overlaid with the numerical solution for the first branch in Figure 4.24.

$$\bar{k}(\Omega-\Omega_{C1}) = x_0\Omega^{\frac{1}{4}} + x_1\Omega \tag{4.48}$$

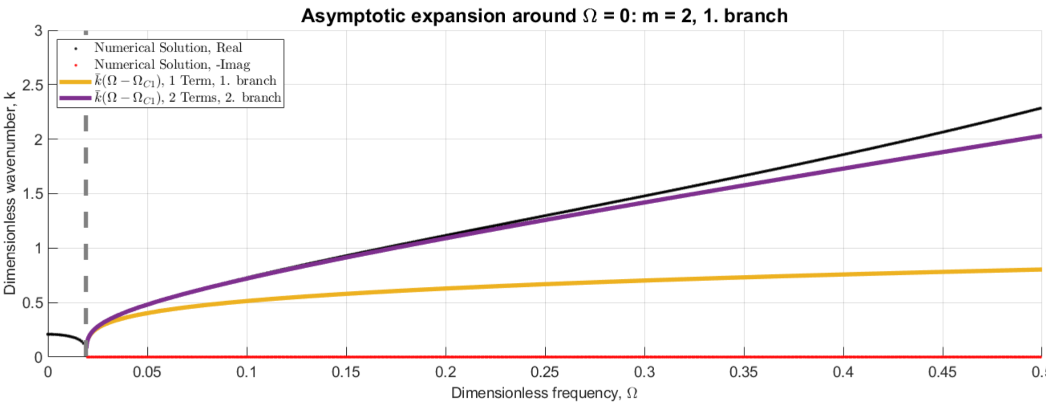

Figure 4.24: Asymptotic approximation for the first branch overlaid with numerical solution.

The expansion series of the second branch is set to start at the $\Omega^{\frac{1}{2}}$ power, as it gives good agreement with the numerical solution. The second term of the expansion series is found at the $\Omega^{\frac{3}{2}}$ power, by evaluating the $\mathcal{O}(\Omega^3)$ order terms, giving the second expansion constant, x_1. The expansion series for the second branch is then found as (4.49), where the expressions for x_0 and x_1 are also omitted. The asymptotic approximation can be found overlaid with the numerical solution for the first branch in Figure 4.25.

$$\bar{k}(\Omega-\Omega_{C2}) = x_0\Omega^{\frac{1}{2}} + x_1\Omega^{\frac{3}{2}} \tag{4.49}$$

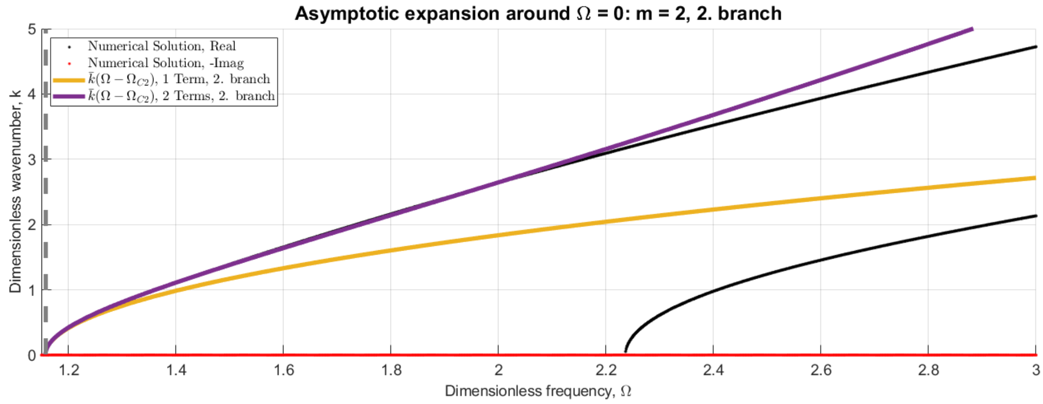

Figure 4.25: Asymptotic approximation for the second branch overlaid with numerical solution.

It is concluded, that the first term of the expansion series is sufficient to describe the dispersion phenomenon of the third branch, and so a second term is not found. The expansion series is given by (4.50), and the asymptotic approximation can be found overlaid with the numerical solution for the third branch in Figure 4.26.

$$\bar{k}(\Omega - \Omega_{C3}) = x_0 \Omega^{\frac{1}{2}} \tag{4.50}$$

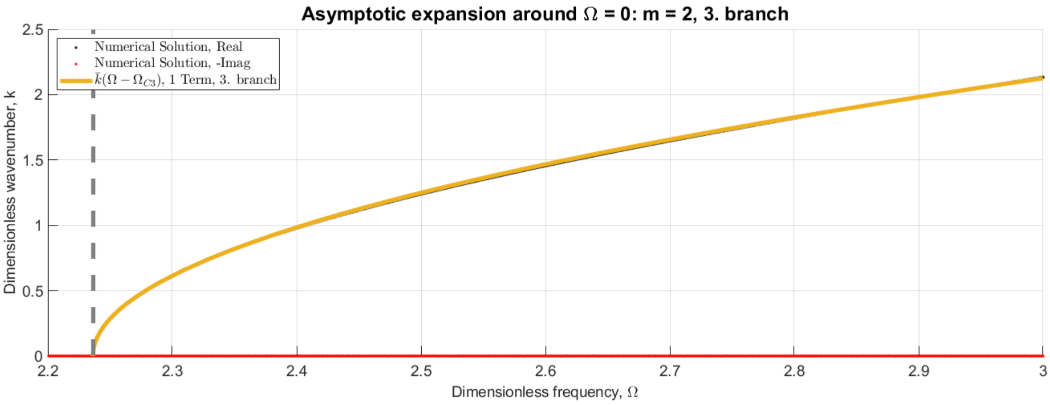

Figure 4.26: Asymptotic approximation for the third branch overlaid with numerical solution.

4.3.2 Analyzing the acoustic black hole effect for $m = 2$

Now, the reflection coefficient and NWV are calculated based on the obtained asymptotic approximations for the ovalling mode, $m = 2$. First, the calculation is performed, for a termination profile where the shell thickness is reduced to zero following a power-law termination profile, given by the parameters presented in Table 4.1. These calculations showed the same tendencies as for the bending mode $m = 1$; also for the ovalling mode, the acoustic black hole effect does not occur to any usable extent for termination profiles where $h \to 0$. Figures showing the calculated reflection coefficient and associated NWV are omitted as they are thoroughly uninteresting.

Next, the calculations are performed for a termination profile where both the shell radius and thickness are reduced simultaneously, following a power-law profile, keeping their ratio constant. The results are presented in Figures 4.27, 4.28 and 4.29. Again, at higher frequencies, the reflection coefficient and NWV reduce to zero for all 3 branches, but it happens far beyond the representative frequency range of the asymptotic approximations. The dimensional frequency range presented in the figures starts from the cut-on frequency of each branch and spans $\omega = 5000\, rad/s$. For the given geometry $\omega = 5000\, rad/s$ is approximately equivalent to 0.18 dimensionless frequency, Ω. Changes in the parameters of the termination profile resulted in changes in the obtained reflection coefficient similar to what was observed for $m = 1$, and agree with the tendencies observed for the simple BE beam analyzed in Chapter 3. Being able to affect the resulting reflection coefficient, by changing the n-power, and the residual shell radius, indicates that the termination profile in fact results in a acoustic black hole effect. For cases where the residual height is set to zero, the reflection coefficient is calculated to be zero, for all frequencies above the cut on frequency of each respective branch.

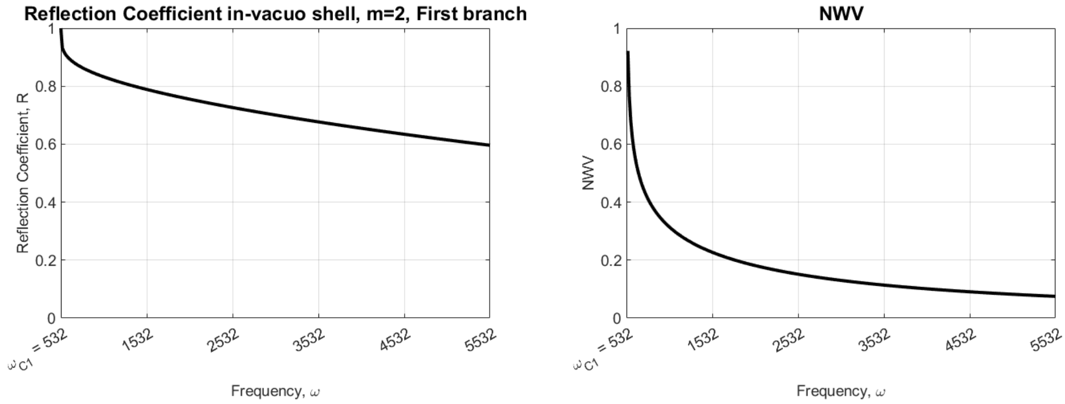

Figure 4.27: Reflection Coefficients and NWV calculated for the first branch of the cylindrical shell having termination profile where $h, R \to 0$ ($m = 2$). Frequency ω in rad/s.

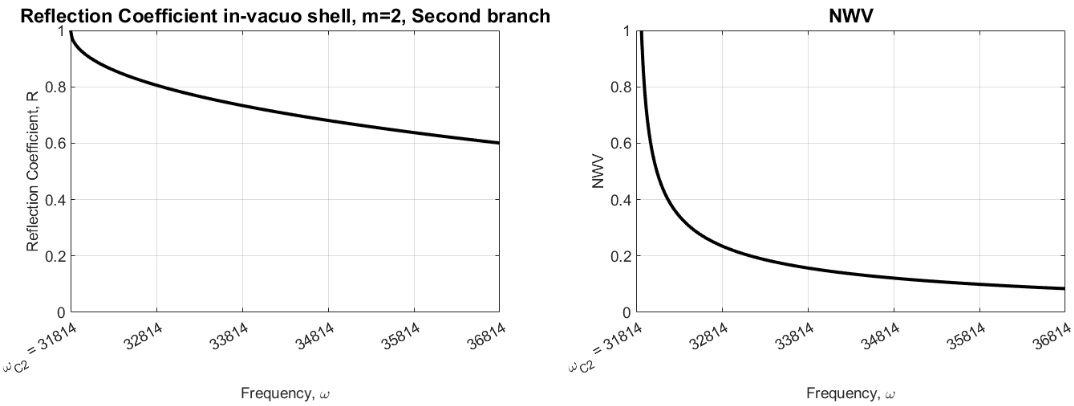

Figure 4.28: Reflection Coefficients and NWV calculated for the second branch of the cylindrical shell having termination profile where $h, R \to 0$ ($m = 2$). Frequency ω in rad/s.

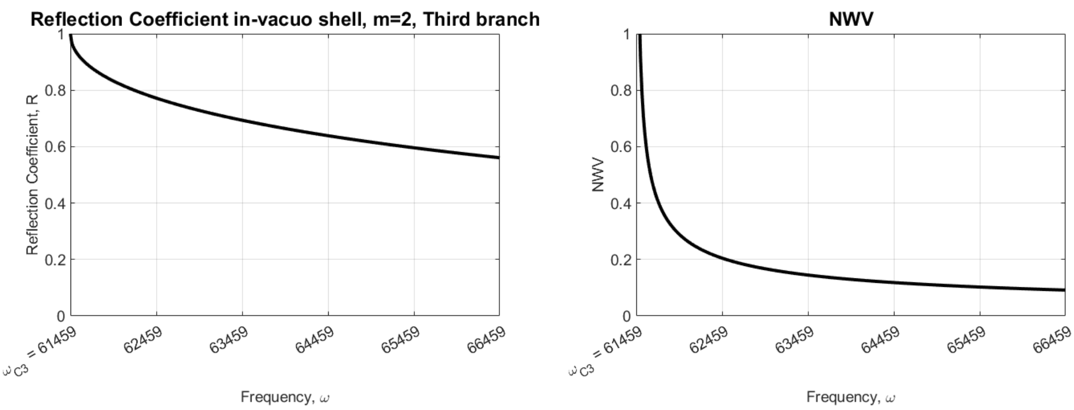

Figure 4.29: Reflection Coefficients and NWV calculated for the third branch of the cylindrical shell having termination profile where $h, R \to 0$ ($m = 2$). Frequency ω in rad/s.

4.4 Discussion of shell model validity

The chapter began with a presentation of the Goldenveizer-Novozhilov shell model which is widely employed in literature [22, 23] for the analysis of wave phenomena in thin shells. Asymptotic dispersion relations were obtained for this model, which indicated that with a vanishingly small shell thickness, the shell still retained a non-zero stiffness making it able to transmit wave energy. This went against intuition and resulted in the model not predicting the acoustic black hole effect, except if the pipe was reduced to a "hollow fiber", by reducing both the shell thickness and radius to vanishing dimensions. Assuming that the analysis performed in this chapter is correct, it is difficult to conclude whether the acoustic black hole effect can be obtained for the cylindrical shell in the low-frequency range, or whether the acoustic black hole effect cannot be modeled through the Goldenveizer-Novozhilov shell model. Since the acoustic black hole effect has been modeled and observed experimentally for plates, the author expects the effect to be obtainable for cylindrical shells also. It may be possible to more accurately predict the wave propagation properties of the cylindrical shell at the limiting cases where $h \to 0$, if a more elaborate model is employed, e.g. if the problem is investigated directly through linear elasticity. This would, however, complicate the analysis immensely, meaning that the analysis would likely be performed numerically, through e.g. finite elements, transfer matrix methods, or the Gaussian expansion method. Obtaining solutions through these methods would make it possible to determine, how the acoustic black hole effect could be obtained for the cylindrical shell by parameter studies, instead of analyzing expressions for wave numbers as was done in this chapter. As mentioned in the introduction in Chapter 1, annular acoustic black holes in cylindrical shells have been analyzed numerically, but these have been in the context of periodicity, where several acoustic black holes are placed sequentially, resulting in stop band effects, i.e. destructive interference [24]. The authors of [24, 8, 25], Jie Deng Et Al., conclude that sequential acoustic black holes can be used to reduce both mechanical vibrations, and resulting sound radiation, but comment little on whether the effect is obtained primarily due to periodicity/stop-band effects or whether it is a result of exploiting the acoustic black hole effect. In a very recent study [26], acoustic black holes in cylindrical shells are investigated through power flow analysis. Here it is found, that the acoustic black hole effect does appear for cylindrical shells having power-law termination profiles where only h is reduced. The effect is observed to be most prevalent for frequencies where the local resonance of the acoustic black hole appears, but mention how the effect is present for all frequencies. The analysis in [26] is performed based on Love's shell theory, indicating that the Goldenveizer-Novozhilov shell model is not the reason for the acoustic black hole effect not being observed through the analysis in this chapter. Because of this, the analysis of the acoustic black hole effect in cylindrical shells is continued, but a more rigorous approach is seen as necessary to identify in which situations the effect can be expected to appear.

A note on symbolic manipulators for obtaining asymptotic expansions

To aid the process of obtaining the asymptotic approximations, the symbolic toolbox in Matlab was used [27]. This toolbox allows for efficient symbolic manipulations of almost arbitrarily complex algebraic equations, making it a strong tool for applications such as this. The use of such symbolic manipulators, however, introduces a potential source of error, as the operator of the program has little insight into the assumptions that underlie the program's derivations. On several occasions, during the derivation of the asymptotic approximations for the bending mode, Matlab failed to obtain the correct solutions for the expansion constants, x_0 and x_1, although the program was given the correct equations and assumed expansions. Sometimes there would be several solutions for an expansion constant, while Matlab only managed to find a single one; sometimes Matlab simply found erroneous solutions when asked to identify terms of a given power automatically. If instead the solutions were manually expanded, and dominant terms were identified by hand, the correct expansion constants were often found. The process of solving problems using the symbolic manipulators offloads the task of performing complex and tedious algebraic expansions by hand to the computer but leaves the operator with the task of formulating the problem in a digestible way for the symbolic manipulator. Sometimes the problem needs to be recast using different constants, sometimes the problem should be reconditioned by expressing it in terms of Ω^2 instead of Ω, sometimes the problem needs to be split into smaller sub-problems. All of this makes the process of determining the correct expansion series a process governed even more by trial and error.

4.5 Answering SRQ 2

How can the acoustic black hole effect be modeled and investigated using asymptotic approximations, for a thin cylindrical shell model?

In this chapter, the acoustic black hole effect was investigated using asymptotic approximations of the wave numbers in the low-frequency range. The analysis started with an introduction of the Goldenveizer-Novozhilov shell model, and the derivation of the dispersion equation for this model. The analysis investigated the effect for the breathing mode ($m = 0$), the bending mode ($m = 1$) and finally the ovalling mode ($m = 2$).

First, an asymptotic approximation was obtained for the dispersion characteristics of the breathing mode. A termination profile was then imposed, as a power-law termination profile gradually reducing the shell thickness to zero (or rather to a small non-zero residual thickness). The following calculation of reflection coefficients indicated no acoustic black hole effect for vanishingly small shell thicknesses. This indicated that the model predicted an erroneous residual stiffness, for infinitely thin shells. Next, asymptotic approximations were obtained for the real-valued dispersion branches of the bending mode ($m = 1$). The approximations were obtained by using Ω as the expansion parameter and obtaining unique expansions for each branch respectively.

Before investigating the acoustic black hole effect using asymptotic approximations, two simplified models of beam-like vibration of a cylindrical shell were investigated. The first model was a Bernoulli-Euler beam model, using a hollow circular cross-section, and the second model was a reduced-order model derived from the full shell model. Both of these simplified models predicted the group speed to not converge to zero for vanishingly small shell thicknesses, requiring instead both shell radius, R, and shell thickness, h, to go to zero. No acoustic black hole effect was observed from the simplified models, by employing a termination profile where $h \to 0$, but the effect appeared for a termination profile where $h, R \to 0$, keeping $\alpha = \frac{h}{R}$ constant. Finally, the ovalling mode ($m = 2$) was investigated through asymptotic approximations, just as was done for the bending mode. Here, the acoustic black hole effect was also observed to appear for profiles where $h, R \to 0$, while not appearing for profiles where only $h \to 0$.

In a short discussion, it was mentioned, that the Goldenveizer-Novozhilov shell model still predicted the ability to carry wave energy for vanishingly small shell thicknesses, which went against intuition and resulted in the acoustic black hole effect not appearing when a termination profile of $h \to 0$ was used. It was discussed how a more thorough analysis through e.g. linear elasticity might be able to predict the acoustic black hole effect for thin shells, but this may limit the analysis to numerical solutions.

SRQ 3: Investigating the differential equations of motion 5

In this chapter, SRQ 3 will be answered by investigating the differential equations of motions driving the acoustic black hole effect. In Chapter 4, it was presented how the acoustic black hole effect could be obtained for cylindrical shells if both the shell thickness and radius go to zero. This went somewhat against intuition, as the flexural rigidity of the shell should go to zero as the shell thickness alone goes to zero. To gain a better understanding of why the acoustic black hole effect is not predicted when the shell thickness goes to zero, a more rigorous investigation will be performed, by investigating the underlying differential equations of motion directly.

First, an investigation of the acoustic black hole effect for the flat plate is presented having a power-law termination profile, and it is shown that the effect appears for this geometry using a termination profile where $h \to 0$. It is discussed why the effect appears for this geometry, and why it does not appear for the curved plate (cylindrical shell). Next, based on this new-found understanding of the driving mechanisms behind the acoustic black hole effect, geometric- and material assumptions are imposed for the cylindrical shell model in an attempt to obtain the effect for this special case. Finally, the analysis returns to the original shell model, and the acoustic black hole effect is re-investigated.

5.1 Investigating the flat plate

The analysis of the acoustic black hole effect for the flat plate starts from (5.1), and follows the derivation presented in [28]. The differential equation, (5.1), describes the flexural motion, $W_w(x, y, t)$, of a termination profile "wedge" on a plate, thereby assuming a spatial dependency of the plates flexural rigidity, $D_w(x)$. The equation is also expressed through the instantaneous height of the wedge, $h_w(x)$, and the material density of the wedge, ρ_w, which is assumed constant for simplicity. In the following derivation, the subscript, w, refers to the wedge geometry. The geometry is presented in Figure 5.1.

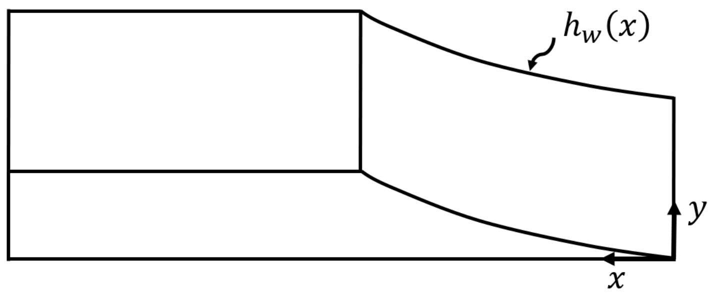

Figure 5.1: Flat plate geometry with termination profile on the left-hand side. Termination profile height is given by expression $h_w(x)$

.

$$\frac{\partial^2}{\partial x^2}\left[D_w\left(\frac{\partial^2 W_w(x,y,t)}{\partial x^2}+\nu\frac{\partial^2 W_w(x,y,t)}{\partial y^2}\right)\right]+2(1-\nu)\frac{\partial^2}{\partial x\partial y}\left[D_w\frac{\partial^2 W_w(x,y,t)}{\partial x\partial y}\right]$$
$$+\frac{\partial^2}{\partial y^2}\left[D_w\left(\frac{\partial^2 W_w(x,y,t)}{\partial y^2}+\nu\frac{\partial^2 W_w(x,y,t)}{\partial x^2}\right)\right]+\rho_w h_w(x)\frac{\partial^2 W_w(x,y,t)}{\partial t^2}=0 \tag{5.1}$$

An ansatz for the solution of (5.1) is proposed as (5.2) having a space-dependent amplitude, $B(x)$. The x-wave number is expressed through the position-independent plate wavenumber, $k_p^2 = \frac{\omega^2\rho_w(1-\nu_w^2)}{E_w}$, and the function $S(x)$. $S(x)$ is the x-dependent part of the Eikonal function, $S(x,y) = S(x) + k_y y$, and it can be seen how this Eikonal function is used to express wave numbers through its gradients. Expressing the x-wave number in this manner, means, that if it is possible to show that the function $S(x)$ diverges for some termination profile, the wavenumber will grow unbounded, resulting in the acoustic black hole effect c.f. Chapter 3. The y-wave number and time dependency are included in the ansatz in the typical manner.

$$W_w(x,y,t) = \underbrace{B(x)}_{\text{Amp.}}\,\underbrace{exp(ik_pS(x))}_{\text{x-wave}}\,\underbrace{exp(ik_yy)}_{\text{y-wave}}\,\underbrace{exp(-i\omega t)}_{\text{Time}} \tag{5.2}$$

Substituting (5.2) into (5.1), a sizeable equation is obtained, which is only presented in Appendix B. A leading order approximation of this equation is obtained, by neglecting all but the higher order terms; i.e. neglecting higher order derivatives and products of derivatives. The higher order terms have been highlighted in red in Appendix B, for convenience. The leading order approximation is obtained as (5.3), and is easily rewritten to the bi-quadratic equation (5.4) in terms of the derivative of $S(x)$.

$$-\rho_w B(x)h_w(x)\omega^2 + D_w(x)B(x)k_p^4\left(\frac{\partial S(x)}{\partial x}\right)^4 + 2D_w(x)k_y^2B(x)k_p^2\left(\frac{\partial S(x)}{\partial x}\right)^2 + D_wB(x)k_y^4 = 0 \tag{5.3}$$

$$\left(\frac{\partial S(x)}{\partial x}\right)^4 + \left(\frac{\partial S(x)}{\partial x}\right)^2\left(\frac{2k_y^2}{k_p^2}\right) + \left(\frac{k_y^4}{k_p^4}\right) - \left(\frac{\rho_w h_w(x)\omega^2}{D_w(x)k_p^4}\right) = 0 \tag{5.4}$$

The four roots of this equation are given as (5.5) which is rewritten to (5.6), by expressing the instantaneous flexural rigidity as $D_w(x) = \frac{E_wh_w(x)^3}{12(1-\nu^2)}$, and expressing the instantaneous wedge height as a power law profile, $h_w(x) = \epsilon x^n$. Here, the constant $\gamma = \frac{\sqrt{12}k_p}{\epsilon k_y^2}$ is introduced to simplify the expression.

$$\frac{\partial S(x)}{\partial x} = \pm\left(\frac{-k_y^2}{k_p^2} \pm \sqrt{\frac{\omega^2 h_w(x)\rho_w}{D_w(x)k_p^4}}\right)^{1/2} \tag{5.5}$$

$$\frac{\partial S(x)}{\partial x} = \pm\frac{k_y}{k_p}\left(-1 \pm \gamma x^{-n}\right)^{1/2} \tag{5.6}$$

Now, to obtain a solution for $S(x)$, the expression in (5.6) must be integrated with respect to x, which is not an easy task to do directly. In order to approximate a closed-form solution for $S(x)$, (5.6) is expressed through a binomial expansion truncated at the third term. This expansion is then integrated, to obtain (5.7,5.8). The two remaining expressions for $S_{3/4}(x)$ are simply the negative of $S_{1/2}(x)$.

$$S_1(x) = \sqrt{\frac{12^{1/2}}{(\epsilon k_p)(1-n/2)^2}}x^{(1-n/2)} - \frac{1}{2}\sqrt{\frac{k_y^4\epsilon}{12^{1/2}k_p^3(1+n/2)^2}}x^{(1+n/2)} - \frac{1}{8}\sqrt{\frac{k_y^8\epsilon^3}{12^{3/2}k_p^5(1+3n/2)}}x^{(1+3n/2)} \tag{5.7}$$

$$S_2(x) = i\sqrt{\frac{12^{1/2}}{(\epsilon k_p)(1-n/2)^2}}x^{(1-n/2)} + \frac{i}{2}\sqrt{\frac{k_y^4\epsilon}{12^{1/2}k_p^3(1+n/2)^2}}x^{(1+n/2)} - \frac{i}{8}\sqrt{\frac{k_y^8\epsilon^3}{12^{3/2}k_p^5(1+3n/2)}}x^{(1+3n/2)} \tag{5.8}$$

Looking at the first term, in the above expressions, it can be seen how the integral diverges for $n = 2$. It is also seen, how the integral diverges for $n \geq 2$ provided that the integral is performed across the singularity at $x = 0$, i.e. to the point of the truncation profile where the thickness goes to zero. Any truncation of the termination profile by a residual height at the tip will cause the integral of $\frac{\partial S}{\partial x}$ to converge, causing the acoustic black hole effect to be reduced. It has thereby been shown, starting from the differential equation of motion, how the acoustic black hole effect can be obtained for the case of a flat plate, with a power-law termination profile of power $n \geq 2$. As the effect is present for this geometry, some effort is invested into studying the nature of (5.3). Looking at the equation, it is apparent that all terms contain the factor $h(x)$ either explicitly or through the $D_w(x)$-term. Through the rewriting to 5.4, it is seen how the term containing ω is dependent on $h(x)^{-2}$, while all other terms are independent of $h(x)$. This means, that as $h \to 0$, the term containing ω will grow unbounded. For the equation to be balanced for a given ω as $h(x) \to 0$, the terms independent of $h(x)$, namely terms containing $\frac{\partial S(x)}{\partial x}$, must grow unbounded at a comparable rate. This in turn causes the phase- and group speeds to reduce to zero, resulting in the acoustic black hole effect. Returning to the dispersion relation (3.8) for the simple Bernoulli Euler beam analyzed in Chapter 3 on page 4, it can be investigated if the same argumentation holds. The acoustic black hole effect was present for this geometry, and one can again see how as $h(x)$ goes to zero, k_x must grow unbounded for any given value of ω to balance the equation. However, if one investigates the asymptotic solutions obtained for the cylindrical shell in Chapter 4, it is seen how none of the solutions for the wave numbers grow unbounded as $t \to 0$, and how the acoustic black hole effect was absent in all these cases.

As the effect has been shown to appear for the completely flat plate, the next natural step is to investigate the curved plate, which is essentially a section of the cylindrical shell investigated in Chapter 4. The geometry of this curved plate is presented in Figure 5.2 by the solid lines. The dashed lines serve to indicate how the curved plate is a section of the previously analyzed cylindrical shell. The boundary conditions are such that longitudinal and radial motion is free, while circumferential motion is constrained. Though the figure indicates a plate of finite length, the analysis still concerns itself with infinite waveguides.

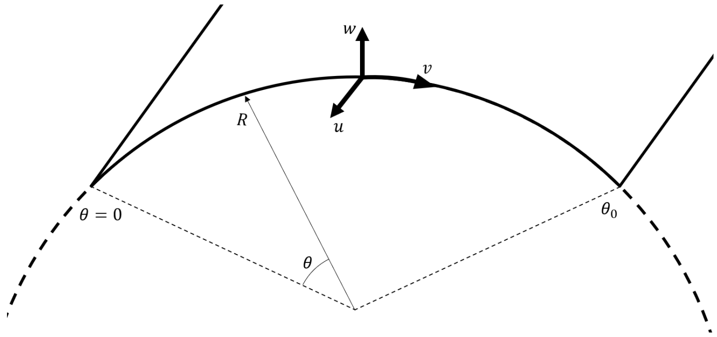

Figure 5.2: Curved plate geometry indicated by solid lines. Dashed lines indicate how the geometry is effectively a section of a full cylindrical shell. Angular span is given by θ_0, while mid plane radius is given by R.

Next, the differential equations of motion will be formulated for the curved plate. This could be done rigorously by the Hamiltonian principle, but a shortcut is exploited instead, and the differential equations of motion for the curved plate are instead "reconstructed" from the equations for the cylindrical shell in (4.1, 4.2, 4.3) on page 10. The solution ansatz used to obtain the equations on page 10, were in the form (5.9). This means, that in each term where the m-factor appears in the original cylindrical shell equations, a derivative has been performed with respect to θ. By substituting the m-factors with differential operations, keeping close track of the sign changes that occur when performing derivatives of the trigonometric functions, the expanded equations are obtained as (5.10, 5.11, 5.12).

$$u(x,\theta,t) = \sum_m u_m(x,t)cos(m\theta); \quad v(x,\theta,t) = \sum_m v_m(x,t)sin(m\theta); \quad w(x,\theta,t) = \sum_m w_m(x,t)cos(m\theta) \tag{5.9}$$

$$\frac{d^2u}{dx^2} + \frac{1-\nu}{2}\frac{1}{R^2}\frac{\partial^2 u}{\partial\theta^2} + \frac{1+\nu}{2}\frac{1}{R}\frac{\partial^2 v}{\partial x\partial\theta} + \frac{\nu}{R}\frac{dw}{dx} - \frac{\rho\omega^2(1-\nu^2)}{E}u = 0 \tag{5.10}$$

$$\begin{aligned}&\frac{1+\nu}{2}\frac{1}{R}\frac{\partial^2 u}{\partial x\partial\theta} + \frac{1-\nu}{2}\frac{d^2v}{dx^2} + \frac{1}{R^2}\frac{\partial^2 v}{\partial\theta^2} + \frac{h^2}{12}\frac{2(1-\nu)}{R^2}\frac{d^2v}{dx^2} + \frac{h^2}{12}\frac{1}{R^4}\frac{\partial^2 v}{\partial\theta^2}\\&+\frac{1}{R^2}\frac{\partial w}{\partial\theta} - \frac{h^2}{12}\frac{1}{R^4}\frac{\partial^3 w}{\partial\theta^3} - \frac{h^2}{12}\frac{(2-\nu)}{R^2}\frac{\partial^3 w}{\partial x^2\partial\theta} - \frac{\rho\omega^2(1-\nu^2)}{E}v = 0\end{aligned} \tag{5.11}$$

$$\begin{aligned}&\frac{\nu}{R}\frac{du}{dx} + \frac{1}{R^2}\frac{\partial v}{\partial\theta} - \frac{h^2}{12}\frac{1}{R^4}\frac{\partial^3 v}{\partial\theta^3} - \frac{h^2}{12}\frac{(2-\nu)}{R^2}\frac{\partial^3 v}{\partial x^2\partial\theta} + \frac{1}{R^2}w\\&+\frac{h^2}{12}\frac{d^4w_m}{dx^4} + \frac{h^2}{12}\frac{2}{R^2}\frac{\partial^4 w}{\partial x^2\partial\theta^2} + \frac{h^2}{12}\frac{1}{R^4}\frac{\partial^4 w}{\partial\theta^4} - \frac{\rho\omega^2(1-\nu^2)}{E}w = 0\end{aligned} \tag{5.12}$$

From here, it is possible to impose a new solution ansatz to the differential equations, consistent with the boundary conditions of the curved plate geometry. This is done in the form (5.13), where m' is the circumferential wavenumber and θ_0 is the angular span of the curved plate, see Figure 5.2. The ansatz still makes use of the orthogonality of the trigonometric functions, allowing each of the m-spectrum to be analyzed independently. This solution ansatz assumes the edges of the curved plate to be free in the u- and w-directions, but assumes zero motion in the v-direction (circumferential motion) at the edges. As the flexural motion is free at the edges, the model is reminiscent of the flat plate analyzed previously, however with the inclusion of coupling terms between the displacement directions appearing due to the curvature of the geometry.

$$u = \sum_m u_m(x,t) cos\left(\frac{\pi m'\theta}{\theta_0}\right); \quad v = \sum_m v_m(x,t) sin\left(\frac{\pi m'\theta}{\theta_0}\right); \quad w = \sum_m w_m(x,t) cos\left(\frac{\pi m'\theta}{\theta_0}\right) \tag{5.13}$$

When employing the ansatz of (5.13), an unfortunate observation is however made. As the new ansatz of (5.13) is identical to the previous ansatz of (5.9), except for the arguments of the trigonometric functions, the equations obtained from the new ansatz are also almost identical. The only difference is the circumferential wavenumber of the cylindrical shell, m, being replaced by an expression containing the circumferential wavenumber of the curved plate: $\frac{\pi m'}{\theta_0}$. These newly obtained equations could be analyzed using the same naive asymptotic expansions as was done in Chapter 4, but this would yield no new information. This is because analyzing the dispersion characteristics of a given m'-spectrum of the curved plate is equivalent to analyzing a higher order m-spectrum of the full cylindrical shell. The reason for this is explained visually in Figure 5.3, where the faint black line shows the different m-orders for the full cylindrical shell, while the solid black line shows the m'-orders of the curved plate, assuming $\theta_0 = \pi/2$. From the figure, it becomes obvious, that investigating the m-order of the full cylindrical shell is equivalent to investigating the $2m'$-order of the curved plate (specifically for the example $\theta_0 = \pi/2$).

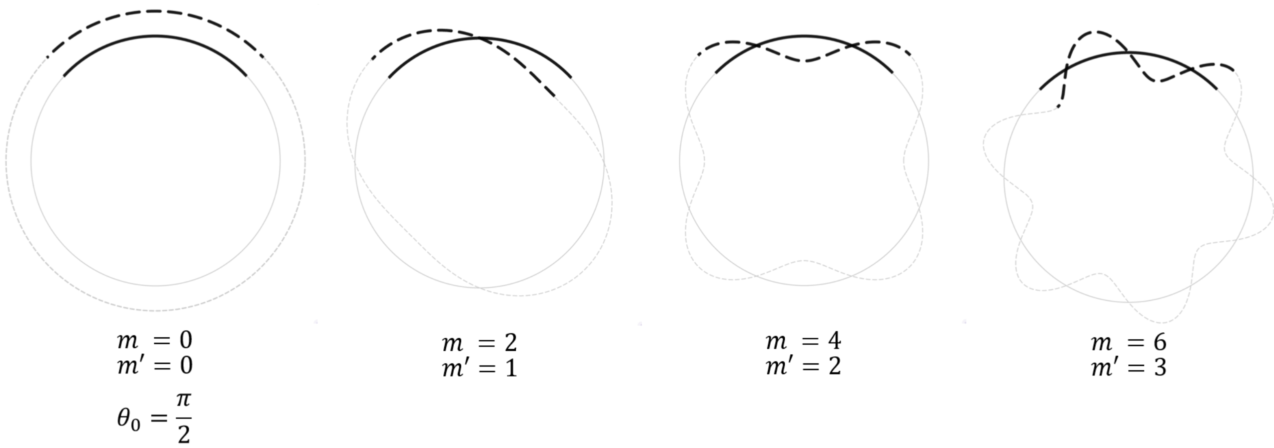

Figure 5.3: Visual representation of how m'-order is equivalent to a higher m-order.

As the analysis of the curved plate is functionally the same as the analysis of the full cylindrical shell, it can be concluded that the acoustic black hole effect does not occur for the curved plate either. This means, that there is a form of discontinuity when going from a perfectly flat plate where the effect is present, to a plate with even the slightest curvature, where the effect is absent. As the effect is present in the first case and not present in the second, it must be possible to determine some fundamental difference between the two models, which could cause the discontinuity. It will be attempted to identify this difference, by an investigation of the differential equations of motion.

The investigation will begin with the simplest case of $m = 0$. The differential equation governing the flexural motion of the full cylindrical shell ((4.1) on page 10) reduces to (5.14) when setting $m = 0$. If one assumes a non-zero curvature of the plate it is seen how the equation governing the flexural motion of the curved shell is coupled with the axial motion u_m, through Poisson effects. This Poisson coupling to the longitudinal motion is not present in the model for the flat plate, and may thereby be the reason why the acoustic black hole effect does not appear. This can be investigated quite simply, by setting $\nu = 0$, and investigating the dispersion characteristics of the breathing mode under this material assumption.

If one assumes a material with $\nu = 0$, the equation reduces to (5.15), and it can be seen how this is equivalent to a curved plate on a classical Winkler foundation. Assuming a spatial solution of $w_m = Wexp(ik_x x)$, the dispersion equation is obtained as (5.16), or using the unit-less parameters from page 11 as (5.17). Here an interesting observation is made, as this unit-less dispersion equation was already obtained previously in the report as (4.9) on page 11. The roots were also obtained as (4.14) on page 13 during the asymptotic analysis of the breathing mode, but the expansion was never pursued for this branch as it did not originate from zero.

$$\frac{\nu}{R}\frac{du_m}{dx} + \frac{1}{R^2}w_m + \frac{h^2}{12}\frac{d^4 w_m}{dx^4} - \frac{\rho\omega^2(1-\nu^2)}{E}w_m = 0 \tag{5.14}$$

$$\frac{1}{R^2}w_m + \frac{h^2}{12}\frac{d^4 w_m}{dx^4} - \frac{\rho\omega^2}{E}w_m = 0 \tag{5.15}$$

$$k_x^4 = \frac{12}{h^2}\left(\frac{\rho\omega^2}{E} - \frac{1}{R^2}\right) \tag{5.16}$$

$$1 + t^2 k^4 - \Omega^2 = 0 \tag{5.17}$$

$$k = \pm\frac{(\Omega^2-1)^{1/4}}{\sqrt{t}}; \qquad \pm i\frac{(\Omega^2-1)^{1/4}}{\sqrt{t}} \tag{5.18}$$

It is seen how there exist 4 waves at all frequencies, and how for low frequencies these will be complex attenuating waves two of which go in either $\pm x$-direction. At the cut-on frequency of $\Omega = 1$ ($\omega^2 = \frac{E}{\rho R^2}$) the 4 complex attenuating waves become 2 evanescent waves and 2 propagating waves; one of each again going in either direction. The group and phase speeds are determined from the real positive root and are presented as (5.19) and (5.20). It can easily be verified that for $t \to 0$, the phase and group speeds go to zero.

$$c_p = \frac{\Omega}{k} = \frac{\Omega\sqrt{t}}{(\Omega^2-1)^{1/4}} \tag{5.19}$$

$$c_g = \frac{\partial\Omega}{\partial k} = \frac{2\sqrt{t}\left(\Omega^2-1\right)^{3/4}}{\Omega} \tag{5.20}$$

Now, to see if the acoustic black hole effect is present, t is expressed through the termination profile $h(x) = \epsilon x^n$ by $t^2 = \frac{h(x)^2}{12R^2}$ in (5.17). From here, the wavenumber expression is integrated with respect to x, and the nature of the integral is evaluated for different powers of n. Fortunately, this integral can be found analytically and is presented as (5.23). In the expression it is seen, how the integral diverges for $n \geq 2$, if the integral is extended to $x = 0$ just as for the flat plate in (5.7) on page 34. Any truncation of the termination profile by a residual height at the tip will cause the integral to converge, causing the acoustic black hole effect to be reduced. It has thereby been shown, starting from the differential equation of motion, how the acoustic black hole can be obtained for the breathing mode of a Poisson-less curved plate, with a power-law termination profile of power $n \geq 2$.

$$k = \frac{(\Omega^2-1)^{1/4}}{\sqrt{t}}; \qquad t(x) = \sqrt{\frac{h(x)^2}{12R_0^2}}; \qquad h(x) = \epsilon x^n \tag{5.21}$$

$$k(x) = \left(\frac{(\Omega^2-1)}{\frac{\epsilon^2 x^{2n}}{12R_0^2}}\right)^{1/4} = \left(\frac{12R_0^2(\Omega^2-1)}{\epsilon^2}\right)^{1/4} x^{-n/2} \tag{5.22}$$

$$\int k dx = \left(\frac{12R_0^2(\Omega^2-1)}{\epsilon^2}\right)^{1/4}\frac{1}{1-\frac{n}{2}}x^{1-\frac{n}{2}} \tag{5.23}$$

Having shown that the acoustic black hole effect can be obtained for $m = 0$ of a curved plate if one introduces certain model assumptions, the same will be attempted for $m > 0$. The differential equation of motion for the cylindrical shell governing the flexural motion is repeated as (5.24).

The equation contains the Poisson term, coupling the equation with the u-displacements as previously, as well as a number of bending terms all containing the $\frac{h^2}{12}$-factor. Additionally, it is seen how two red terms are present in the equation associated with the membrane forces in the shell, which do not contain the factor $h(x)$. This indicates, that the primary difference between the curved plate and the flat plate for $m > 0$, is the presence of Poisson-coupling terms, and terms associated with membrane forces, which do not contain the $h(x)$-factor.

From this observation, an idea is formulated, where if it is possible to remove these membrane-force terms from the equations, it would leave an equation only containing bending terms (still assuming a Poisson-less material). If only bending terms are present in the equation, it is expected that for a termination profile where $h \to 0$, the acoustic black hole effect will appear, just as it was observed for the flat plate. The membrane-force terms will be removed by the introduction of a kinematic constraint on the circumferential strain, ϵ_2, setting it to zero. The circumferential strain is expressed through equation (5.25), and it is seen how setting this to zero will cause the two red membrane force terms to cancel out[†].

$$\begin{aligned}&\frac{\nu}{R}\frac{du_m}{dx} + \frac{m}{R^2}v_m + \frac{h^2}{12}\frac{m^3}{R^4}v_m - \frac{h^2}{12}\frac{(2-\nu)m}{R^2}\frac{d^2v_m}{dx^2} + \frac{1}{R^2}w_m \\ &+ \frac{h^2}{12}\frac{d^4w_m}{dx^4} - \frac{h^2}{12}\frac{2m^2}{R^2}\frac{d^2w_m}{dx^2} + \frac{h^2}{12}\frac{m^4}{R^4}w_m - \frac{\rho\omega^2(1-\nu^2)}{E}w_m = 0\end{aligned} \tag{5.24}$$

$$\epsilon_2 = \frac{1}{R}\frac{\partial v}{\partial \theta} + \frac{w}{R} = 0 \tag{5.25}$$

To investigate if these material and kinematic constraints will result in the acoustic black hole effect, the equations of motion will be derived and analyzed. The equations of motion for this system will be derived through Hamilton's principle. This will be done by setting ν to zero, and introducing the kinematic constraint in the expressions for kinetic and potential energy before employing Hamilton's principle. Expressions for the kinetic energy, T_{SH}, elastic potential energy, U_{SH}, and the external potential, $W_{SH} = -V_{SH}$ are presented in (5.27), (5.28) and (5.29) respectively. Here, dots represent a time derivative. The external potential is presented for completeness, but as the subsequent analysis will be of free vibration of the shell, the external forcing terms can be disregarded already at this stage. The Lagrangian is then formulated as $L_{SH} = T_{SH} - U_{SH}$, and Hamilton's principle tells us that the motion of a system is given as the path which minimizes the time integral of L_{SH}. This is conveniently stated through setting the variation of the integral to zero (5.26).

$$\delta \int_{t_1}^{t_2} L dt = 0 \tag{5.26}$$

$$T_{SH} = \frac{1}{2}\rho h \int_0^L \int_0^{2\pi} \left[\dot{u}^2 + \dot{v}^2 + \dot{w}^2\right] R d\theta dx \tag{5.27}$$

$$U_{SH} = \frac{1}{2}\int_0^L \int_0^{2\pi} \left[\epsilon_1 T_1 + \epsilon_2 T_2 + \bar{\omega} S + \kappa_1 M_1 + \kappa_2 M_2 + \tau H\right] R d\theta dx \tag{5.28}$$

$$V_{SH} = -\int_0^L \int_0^{2\pi} \left[q_1 u + q_2 v + q_3 w\right] R d\theta dx \tag{5.29}$$

The mid-plane deformations are given as (5.30).

[†]It will become more obvious why the derivative of v spawns the m-factor, when a solution ansatz is introduced later.

$$\epsilon_1 = \frac{\partial u}{\partial x}, \qquad \text{Axial strain} \tag{5.30a}$$
$$\epsilon_2 = \frac{1}{R}\frac{\partial v}{\partial \theta} + \frac{w}{R}, \qquad \text{Circumferential strain} \tag{5.30b}$$
$$\bar{\omega} = \frac{1}{R}\frac{\partial u}{\partial \theta} + \frac{\partial v}{\partial x}, \qquad \text{Shear strain} \tag{5.30c}$$
$$\kappa_1 = -\frac{\partial^2 w}{\partial x^2}, \qquad \text{Bending curvature in axial direction} \tag{5.30d}$$
$$\kappa_2 = -\frac{1}{R^2}\frac{\partial^2 w}{\partial \theta^2} + \frac{1}{R^2}\frac{\partial v}{\partial \theta}, \qquad \text{Bending curvature in circumferential direction} \tag{5.30e}$$
$$\tau = -\frac{1}{R}\frac{\partial^2 w}{\partial x \partial \theta} + \frac{1}{R}\frac{\partial v}{\partial x}, \qquad \text{Twisting deformation} \tag{5.30f}$$

Similarly, the force and moment resultant in the shell are given as (5.31), where $\nu = 0$ has already been assumed for simplicity.

$$T_1 = Eh\frac{\partial u}{\partial x}, \qquad \text{Axial membrane force} \tag{5.31a}$$
$$T_2 = \frac{Eh}{R}\left(\frac{\partial v}{\partial \theta} + w\right), \qquad \text{Circumferential membrane force} \tag{5.31b}$$
$$S = \frac{Eh}{2}\left(\frac{\partial v}{\partial x} + \frac{1}{R}\frac{\partial u}{\partial \theta}\right), \qquad \text{Shear force} \tag{5.31c}$$
$$M_1 = \frac{-Eh^3}{12}\frac{\partial^2 w}{\partial x^2}, \qquad \text{Bending moment in axial direction} \tag{5.31d}$$
$$M_2 = \frac{-Eh^3}{12}\left(\frac{1}{R^2}\frac{\partial^2 w}{\partial \theta^2} - \frac{v}{R}\right), \qquad \text{Bending moment in circumferential direction} \tag{5.31e}$$
$$H = \frac{-Eh^3}{12}\left(\frac{1}{R}\frac{\partial^2 w}{\partial x \partial \theta} - \frac{1}{R}\frac{\partial v}{\partial x}\right), \qquad \text{Twisting moment} \tag{5.31f}$$

The next step is to perform variations on the kinetic energy expression, T_{SH}, but before doing so, the kinematic assumption of $\epsilon_2 = 0$ is introduced. Setting $\epsilon_2 = 0$ it is seen how $\frac{\partial v}{\partial \theta} = -w$. As separation of variables is possible for $(u(x,\theta,t), v(x,\theta,t), w(x,\theta,t))$, the same relation is seen to hold for the time derivatives: $\frac{\partial^2 v}{\partial \theta \partial t} = -\frac{\partial w}{\partial t}$. Insertion into (5.27), one obtains (5.32) where subscripts are used to denote spacial derivatives for compact notation.

$$T_{SH} = \frac{1}{2}\rho h \int_0^L \int_0^{2\pi} \left[\dot{u}^2 + \dot{v}^2 + \dot{v}_\theta^2\right] R d\theta dx \tag{5.32}$$

The next step is then to take variations on the displacements and perform integration by parts to "offload" the derivatives from the variational terms. The variations are performed in (5.33), where an arbitrary integral is performed from t_1 to t_2 c.f. the Hamiltonian principle (5.26).

$$\delta \int_{t_1}^{t_2} T_{SH} dt = \delta \int_{t_1}^{t_2} \left(\frac{1}{2}\rho h \int_0^L \int_0^{2\pi} \left[\dot{u}^2 + \dot{v}^2 + \dot{v}_\theta^2\right] R d\theta dx\right) dt \tag{5.33}$$

Based on the commutative properties of the δ-operator, variations are performed under the integral, to obtain (5.34). For the first 2 terms in the integrand, integration by parts in time is performed. This will allow the time-derivative operator to be "moved" from the variational term, leaving a pure variational term which vanishes at the boundaries t_1 and t_2 c.f. the fundamental Lemma of Calculus of Variations [29].

$$\delta \int_{t_1}^{t_2} T_{SH} dt = \int_{t_1}^{t_2} \left(\rho h \int_0^L \int_0^{2\pi} \left[\dot{u}\delta\dot{u} + \dot{v}\delta\dot{v} + \dot{v}_\theta \delta \dot{v}_\theta\right] R d\theta dx\right) dt \tag{5.34}$$

$$\delta \int_{t_1}^{t_2} T_{SH} dt = \left(\rho h \int_0^L \int_0^{2\pi} \left[\cancelto{0}{\dot{u}\delta u \Big|_{t=t_1}^{t=t_2}} - \int_{t_1}^{t_2} \ddot{u}\delta u dt + \cancelto{0}{\dot{v}\delta v \Big|_{t=t_1}^{t=t_2}} - \int_{t_1}^{t_2} \ddot{v}\delta v dt + \int_{t_1}^{t_2} \dot{v}_\theta \delta \dot{v}_\theta dt \right] R d\theta dx \right) \tag{5.35}$$

For the third term in the integrand, integration by parts is first performed for θ, resulting in a term to be evaluated at $\theta = 0$ and $\theta = 2\pi$. As these boundaries correspond to the same physical position on the shell, the term implicitly cancels to zero. Finally, integration by parts is performed in time for the third term, and the final expression is obtained as (5.36).

$$\delta \int_{t_1}^{t_2} T_{SH} dt = \int_{t_1}^{t_2} \left(\rho h \int_0^L \int_0^{2\pi} \left[-\ddot{u}\delta u - (\ddot{v} - \ddot{v}_{\theta\theta})\delta v \right] R d\theta dx \right) dt \tag{5.36}$$

Next, variations are performed on the potential energy expression, U_{SH}. First, the expressions for the mid-plane deformations and force/moment resultants are substituted into (5.28). The equation is expanded, and a sizable expression is obtained as (5.37), where subscripts are used to denote partial spatial derivatives. Each square bracket holds a single term from the original expression for U_{SH}, in an attempt to make the derivation easier to follow.

$$\begin{aligned} U_{SH} = \frac{1}{2} \int_0^L \int_0^{2\pi} & \left[Ehu_x^2 \right] + \left[\epsilon_2 T_2 \right] + \left[\frac{Eh}{2} \left(\frac{u_\theta}{R^2} + v_x^2 + \frac{2u_\theta v_x}{R} \right) \right] + \left[\frac{Eh^3}{12} w_{xx}^2 \right] \\ & + \left[\frac{Eh^3}{12R^3} \left(\frac{1}{R} w_{\theta\theta}^2 - w_{\theta\theta} v - \frac{1}{R} v_\theta w_{\theta\theta} + v_\theta v \right) \right] + \left[\frac{Eh^3}{12R^2} \left(w_{x\theta}^2 + v_x^2 - 2w_{x\theta} v_x \right) \right] R d\theta dx \end{aligned} \tag{5.37}$$

Introducing the kinematic assumption of $\epsilon_2 = 0$ to (5.37), a new expression is obtained only in terms of u and v as (5.38).

$$\begin{aligned} U_{SH} = \frac{1}{2} \int_0^L \int_0^{2\pi} & \left[Ehu_x^2 \right] + \left[\frac{Eh}{2} \left(\frac{u_\theta}{R^2} + v_x^2 + \frac{2u_\theta v_x}{R} \right) \right] + \left[\frac{Eh^3}{12} v_{\theta xx}^2 \right] \\ & + \left[\frac{Eh^3}{12R^3} \left(\frac{1}{R} v_{\theta\theta\theta}^2 + v_{\theta\theta\theta} v + \frac{1}{R} v_\theta v_{\theta\theta\theta} + v_\theta v \right) \right] + \left[\frac{Eh^3}{12R^2} \left(v_{x\theta\theta}^2 + v_x^2 + 2v_{x\theta\theta} v_x \right) \right] R d\theta dx \end{aligned} \tag{5.38}$$

Sparing many of the details of the derivation, variations are performed on u and v in (5.38). Next, each term is tediously integrated by parts, to offload derivatives from the variational terms. Again, several boundary terms are generated, some of which are to be evaluated at $\theta = 0$ & 2π and some to be evaluated at $x = 0$ & L. Again, the boundary terms evaluated at θ implicitly cancel to zero. The terms evaluated at L are disregarded, as the subsequent analysis will consider infinite waveguides. The final expression is presented in (5.39), where all terms are conveniently grouped based on their variation terms.

$$\begin{aligned} \delta \int_{t_1}^{t_2} U_{SH} dt = \int_{t_1}^{t_2} \int_0^L \int_0^{2\pi} & \left(\left[-Ehu_{xx} - \frac{Eh}{2R^2} u_{\theta\theta} - \frac{Eh}{2R} v_{x\theta} \right] \delta u + \left[\frac{-Eh}{2} v_{xx} - \frac{Eh}{2R} u_{x\theta} - \frac{Eh^3}{12} v_{\theta 2x4} \right. \right. \\ & \left. \left. - \frac{Eh^3}{12R^4} v_{\theta 6} - \frac{Eh^3}{12R^4} v_{\theta 4} - \frac{Eh^3}{12R^2} v_{\theta 4x2} - \frac{Eh^3}{12R^2} v_{xx} - \frac{Eh^3}{12R^2} 2v_{2\theta 2x} \right] \delta v \right) R d\theta dx dt \end{aligned} \tag{5.39}$$

Collecting the terms with the δu and δv factors from (5.36) and (5.39) two differential equations can be established. These are written out as (5.40) and (5.41).

$$\frac{\partial^2 u}{\partial x^2} + \frac{1}{2R^2} \frac{\partial^2 u}{\partial \theta^2} + \frac{1}{2R} \frac{\partial^2 v}{\partial x \partial \theta} - \frac{\rho}{E} \frac{\partial^2 u}{\partial t^2} = 0 \tag{5.40}$$

$$\frac{1}{2}\frac{\partial^2 v}{\partial x^2}+\frac{1}{2R}\frac{\partial^2 u}{\partial x\partial\theta}+\frac{h^2}{12}\left[\frac{\partial^6 v}{\partial x^4\partial\theta^2}+\frac{1}{R^4}\frac{\partial^6 v}{\partial\theta^6}+\frac{1}{R^4}\frac{\partial^4 v}{\partial\theta^4}+\frac{1}{R^2}\frac{\partial^6 v}{\partial x^2\partial\theta^4}+\frac{1}{R^2}\frac{\partial^2 v}{\partial x^2}+\frac{2}{R^2}\frac{\partial^4 v}{\partial x^2\partial\theta^2}\right] \\ -\frac{\rho}{E}\left(\frac{\partial^2 v}{\partial t^2}-\frac{\partial^4 v}{\partial t^2\partial\theta^2}\right)=0 \tag{5.41}$$

At this point, the differential equations of motion for a cylindrical shell have been derived under the assumption of no circumferential extensibility, and no Poisson effects. Unsurprisingly, two equations are derived instead of three, as w-displacements were condensed from the system early in the derivation. The w-displacements can however be recovered trivially from the relation $w=-v_\theta m$. Additionally, the equations are still coupled as both equations contain the yet unknown u- an v-displacements. The next step in the analysis is to impose ansatz for u- and v-displacements which will be done in the form (5.42) and (5.43).

$$u(x,\theta,t)=\sum_m \quad u_m(x) \quad cos(m\theta)\, exp(-i\omega t) \tag{5.42}$$

$$v(x,\theta,t)=\sum_m \underbrace{v_m(x)}_{x-dependency}\underbrace{sin(m\theta)}_{\theta-wave}\underbrace{exp(-i\omega t)}_{Time} \tag{5.43}$$

It is observed, how after inserting these Ansatz and differentiating w.r.t. θ, each term in (5.40) contains the cosine-factor while each term in (5.41) contains the sine-factor, and so these trigonometric terms are condensed from the equations. From these operations (5.44) and (5.45) are obtained.

$$\frac{\partial^2 u_m}{\partial x^2}-\frac{m^2}{2R^2}u_m+\frac{m}{2R}\frac{\partial v_m}{\partial x}+\frac{\rho\omega^2}{E}u_m=0 \tag{5.44}$$

$$\frac{1}{2}\frac{\partial^2 v_m}{\partial x^2}-\frac{m}{2R}\frac{\partial u_m}{\partial x}+\frac{h^2}{12}\left[-m^2\frac{\partial^4 v_m}{\partial x^4}-\frac{m^6}{R^4}v_m+\frac{m^4}{R^4}v_m+\frac{m^4}{R^2}\frac{\partial^2 v_m}{\partial x^2}+\frac{1}{R^2}\frac{\partial^2 v_m}{\partial x^2}-\frac{2m^2}{R^2}\frac{\partial^2 v_m}{\partial x^2}\right] \\ +\frac{\rho\omega^2}{E}\left(1+m^2\right)v_m=0 \tag{5.45}$$

Next, Ansatz are employed for the x-dependencies $u_m(x)$ and $v_m(x)$. This will be done in the same manner as in the beginning of Chapter 4 using $A_j exp(ik_x x)$ where k_x is the dimensional wavenumber with units $[m^{-1}]$. Inserting this into the equations yields (5.46) and (5.47). The original differential equations of motion for a cylindrical shell with $\nu\neq 0$ and $\epsilon_2\neq 0$ are also presented in red below the equations so that a direct comparison can be made.

$$k_x^2 A_1+\frac{m^2}{2R^2}A_1-ik_x\frac{m}{2R}A_2-\frac{\rho\omega^2}{E}A_1=0 \tag{5.46}$$

$$k_x^2 A_1+\frac{1-\nu}{2}\frac{m^2}{R^2}A_1-\frac{1+\nu}{2}\frac{m}{R}A_2 ik_x-\frac{\nu}{R}A_3 ik_x-\frac{\rho\omega^2(1-\nu^2)}{E}A_1 \;=0$$

For (5.46), it is seen how the only difference between the black and red equation stems from assuming $\nu=0$. This gives some confidence in the validity of the obtained solution.

$$\frac{k_x^2}{2}A_2+ik_x\frac{m}{2R}A_1+\frac{h^2}{12}\left[m^2k_x^4+\frac{m^6}{R^4}-\frac{m^4}{R^4}+k_x^2\frac{m^4}{R^2}+k_x^2\frac{1}{R^2}-k_x^2\frac{2m^2}{R^2}\right]A_2 \\ -\frac{\rho\omega^2}{E}\left(1+m^2\right)A_2=0 \tag{5.47}$$

$$\frac{1+\nu}{2}\frac{m}{R}A_1 ik_x + \frac{1-\nu}{2}A_2k_x^2 + \frac{m^2}{R^2}A_2 + \frac{h^2}{12}\frac{2(1-\nu)}{R^2}A_2k_x^2 + \frac{h^2}{12}\frac{m^2}{R^4}A_2$$
$$+\frac{m}{R^2}A_3 + \frac{h^2}{12}\frac{m^3}{R^4}A_3 + \frac{h^2}{12}\frac{(2-\nu)m}{R^2}A_3k_x^2 - \frac{\rho\omega^2(1-\nu^2)}{E}A_2 = 0$$

$$\frac{\nu}{R}A_1 ik_x + \frac{m}{R^2}A_2 + \frac{h^2}{12}\frac{m^3}{R^4}A_2 + \frac{h^2}{12}\frac{(2-\nu)m}{R^2}A_2k_x^2 + \frac{1}{R^2}A_3 + \frac{h^2}{12}A_3k_x^4$$
$$+\frac{h^2}{12}\frac{2m^2}{R^2}A_3k_x^2 + \frac{h^2}{12}\frac{m^4}{R^4}A_3 - \frac{\rho\omega^2(1-\nu^2)}{E}A_3 = 0$$

Comparing (5.47) with the two red equations below it, it is not immediately obvious how the equations relate. It is however seen, that (5.47) could not have been obtained simply by introducing the kinematic constraint to the red equations. It is seen how the kinematic constraint successfully removed the terms related to membrane forces, leaving only two terms that are not multiplied by the factor $\frac{h^2}{12}$. The first of these terms $\left(\frac{k_x^2}{2}A_2\right)$ originate from the first of the red equations, governing the circumferential motion of the cylindrical shell. The second "non-bending" term, $\left(\frac{ik_xm}{2R}A_1\right)$, is a coupling term with the u-displacements, which also appears in (5.46).

The equations are recast in matrix form using the unit-less parameters from (5.49). It is seen how the system is a 2-by-2 system, as the radial displacements have been described through the circumferential displacements. Finally, the dispersion equation is presented in vector form as (5.50). It is seen how the dispersion equation for the case of $\nu, \epsilon_2 = 0$ is a 6^{th}-order polynomial in k. This means, that for any frequency, 6 waves are present as opposed to the 8 waves present in the original cylindrical shell model. This is a result of the flexural and circumferential motions no longer being independent of each other due to the kinematic constraint of $\epsilon_2 = 0$.

$$L_{jl}A_j = 0; j,l = 1,2 \tag{5.48}$$

$$L_{11} = k^2 + \frac{1}{2}m^2 - \Omega^2$$
$$L_{22} = \frac{1}{2}k^2 + t^2\left[m^6 - m^4 + m^4k^2 + m^2k^4 - 2m^2k^2 + k^2\right] - \Omega^2(1+m^2)$$
$$L_{12} = -L_{21} = -\frac{1}{2}mik$$

Using the unit-less conversion of:

$$k = k_xR \qquad t^2 = \frac{h^2}{12R^2} \qquad \Omega^2 = \frac{\omega^2R^2}{c_L^2} = \frac{\rho\omega^2R^2}{E} \tag{5.49}$$

$$\begin{Bmatrix} k^6 & k^4 & k^2 & k \end{Bmatrix} \begin{Bmatrix} m^2t^2 \\ \frac{3m^4t^2}{2} - \Omega^2m^2t^2 - 2m^2t^2 + t^2 + \frac{1}{2} \\ 2\Omega^2m^2t^2 - \Omega^2m^4t^2 - \Omega^2m^2 - \Omega^2t^2 - \frac{3\Omega^2}{2} + \frac{3m^6t^2}{2} - 2m^4t^2 + \frac{m^2t^2}{2} \\ \Omega^4m^2 + \Omega^4 - \Omega^2m^6t^2 + \Omega^2m^4t^2 - \frac{\Omega^2m^4}{2} - \frac{\Omega^2m^2}{2} + \frac{m^8t^2}{2} - \frac{m^6t^2}{2} \end{Bmatrix} = 0 \tag{5.50}$$

Numerical solutions are found for $m = 0, 1, 2$, which are presented in Figures 5.4, 5.5 and 5.6 respectively. The numerical solutions assume $\alpha = \frac{h}{R} = \frac{1}{40}$.

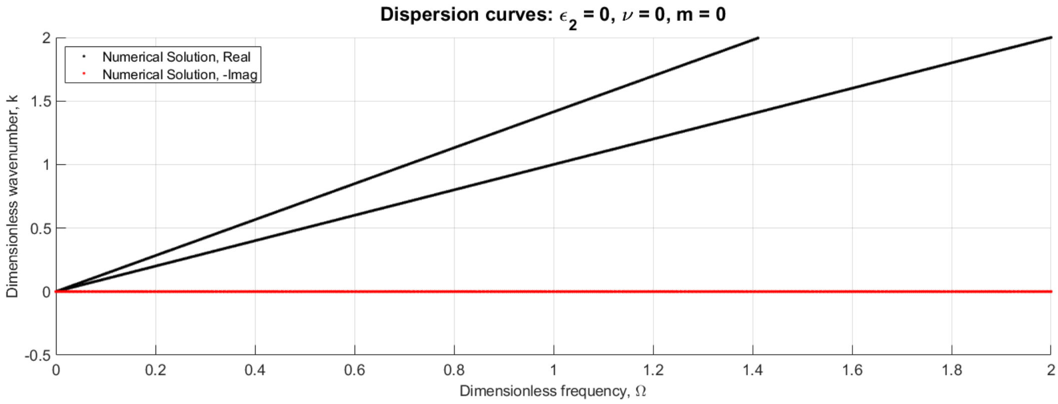

Figure 5.4: Numerical solution for the dispersion curves of cylindrical shell model with $\epsilon_2, \nu = 0$ ($m = 0$).

For the case of $m = 0$, the system reduces to a 4^{th}-order polynomial in k, see (5.50), and so only 4 waves exist; two of which going in either x-direction. This follows intuition, as the system has $\epsilon_2 = 0$, meaning no circumferential strain may exist in the shell. For the case of $m = 0$, the shell must deform axis-symmetrically, inevitably causing membrane- forces and strains. Such an axis-symmetric flexural wave therefore can not exist in the shell when $\epsilon_2 = 0$, and the only waves present will be two torsion waves and two longitudinal waves. This is also seen in the figure, where 2 purely real dispersion branches are present, both of which originating from zero with no dispersion properties.

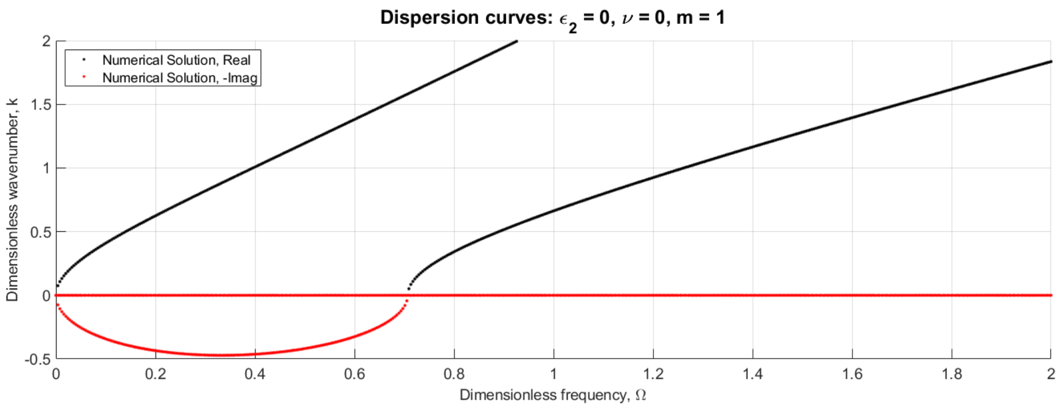

Figure 5.5: Numerical solution for the dispersion curves of cylindrical shell model with $\epsilon_2, \nu = 0$ ($m = 1$).

For the case of $m = 1$, the dispersion equation is a 6^{th}-order polynomial in k, and so 6 waves exist. Looking at Figure 5.5 however, only 2 branches seem to be present, this is because a third purely imaginary branch (evanescent near-field wave) is located at $\approx 100i$ and it would be impractical to include all 3 branches in the same figure. The third branch never cuts on and remains strongly evanescent for all frequencies. This is also confirmed, by solving for cut-on frequencies by setting $k = 0$ and solving the dispersion equation for roots of Ω. Here it is found, that the cut-on frequencies are defined by (5.51) and (5.52).

$$\Omega_{C1} = \frac{\sqrt{2}m}{2} \tag{5.51}$$

$$\Omega_{C2} = \frac{m^2\, t\, \sqrt{m^4 - 1}}{m^2 + 1} \tag{5.52}$$

The dispersion branches seen in the figure, are very reminiscent of the dispersion branches of the original shell model with $m = 1$, (see Figure 4.8 on page 17), if one disregards the third missing branch.

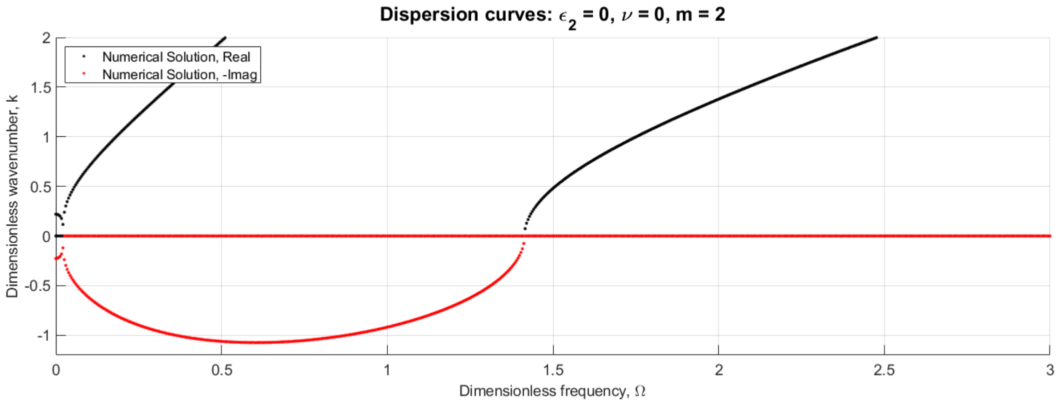

Figure 5.6: Numerical solution for the dispersion curves of cylindrical shell model with $\epsilon_2, \nu = 0$ ($m = 2$).

For the case of $m = 2$, six waves still exist, but the third branch is again not visible in the figure, as it is imaginary for all frequencies c.f. (5.51) and (5.52). For $m = 2$ no branches originate from zero, which was also the case for the original cylindrical shell model.

5.2 Investigating the acoustic black hole effect for $\epsilon_2, \nu = 0$

Now, asymptotic analysis can be performed for the dispersion branches of the newly obtained shell model. The analysis will be performed similarly to what was done in Chapter 4, using the naive asymptotic expansion around $\Omega = 0$. First, the bending mode, $m = 1$, is investigated, and afterward, the ovalling mode, $m = 2$, is investigated.

5.2.1 Investigating the bending mode, $m = 1$

An expansion series is assumed in the form (5.53), based on the previous experience from Chapter 4. For the first branch, the cut-on frequency Ω_c is set to zero, while for the second branch, the cut-on frequency is set to $\frac{\sqrt{2}}{2}$ c.f. (5.51,5.52) on page 43. Substituting (5.53) into the dispersion equation (5.50), and balancing terms at the $\mathcal{O}(\Omega^2)$ order gives the first constants, x_0, for the first and second branch respectively. Similarly, balancing terms at the $\mathcal{O}(\Omega^3)$ order gives the second constants, x_1. The constants for the first branch are found in (5.54) and (5.55), and the constants for the second branch are found in (5.56) and (5.57). The asymptotic approximation can be found overlaid with the numerical solution in Figure 5.7. Here it can be seen how the asymptotic approximation for the first branch gives good results up to around $\Omega = 0.3$, while for the second branch, the approximation gives good results up to around $\Omega = 0.9$.

$$\bar{k}(\Omega) = x_0(\Omega - \Omega_C)^{1/2} + x_1(\Omega - \Omega_C)^{3/2} \tag{5.53}$$

Constants x_0 and x_1 for first branch:

$$x_0 = \left(\frac{2}{t^2+1}\right)^{1/4} \tag{5.54}$$

$$x_1 = -\frac{\frac{4\,t^2}{t^2+1} - 5}{4\left(\frac{2}{t^2+1}\right)^{1/4} + 4\,t^2\left(\frac{2}{t^2+1}\right)^{1/4}} \tag{5.55}$$

Constants x_0 and x_1 for second branch:

$$x_0 = \frac{2\sqrt{5}\sqrt{2\,\Omega_C - 1}\sqrt{2\,\Omega_C + 1}}{5\sqrt{\Omega_C}} = 1.0637 \tag{5.56}$$

$$x_1 = \frac{24\,{\Omega_C}^2 - 10\,\Omega_C\,{x_0}^2 + {x_0}^4 - 2}{10\,{\Omega_C}^2\,x_0} = 0.6167 \tag{5.57}$$

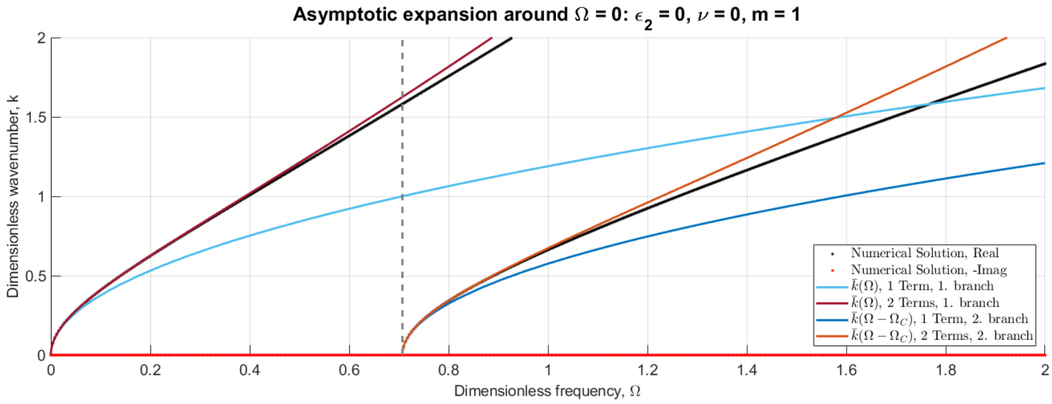

Figure 5.7: Asymptotic approximations overlaid with the numerical solution for cylindrical shell model where $\epsilon_2, \nu = 0$ ($m = 1$).

As can be seen from the constants for the first branch, the wave numbers are dependent on the thickness parameter, t. As the assumed expansion series is identical to the one used for the bending mode in Chapter 4, the phase and group speed expressions are also identical. The phase and group speed is given by (4.43) and (4.44) on page 24, but are repeated here for convenience as (5.58) and (5.59). It is immediately obvious, that the phase and group speeds for the first branch do not go to zero for the limiting case of $t \to 0$. Numerical calculations of the reflection coefficient and NWV showed no acoustic black hole effect, and the results are not presented for this reason. For the second branch, it is seen how x_0 and x_1 are constant. The phase and group speeds are therefore unaffected by a change in shell thickness, and the acoustic black hole effect is therefore not obtainable from the asymptotic approximation.

$$c_p = \frac{\Omega}{\bar{k}} = \frac{\Omega}{x_0(\Omega - \Omega_C)^{1/2} + x_1(\Omega - \Omega_C)^{3/2}} \tag{5.58}$$

$$c_g = \frac{\partial \Omega}{\partial \bar{k}} = \frac{2(\Omega - \Omega_C)^{1/2}}{x_0 + 3x_1(\Omega - \Omega_C)} \tag{5.59}$$

High-frequency solution: $\epsilon_2, \nu = 0$, $m = 1$:
The observation, that the first two terms in the asymptotic approximation for the second branch are independent of t hints towards the low-frequency range being dominated by longitudinal motion. This can be investigated further, by introducing the modal coefficient, $\xi = \frac{A_1}{A_2}$ in (5.48) on page 42. Doing so makes it possible to determine the ratio between the longitudinal and circumferential motion of the given wave, by evaluating (5.60) for given values of k and Ω on a given dispersion curve. In Figure 5.8, the modal coefficients have been plotted together with the two dispersion branches in a log plot. Values of ξ above unity indicate a wave dominated by longitudinal u-motion, while values below unity indicate a wave dominated by circumferential v-motion (and thereby flexural w-motion due to the kinematic constraint of $\epsilon_2 = 0$). For the first branch, it is seen how in the low-frequency range the wave is a mixture between u- and v-motion, but with increasing frequency, the v-motion becomes dominant. Right at the cut-on of the second branch, the wave is strongly dominated by u-motion, and remains this way with increasing frequency.

$$L_{11}A_1 + L_{12}A_2 = 0 \leftrightarrow \xi = \frac{-L_{12}}{L_{11}} \tag{5.60}$$

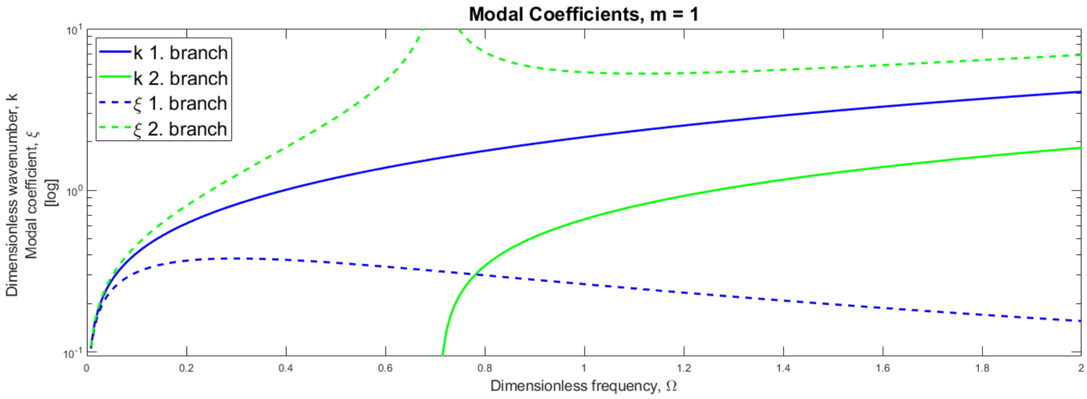

Figure 5.8: Modal coefficients, ξ, overlaid with wave numbers in log-plot to show which motion type is dominant at various frequencies for the two dispersion branches ($m = 1$).

As the acoustic black hole effect is expected to be obtainable for waves dominated by flexural motion, it seems unlikely to obtain the effect from the second branch. The first branch, however, seems to have some potential in the high-frequency range which has not been investigated as asymptotic expansion has always been carried out around $\Omega = 0$. In order to investigate the high-frequency range, a frequency scaling approach is used together with the dominant balance method, inspired by [30]. Based on the square root proportionality of $k \propto \sqrt{\Omega}$, re-scaled frequency and wave numbers are introduced as (5.61), and substituted into the dispersion equation to obtain (5.62). Here $\eta \ll 1$ acts as the re-scaling parameter. A short note on the scaling approach is presented in Appendix E, where the method is exemplified.

$$k_{rs} = k\sqrt{\eta}; \qquad \Omega_{rs} = \Omega\eta \tag{5.61}$$

$$\frac{2\,{\Omega_{rs}}^4}{\eta^4} - \frac{{\Omega_{rs}}^2}{\eta^2} + \frac{{k_{rs}}^4}{2\,\eta^2} - \frac{5\,{\Omega_{rs}}^2\,{k_{rs}}^2}{2\,\eta^3} + \frac{{k_{rs}}^4\,t^2}{2\,\eta^2} + \frac{{k_{rs}}^6\,t^2}{\eta^3} - \frac{{\Omega_{rs}}^2\,{k_{rs}}^4\,t^2}{\eta^4} = 0 \tag{5.62}$$

From here, the re-scaled wavenumber, k_{rs}, is expressed through an expansion series, very similar to what was done for the naive asymptotic approximations for the low-frequency analysis. The expansion for k_{rs} will be attempted in the form (5.63), where x_0 and x_1 are constants to be determined, while p_0 and p_1 are the yet undetermined powers of η.

$$\bar{k_{rs}} = x_0\eta^{p_0} + x_1\eta^{p_1}... \tag{5.63}$$

The task is now, to substitute (5.63) into (5.62), and attempt to balance the higher order terms of the obtained expression, by varying the powers p_0 and p_1. If appropriate powers of p_0 and p_1 are chosen, the higher order terms in the expression can be equated and solved for an expression for x_0 or x_1.

If one equates $p_0 = 0$, two terms dominate the solution as they contain the η^{-4} power. As $\eta \ll 1$, high negative powers of eta will make a term dominate the expression. The two terms are balanced in (5.64), and solved for the final expression of x_0 in (5.65). If one now returns to the non-scaled frequencies and wave numbers, the solution for x_0 can be plotted against the numerical solution to see if a valid solution has been obtained. This is done in Figure 5.9, where it is seen how the solution gives poor results in the low-frequency range, and only begins to give a good approximation in the *very* high-frequency range. For increasing frequencies $\Omega >> 100$, the approximation fits the numerical solution perfectly. The first term is not seen as sufficient, as the solution is only valid at these excessively high frequencies, and so two more terms are found.

$$\frac{2\Omega_{rs}^4}{\eta^4} - \frac{\Omega_{rs}^2 t^2 x_0^4}{\eta^4} = 0 \tag{5.64}$$

$$x_0 = \left(\frac{\sqrt{2}\Omega_{rs}}{t}\right)^{1/2} \tag{5.65}$$

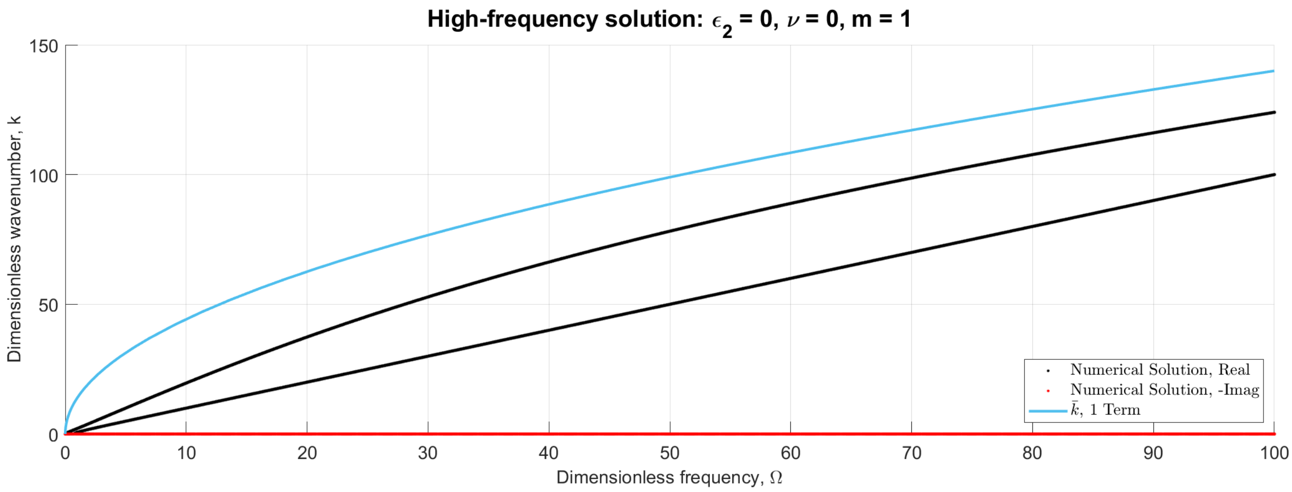

Figure 5.9: High-frequency asymptotic solution including one term for cylindrical shell model having $\epsilon_2, \nu = 0$ ($m = 1$).

The second term is found by setting $p_0 = 0$ and $p_1 = 1$, which caused three terms to dominate the expression as they contained the η^{-3} power†. These terms are balanced in (5.66), and solved for the final expression of x_1 in (5.67).

$$\frac{t^2 x_0^6}{\eta^3} - \frac{5\Omega_{rs}^2 x_0^2}{2\eta^3} - \frac{4\Omega_{rs}^2 t^2 x_0^3 x_1}{\eta^3} = 0 \tag{5.66}$$

$$x_1 = \frac{2t^2 x_0^4 - 5\Omega_{rs}^2}{8\Omega_{rs}^2 t^2 x_0} \tag{5.67}$$

Finally, the third term is found by setting $p_0 = 0$, $p_1 = 1$, and $p_2 = 2$. which caused seven terms to dominate the expression as they contained the η^{-2} power†. These terms are balanced in (5.68), and solved for the final expression of x_2 in (5.69). The obtained asymptotic solution for the high-frequency range is plotted against the numerical solution in Figure 5.10. From the figure it is seen how the addition of the second and third terms improves the solution significantly. The obtained solution is still only valid for the high-frequency range of $\Omega \gg\approx 50$, which is still far beyond the applicable range of the Goldenveizer-Novozhilov shell theory, and much higher frequency than most typical excitation frequencies of mechanical systems. For the geometry listed in Table 4.2 on page 21, $\Omega = 50$ is equivalent to $\omega \approx 41000\, rad/s$ or 6.5 kHz. In spite of this, the obtained solution will still be analyzed for the acoustic black hole effect.

$$\frac{{x_0}^4}{2\,\eta^2} - \frac{{\Omega_{kr}}^2}{\eta^2} + \frac{t^2\,{x_0}^4}{2\,\eta^2} + \frac{6\,t^2\,{x_0}^5\,x_1}{\eta^2} - \frac{5\,{\Omega_{kr}}^2\,x_0\,x_1}{\eta^2} - \frac{6\,{\Omega_{kr}}^2\,t^2\,{x_0}^2\,{x_1}^2}{\eta^2} - \frac{4\,{\Omega_{kr}}^2\,t^2\,{x_0}^3\,x_2}{\eta^2} = 0 \tag{5.68}$$

$$x_2 = \frac{-12\,{\Omega_{rs}}^2\,t^2\,{x_0}^2\,{x_1}^2 - 10\,{\Omega_{rs}}^2\,x_0\,x_1 - 2\,{\Omega_{rs}}^2 + 12\,t^2\,{x_0}^5\,x_1 + t^2\,{x_0}^4 + {x_0}^4}{8\,{\Omega_{rs}}^2\,t^2\,{x_0}^3} \tag{5.69}$$

†Disregarding the η^{-4}-power terms.
†Disregarding the η^{-4}-power and η^{-3}-power terms.

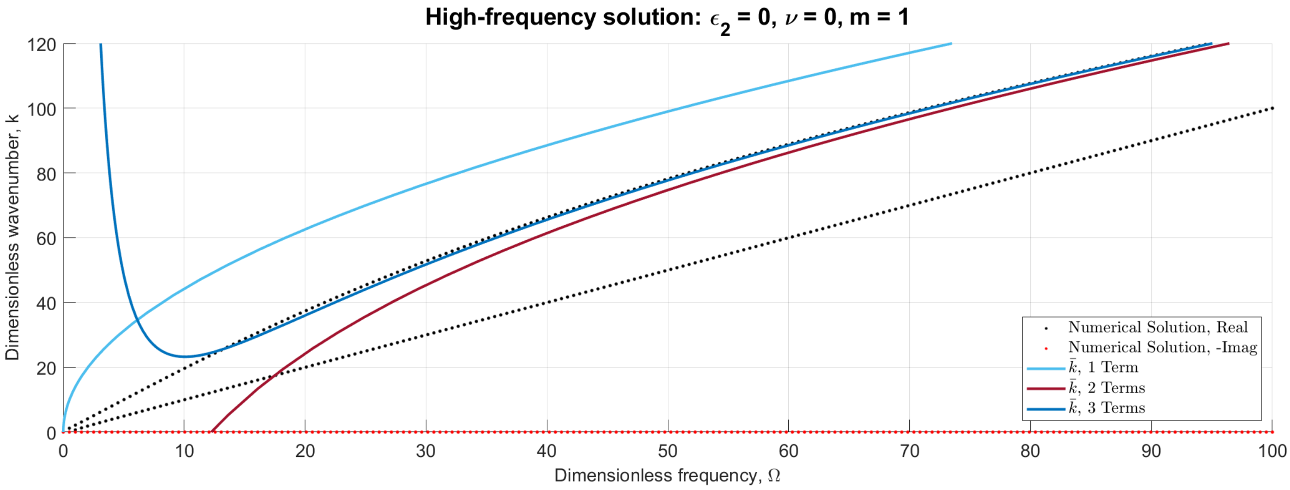

Figure 5.10: High-frequency asymptotic solution for cylindrical shell model having $\epsilon_2, \nu = 0$ $(m = 1)$.

After some algebraic simplification, the full solution of $\bar{k} = x_0 + x_1\eta + x_2\eta^2$ is written out as (5.70), using the non-scaled frequencies and wave numbers, Ω and k. The phase- and group speeds are presented as (5.71) and (5.72) respectively, where it can be seen how for $t \to 0$, both expressions tend to zero.

$$\bar{k} = \frac{2^{1/4}\left(2^8\,\Omega^2\,t^2 - 2^4\,\sqrt{2}\,\Omega\,t + 1\right)}{2^8\,t^4\left(\frac{\Omega}{t}\right)^{3/2}} \tag{5.70}$$

$$c_p = \frac{\Omega}{k} = \frac{2^7 2^{3/4} t^4 \Omega\left(\frac{\Omega}{t}\right)^{3/2}}{2^8 t^2 \Omega^2 - 2^4\sqrt{2} t\Omega + 1} \tag{5.71}$$

$$c_g = \frac{\partial\Omega}{\partial k} = \frac{2^9 t^5\left(\frac{\Omega}{t}\right)^{5/2}}{2^{1/4}2^8 t^2\Omega^2 + 2^{3/4}2^4 t\Omega 2^{1/4}3} \tag{5.72}$$

The acoustic black hole effect will now be investigated for a termination profile of $h \to 0$, using the power-law termination profile $h(x) = \epsilon x^n$. Substituting the expression for $h(x)$ into (5.70), the expression for the high-frequency wavenumber becomes (5.73). This expression is somewhat unwieldy and is split into 3 separate terms as (5.74), in an attempt to make the task of integrating the expression easier.

$$\bar{k} = \frac{2^{3/4}\,3^{1/4}\,R^2\left(3\,R^2 + 64\,\Omega^2\,\epsilon^2\,x^{2\,n} - 8\,\sqrt{6}\,\Omega\,R^2\,\sqrt{\frac{\epsilon^2\,x^{2\,n}}{R^2}}\right)}{64\,\epsilon^4\,x^{4\,n}\left(\frac{\Omega}{\sqrt{\frac{\epsilon^2\,x^{2\,n}}{R^2}}}\right)^{3/2}} \tag{5.73}$$

$$\bar{k} = 2^{1/4}\,\frac{9}{16}\,\frac{R^4}{\epsilon^4\,x^{4\,n}\left(\frac{\sqrt{12}\,\Omega}{\frac{\epsilon x^n}{R}}\right)^{3/2}} + 12\,2^{1/4}\,\frac{\Omega^2\,R^2}{\epsilon^2\,x^{2\,n}\left(\frac{\sqrt{12}\,\Omega}{\frac{\epsilon x^n}{R}}\right)^{3/2}} - \frac{3}{4}\sqrt{12}\,2^{3/4}\,\frac{\Omega\,R^4\,\frac{\epsilon x^n}{R}}{\epsilon^4\,x^{4\,n}\left(\frac{\sqrt{12}\,\Omega}{\frac{\epsilon x^n}{R}}\right)^{3/2}} \tag{5.74}$$

Now (5.74) is integrated with respect to x to obtain (5.75). It is seen how the first term diverges if $n = 2/5$, as the denominator will equal zero. The first term is also seen to diverge for $n \geq \frac{2}{5}$ as the numerator will tend to negative infinity if the integral is evaluated at $x = 0$, which is equivalent to a termination profile with no residual thickness at the tip. The same argumentation can be used to conclude that the second term will diverge at $n \geq \frac{2}{3}$ and that the third term will diverge at $n \geq 2$. This might indicate, that the acoustic black hole effect is obtainable from termination profiles having n-powers lower than unity, but this is not the case. A termination profile with $n < 1$, would severely violate the requirement of low NWV, as around $x = 0$ the rate of change of the shell thickness would grow unbounded, resulting in unbounded NWV. It also becomes obvious, that such a termination profile would violate the requirement of low NWV, when the profile is plotted, see Figure 5.11. The termination is reminiscent of a simple 90°cut, which would reflect all incoming wave energy. This means, that though the integral diverges for n-powers less than 2, the acoustic black hole effect is not obtainable unless a termination profile with $n \geq 2$ is used.

$$\int \bar{k} dx = 2^{1/4} \frac{9}{16} \left[-\frac{\sqrt{2}\, 3^{1/4}\, R^2\, x^{1-2\,n} \sqrt{\frac{\Omega\, R}{\epsilon\, x^n}}}{6\, \Omega^2\, \epsilon^2\, (5\, n - 2)} \right] + 12\, 2^{1/4} \left[-\frac{3^{1/4}\, x \sqrt{\frac{2\, \Omega\, R}{\epsilon\, x^n}}}{6\, n - 12} \right] - \frac{3}{4} \sqrt{12}\, 2^{3/4} \left[-\frac{\sqrt{2}\, 3^{1/4}\, R^2\, x^{1-n} \sqrt{\frac{\Omega\, R}{\epsilon\, x^n}}}{6\, \Omega\, \epsilon\, (3\, n - 2)} \right] \tag{5.75}$$

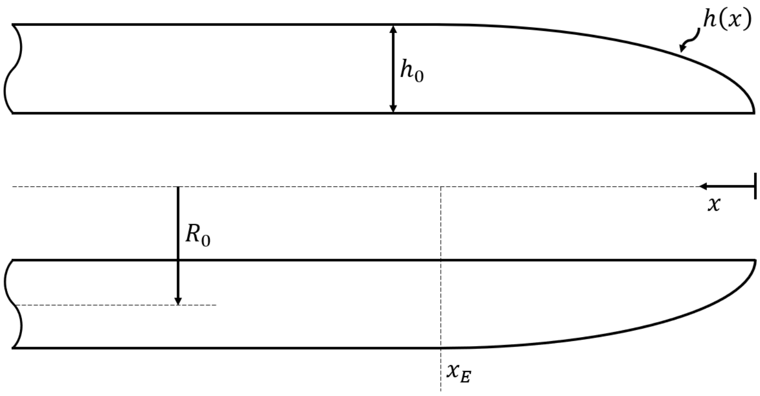

Figure 5.11: Power-law termination profile with $0 < n < 1$.

5.2.2 Investigating the ovalling mode, $m = 2$

Now, the ovalling mode ($m = 2$) is investigated for the model where $\nu, \epsilon_2 = 0$. Two separate expansion series are assumed in the form (5.76) and (5.77), based on the previous experience from Chapter 4, and will be used for the first and second branch respectively. For the first branch, the cut-on frequency Ω_{C1} is set to $(4\sqrt{15}t)/5$, while for the second branch, the cut-on frequency is set to $\sqrt{2}$ c.f. (5.51,5.52) on page 43.

The asymptotics of the first branch are now performed. Substituting (5.76) into the dispersion equation (5.50), and balancing terms at the $\mathcal{O}(\Omega^2)$ order gives x_0. Similarly, equating terms at the $\mathcal{O}(\Omega^3)$ order gives the second constant x_1. The constants for the first branch are found in (5.79) and (5.80). The asymptotic approximation can be found overlaid with the numerical solution in Figure 5.12.

$$\bar{k}(\Omega - \Omega_{C1}) = x_0(\Omega - \Omega_{C1})^{1/4} + x_1(\Omega - \Omega_{C1}) \tag{5.76}$$

$$\bar{k}(\Omega - \Omega_{C2}) = x_0(\Omega - \Omega_{C2})^{1/2} + x_1(\Omega - \Omega_{C2})^{3/2} \tag{5.77}$$

Constants x_0 and x_1 for first branch:

$$\Omega_{C1} = \frac{4t}{5} 15^{1/2} \tag{5.78}$$

$$x_0 = \left(\frac{-40\, {\Omega_{C1}}^3 + 192\, \Omega_{C1}\, t^2 + 40\, \Omega_C}{-8\, {\Omega_{C1}}^2\, t^2 + 34\, t^2 + 1} \right)^{1/4} \tag{5.79}$$

$$x_1 = \frac{\sqrt{2} \sqrt{(18\, t^2 + 11) \left(-8\, {\Omega_{C1}}^2\, t^2 + 34\, t^2 + 1\right)}}{-16\, {\Omega_{C1}}^2\, t^2 + 68\, t^2 + 2} \tag{5.80}$$

Following the same procedure, the asymptotics are performed for the second branch. Substituting (5.77) into the dispersion equation (5.50), and equating terms at the $\mathcal{O}(\Omega^2)$ order gives the first constant x_0 for the second branch. Similarly, equating terms at the $\mathcal{O}(\Omega^3)$ order gives the second constant x_1. The constants for the second branch are found in (5.82) and (5.83). The asymptotic approximation can be found overlaid with the numerical solution in Figure 5.12.

Constants x_0 and x_1 for second branch:

$$\Omega_{C2} = \sqrt{2} \tag{5.81}$$

$$x_0 = \frac{2\sqrt{2}\sqrt{-\Omega_{C2}\left(18\,\Omega_{C2}{}^2\,t^2 + 11\,\Omega_{C2}{}^2 - 132\,t^2\right)\left(-5\,\Omega_C{}^2 + 24\,t^2 + 5\right)}}{t^2\left(18\,\Omega_{C2}{}^2 - 132\right) + 11\,\Omega_{C2}{}^2} \tag{5.82}$$

$$x_1 = -\frac{8\,\Omega_{C2}{}^2\,t^2\,x_0{}^4 - 60\,\Omega_{C2}{}^2 + 36\,\Omega_{C2}\,t^2\,x_0{}^2 + 22\,\Omega_{C2}\,x_0{}^2 - 34\,t^2\,x_0{}^4 + 96\,t^2 - x_0{}^4 + 20}{2\,x_0\left(18\,\Omega_{C2}{}^2\,t^2 + 11\,\Omega_{C2}{}^2 - 132\,t^2\right)} \tag{5.83}$$

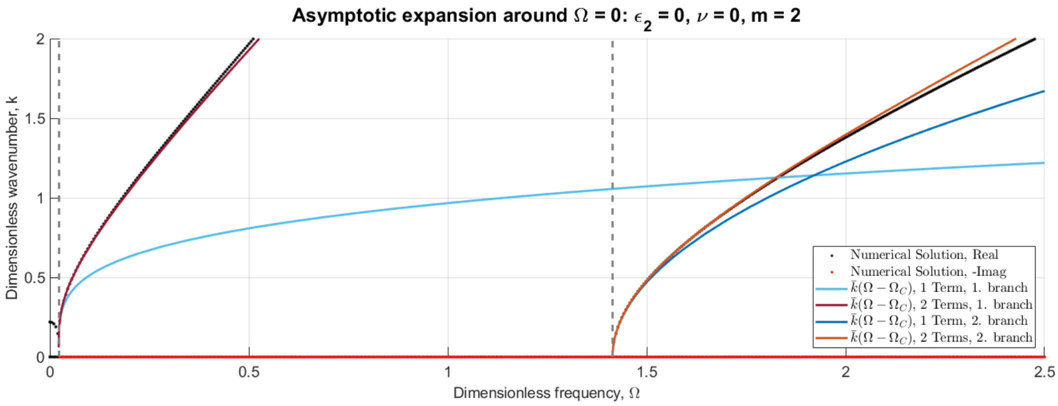

Figure 5.12: Asymptotic approximations overlaid with the numerical solution for cylindrical shell model where $\epsilon_2, \nu = 0$ ($m = 2$).

Having determined the low-frequency asymptotic approximations for the two branches, the acoustic black hole effect can now be investigated. Beginning the analysis with the first branch, phase- and group speed expressions are obtained as (5.84) and (5.85) based on the assumed asymptotic expansion (5.76). It is seen how the expressions only equal zero in cases where both x_0 and x_1 equal zero, disregarding the cut-on frequency $\Omega = \Omega_{C1}$. As neither x_0 nor x_1 will tend to zero for $t \to 0$, this hints towards the acoustic black hole effect not being present for the first branch in the low-frequency range. This is also confirmed by numerical calculations of the reflection coefficient and NWV. Next, the second branch is investigated in the same manner. The phase- and group speed expressions for this branch are identical to the ones for $m = 1$, and are given as (5.58) and (5.59) on page 45. Again, it is seen how the phase- and group speeds do not tend to zero for $t \to 0$, and numerical calculations confirmed the absence of the acoustic black hole effect in the low-frequency range.

$$c_p = \frac{\Omega}{k} = \frac{\Omega}{x_0(\Omega - \Omega_{C1})^{1/4} + x_1(\Omega - \Omega_{C1})} \tag{5.84}$$

$$c_g = \frac{\partial \Omega}{\partial k} = \frac{1}{x_1 + \frac{x_0}{4(\Omega - \Omega_{C1})^{3/4}}} \tag{5.85}$$

High-frequency solution: $\epsilon_2, \nu = 0$, $m = 2$:
As the effect was observed to be obtainable in the high-frequency range for $m = 1$, this will also be investigated for $m = 2$. The modal coefficient ξ is again introduced, to investigate the motion of the waves at various frequencies. In Figure 5.13, the modal coefficients have been plotted together with the two dispersion branches in a log-plot. For the first branch, it is seen how in the low-frequency range the wave is a mixture between u- and v-motion, but with increasing frequency, the v-motion becomes dominant. Right at the cut-on of the second branch, the wave is strongly dominated by u-motion, and remains this way with increasing frequency. Based on this observation, a high-frequency solution will be sought for the first branch using the same frequency scaling approach as previously.

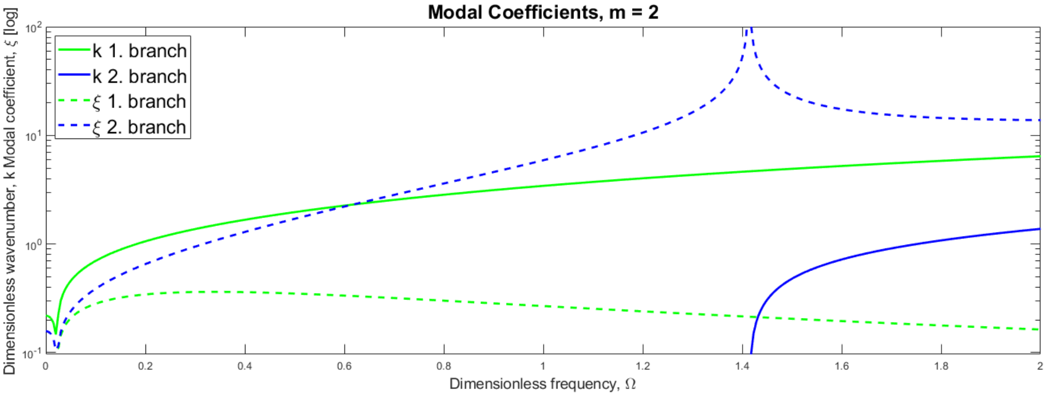

Figure 5.13: Modal coefficients, ξ, overlaid with wave numbers in log-plot to show which motion type is dominant at various frequencies for the two dispersion branches ($m = 2$).

The procedure is the same as described during the high-frequency analysis of the bending mode on page 46, but as a generalization, the asymptotic solution is now found for arbitrary m-values. The expansion series is assumed in the form $\bar{k_{rs}} = x_0 + x_1\eta + x_2\eta^2$.

The x_0 constant is found by balancing terms at the η^{-4} order, and the constant is expressed through non-scaled frequencies and wave numbers in (5.86). It is seen how setting $m = 1$ in the expression yields the previously obtained expression for x_0 for the bending mode (5.65) on page 47.

$$x_0 = \frac{\sqrt{\Omega}\,\left(m^2+1\right)^{1/4}}{\sqrt{m}\,\sqrt{t}} \tag{5.86}$$

The x_1 constant is found by balancing terms at the η^{-3} order, and the constant is expressed through non-scaled frequencies and wave numbers in (5.87).

$$x_1 = -\frac{2\,m^4\,t^2 - 4\,m^2\,t^2 + 2\,t^2 + 1}{8\,\sqrt{\Omega}\,m^{3/2}\,t^{3/2}\,\left(m^2+1\right)^{1/4}} \tag{5.87}$$

Finally, the x_2 constant is found by balancing terms at the η^{-2} order, and the constant is expressed through non-scaled frequencies and wave numbers in (5.88).

$$x_2 = \frac{-28\,m^8\,t^4 + 16\,m^6\,t^4 + 24\,m^4\,t^4 + 4\,m^4\,t^2 - 16\,m^2\,t^4 - 8\,m^2\,t^2 + 4\,t^4 + 4\,t^2 + 1}{128\,\Omega^{3/2}\,m^{5/2}\,t^{5/2}\,\left(m^2+1\right)^{3/4}} \tag{5.88}$$

After some algebraic manipulation, the high-frequency solution $\bar{k} = x_0 + x_1 + x_2$ is obtained as (5.89)†. The high-frequency solution can be found plotted against the numerical solution in Figure 5.14 for $m = 2$. The obtained solution is still only valid for the high-frequency range of $\Omega \gg\approx 10$, which is still far beyond the applicable range of the Goldenveizer-Novozhilov shell theory, and much higher frequency than most typical excitation frequencies of mechanical systems. In spite of this, the obtained solution will be analyzed for the acoustic black hole effect.

†As a form of validation, the solution was also evaluated for $m = 1$, which correctly yielded (5.70) on page 48.

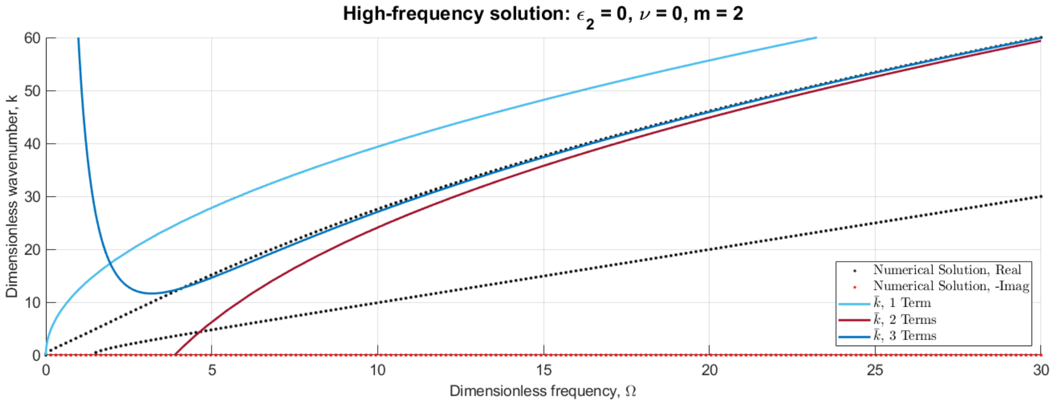

Figure 5.14: High-frequency asymptotic solution for cylindrical shell model having $\epsilon_2, \nu = 0$ ($m = 2$).

For simplicity, the high-frequency solution is expressed as a sum of $t^s c_s$ in (5.90), where $s \in [\frac{3}{2}, \frac{1}{2}, -\frac{1}{2}, -\frac{3}{2}, -\frac{5}{2}]$.

$$\bar{k} = \left\{ t^{3/2} \quad t^{1/2} \quad t^{-1/2} \quad t^{-3/2} \quad t^{-5/2} \right\} \left\{ \begin{matrix} 4 - 16m^2 + 24m^4 + 16m^6 - 28m^8 \\ 32\sqrt{m^2+1}\Omega(2m^3 - m^5 - m) \\ 4 - 8m^2 + 4m^4 + 128\Omega^2 m^2 + 128\Omega^2 m^4 \\ -16m\Omega\sqrt{m^2+1} \\ 1 \end{matrix} \right\} \frac{1}{128\Omega^{3/2} m^{5/2} (m^2+1)^{3/4}} \tag{5.89}$$

$$\bar{k} = t^{3/2} c_{\frac{3}{2}} + t^{1/2} c_{\frac{1}{2}} + t^{-1/2} c_{-\frac{1}{2}} + t^{-3/2} c_{-\frac{3}{2}} + t^{-5/2} = \sum t^s c_s \tag{5.90}$$

Expressing t in (5.90) through a power-law termination profile and integrating it with respect to x yields (5.91). The nature of the integral can now be evaluated for different powers of n.

$$\int \bar{k} dx = \int \sum t^s c_s dx = \sum \frac{\left(\frac{\epsilon^2}{12\,R^2}\right)^{s/2}}{n\,s+1} x^{ns+1} c_s \tag{5.91}$$

It can be seen how if $s > 0$, the summand converges, which is the case for $s = \frac{3}{2}$ and $s = \frac{1}{2}$. The remaining 3 terms however have $s < 0$, and the summand diverges, indicating the acoustic black hole effect. Setting $s = -1/2$, it is seen how the summand diverges for $n \geq 2$, and setting $s = -3/2$ & $-5/2$ the summand is seen to diverge for $n \geq 2/3$ & $2/5$ respectively. Again, the n-powers lower than unity result in a termination profile as presented in Figure 5.11 on page 49, which would violate the underlying assumption of low NWV. It can however be concluded, that the acoustic black hole effect can be obtained for a power-law termination profile of $n \geq 2$.

5.3 High-Frequency solution of ordinary shell model

It has now been shown, that the acoustic black hole effect is obtainable in the high-frequency range of the shell model with $\epsilon_2, \nu = 0$. When performing the asymptotics for the low-frequency range of this model, it was seen that the obtained solution was independent of t. This indicated that the obtained solution described a wave dominated by longitudinal motion, and it was determined from modal-coefficient analysis, that the wave only became flexural dominated at higher frequencies. From this observation, it was decided to investigate the high-frequency regime for the acoustic black hole effect. There is however no reason for assuming, that the acoustic black hole effect appeared in the high-frequency range due to the assumptions of $\epsilon_2, \nu = 0$. Because of this, a high-frequency solution will also be sought for the flexural wave numbers in the original cylindrical shell model.

The procedure is the same as described during the high-frequency analysis of the bending mode on page 46. The expansion series is assumed in the form $\bar{k_{rs}} = x_0 + x_1\eta + x_2\eta^2$, and the solution will be sought for arbitrary m-values.

The x_0 constant is found by balancing terms at the η^{-6} order, while the x_1 and x_2 constants are found by balancing terms at the η^{-5} and η^{-4} order respectively. The obtained constants are found as (5.92), (5.93) and (5.94). As the typical form of validation, the obtained solutions are plotted overlaid the numerical solutions for $m = 1$ in Figure 5.15, and for $m = 2$ in Figure 5.16[†]. If only x_0 is used the solution gives a good approximation in the *very* high-frequency range, far beyond the applicable range of the shell model. If x_1 and x_2 is included however, it is seen how the solution gives a good approximation after $\Omega > 1.5$, equivalent to $\omega \approx 1230\,rad/s$ for the geometry presented in Table 4.2 on page 21.

$$x_0 = \frac{\sqrt{\Omega}}{\sqrt{t}} \tag{5.92}$$

$$x_1 = -\frac{m^2\sqrt{t}}{2\sqrt{\Omega}} \tag{5.93}$$

$$x_2 = -\frac{m^4\,t^2 + 2\,m^2\,\nu^2\,t^2 - 8\,m^2\,\nu\,t^2 + 8\,m^2\,t^2 + 2}{8\,\Omega^{3/2}\sqrt{t}} \tag{5.94}$$

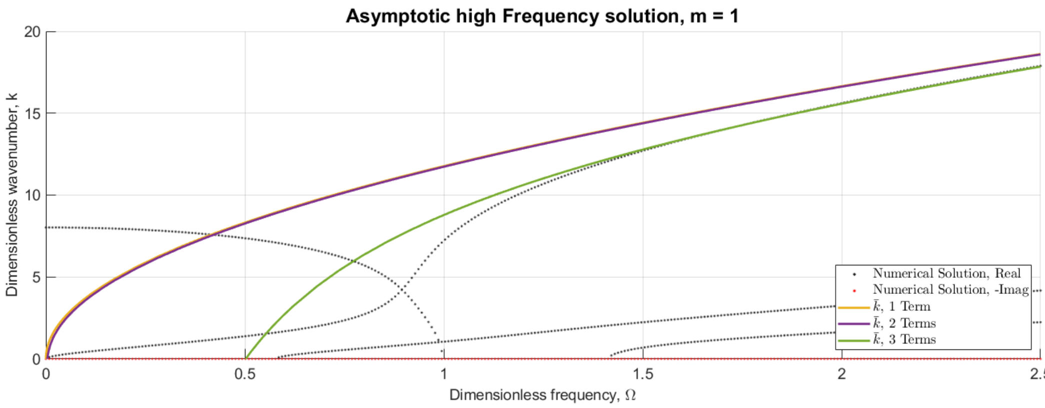

Figure 5.15: High-frequency asymptotic solution for original cylindrical shell model with no material- nor kinematic assumptions ($m = 1$).

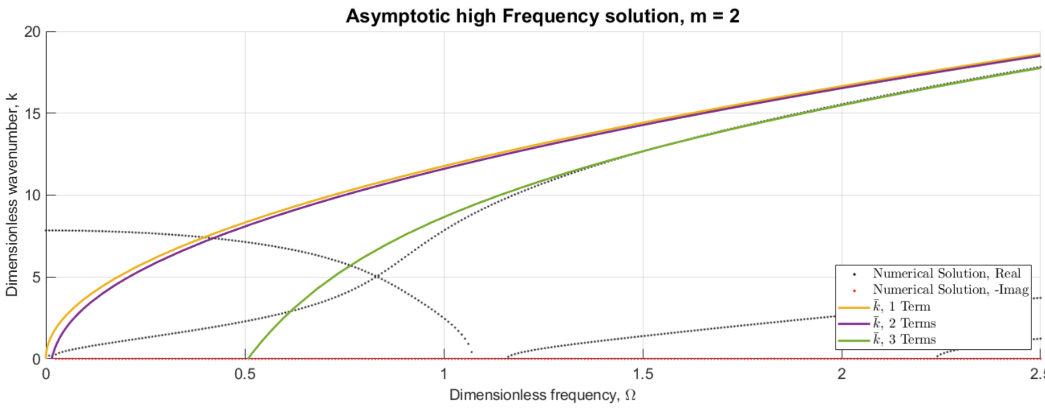

Figure 5.16: High frequency asymptotic solution for original cylindrical shell model with no material- nor kinematic assumptions ($m = 2$).

Next, the high-frequency wave number solution is integrated with respect to x, and the nature of the integral is assessed for different powers of n. The integral is performed in (5.95), where the first square bracket contains

[†]The solution was tested up to $m = 8$, and continued to give good approximations.

the integral of x_0. It is seen how the first term diverges for $n \geq 2$, indicating the acoustic black hole effect to be present in the very high-frequency range. The second square bracket contains the integral of x_1, and it is seen how this term never diverges, assuming $n > 0$ which would be necessary for a proper termination profile. The remaining two square brackets contain the integral of x_2, and it is seen how the former of the two never diverges, while the latter diverges for $n \geq 2$.

$$\int \bar{k} = -\left[\frac{2\,12^{1/4}\,\sqrt{\Omega}\,R^2\left(\frac{\epsilon^2}{R^2}\right)^{3/4}}{\epsilon^2\,(n-2)}\right]x^{1-n/2} \tag{5.95}$$

$$-\left[\frac{12^{3/4}\,m^2\left(\frac{\epsilon^2}{R^2}\right)^{1/4}}{12\sqrt{\Omega}\,(n+2)}\right]x^{1+n/2}-\left[\frac{m^2\,\left(m^2+2\,\nu^2-8\,\nu+8\right)\,\left(\frac{\epsilon^2}{12\,R^2}\right)^{3/4}}{4\,\Omega^{3/2}\,(3\,n+2)}\right]x^{1+3n/2}+\left[\frac{12^{1/4}\,R^2\left(\frac{\epsilon^2}{R^2}\right)^{3/4}}{2\,\Omega^{3/2}\,\epsilon^2\,(n-2)}\right]x^{1-n/2}$$

From these observations, it is seen how the acoustic black hole effect is obtainable in the slightly higher frequency range, than what was investigated previously in Chapter 4. The reason why the effect was not obtained in Chapter 4, was due to the asymptotic approximations only being representative in the low-frequency range, where the effect did not appear. The observation, that a power-law termination profile with $n \geq 2$ is sufficient to obtain the effect corresponds well with the observations made by M. A. Mironov in [9], and the observations made in [28] analyzing the flat plate.

5.4 Acoustic black hole effect for waves in circumferential direction

As a final investigation, the acoustic black hole effect will be analyzed for waves traveling in the circumferential direction of the cylindrical shell. The analysis is performed on the original cylindrical shell model, with no additional material- or kinematic assumptions. As the waves will travel in the circumferential direction the analysis will not be conducted on the full cylindrical shell, but instead on the partial cylindrical shell (curved plate) which was introduced previously in Figure 5.2 on page 35. As was shown previously, during the analysis of the curved plate, the dispersion equation for the curved plate can be obtained from the dispersion equation for the full cylindrical shell, by substituting m with $\frac{\pi m'}{\theta_0}$. Here m' is the circumferential wavenumber of the curved plate, and θ_0 is the angular span of the plate. The dispersion equation for the curved plate then becomes (5.96).

$$L_{jl}A_j = 0; j, l = 1, 2, 3 \tag{5.96}$$

$$L_{11} = k^2 + \frac{1-\nu}{2}\left(\frac{\pi m'}{\theta_0}\right)^2 - \Omega^2$$

$$L_{22} = \frac{1-\nu}{2}k^2 + \left(\frac{\pi m'}{\theta_0}\right)^2 + t^2 2(1-\nu)k^2 + t^2\left(\frac{\pi m'}{\theta_0}\right)^2 - \Omega^2$$

$$L_{33} = 1 + t^2(k^2 + \left(\frac{\pi m'}{\theta_0}\right)^2)^2 - \Omega^2$$

$$L_{12} = -L_{21} = \frac{1+\nu}{2}\left(\frac{\pi m'}{\theta_0}\right)ik$$

$$L_{13} = -L_{31} = \nu ik$$

$$L_{23} = L_{32} = \left(\frac{\pi m'}{\theta_0}\right) + t^2\left(\frac{\pi m'}{\theta_0}\right)^3 + t^2(2-\nu)\left(\frac{\pi m'}{\theta_0}\right)k^2$$

$$k = k_x R \qquad t^2 = \frac{h^2}{12R^2} \qquad \Omega^2 = \frac{\omega^2 R^2}{c_L^2} = \frac{\rho(1-\nu^2)\omega^2 R^2}{E} \tag{5.97}$$

For the analysis of waves in the circumferential direction, dispersion characteristics are investigated for the m' wave number as a function of dimensionless frequency, Ω. This will be done keeping the longitudinal wave number, k, constant, and for simplicity, the analysis will consider $k = 0$. For this case, it can be seen how the L_{12} and L_{13} terms equal zero, meaning the longitudinal motion is decoupled from the circumferential and radial motion. Condensing this equation from the system, the dispersion equation can be written compactly as (5.98).

$$t^2\, m'^6 + \left(-\Omega^2\, t^2 - 2\, t^2\right)\, m'^4 + \left(-\Omega^2\, t^2 - \Omega^2 + t^2\right)\, m'^2 + \Omega^4 - \Omega^2 = 0 \tag{5.98}$$

A numerical solution for (5.98) is obtained excluding the dispersionless longitudinal branch. Figure 5.17 shows the solution in the *very* low-frequency range, and 5.18 shows the solution spanning $\Omega \in [0, 2]$. It can be seen how for any frequency 6 waves must be present, as (5.98) is a 6^{th} order polynomial in m'. The figure shows 3 branches for any frequency, but this is as always just due to the waves in the positive half-space of the waveguide being plotted. It can be seen how 2 purely real branches are present in the plotted frequency range. One appears to start from $(\Omega, m') = (0, 0.5)$ and another cuts on at $\Omega = 1$.

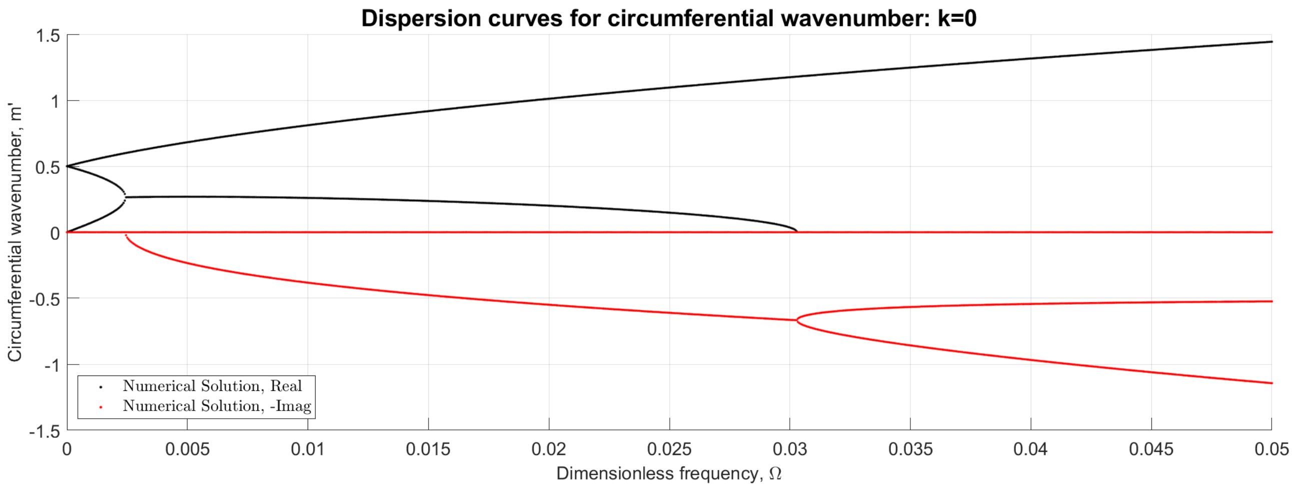

Figure 5.17: Numerical solution of dispersion curves for circumferential wavenumber m'. $k = 0$. Very low-frequency range.

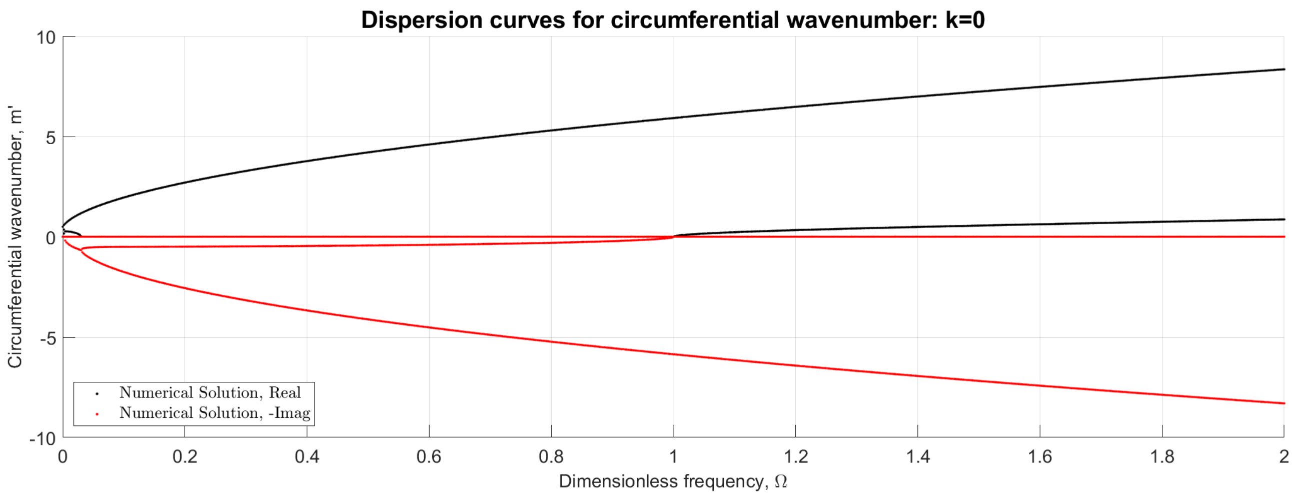

Figure 5.18: Numerical solution of dispersion curves for circumferential wavenumber m'. $k = 0$.

Now asymptotic approximations can be found for the dispersion equation. This is done in Appendix D, as the process is identical to what has already been presented several times. The asymptotic approximations are found in the low-frequency range by expanding around small values of Ω, and a low-frequency solution is obtained for both the first and second branches. The asymptotic approximation for the first branch, $\bar{m'}_{B1}$, is found as (5.99), while the approximation for the second branch, $\bar{m'}_{B2}$, is found as (5.100). In the following derivations, the circumferential wavenumber could reasonably be normalized by θ_0, but this has not been done and instead, all figures are generated with an assumed angle of $\theta_0 = \pi/2$.

$$\bar{m'}_{B1} = \frac{\theta_0}{\pi} - \frac{\Omega^2\,\theta_0}{2\,t^2\,\pi} + \frac{\sqrt{2}\,\Omega\,\theta_0\,\sqrt{t^2+1}}{2\,t\,\pi} \tag{5.99}$$

$$\bar{m'}_{B2} = \Omega^{1/2}\,\frac{\sqrt{2}\,\theta_0}{\pi} - \Omega^{3/2}\,\frac{\sqrt{2}\,\theta_0\,\left(16\,t^2-1\right)}{4\,\pi} \tag{5.100}$$

To investigate the acoustic black hole effect, a new termination profile must be introduced. The termination profile still follows the power-law profile but is now expressed as a function of θ, as $h(\theta) = \epsilon\theta^n$. This termination profile is substituted into the expression for t to obtain $t = \sqrt{\frac{h(\theta)^2}{12R^2}}$, which is then substituted into (5.99) and (5.100).

Now (5.99) will be integrated with respect to θ, and the nature of the integral will be evaluated for various powers of n. It can be seen how the first two terms in (5.99) can be integrated quite straightforwardly, but the third term poses some issues. The $\sqrt{t^2+1}$ in the numerator makes it difficult to evaluate the integral analytically, even with the help of symbolic manipulation. It is however observed, that both the numerator and the denominator of the third term are of order t^1, and the term is therefore not expected to diverge for $t \to 0$. Because of this, the third term is not expected to contribute to the acoustic black hole effect. Based on this observation, the integral of the third term will not be pursued. The remaining terms are integrated, to obtain (5.101). Here it is immediately seen how the second term of (5.101) will diverge for $n \geq \frac{1}{2}$ if the integral is evaluated at $\theta = 0$. As discussed earlier on page 52, a power-law termination profile with $n \leq 1$ would violate the underlying assumption of low NWV, and so a value of $n \geq 2$ is argued to be a sufficient termination profile power for the acoustic black hole effect to appear for waves propagating in the circumferential direction.

$$\int \bar{m'}_{B1} d\theta = \frac{\theta\,\theta_0}{\pi} + \frac{6\,\Omega^2\,R^2\,\theta^{1-2\,n}\,\theta_0}{\varepsilon^2\,\pi\,(2\,n-1)} + \int \frac{\sqrt{2}\,\Omega\,\theta_0\,\sqrt{t^2+1}}{2\,t\,\pi} d\theta \tag{5.101}$$

Now, the same analysis is performed for the second branch, using the low-frequency solution (5.100). The expression is integrated with respect to θ to obtain (5.102). Here it can be seen, that the acoustic black hole effect does not appear for the second branch, as no value of n causes (5.102) to diverge when evaluated at $\theta = 0$.

$$\int \bar{m'}_{B2} d\theta = \frac{\sqrt{2}\,\theta\,\theta_0\,\sqrt{\Omega-1}\,(\Omega+3)}{4\,\pi} - \frac{\sqrt{2}\,\varepsilon^2\theta^{2\,n+1}\,\theta_0\,(\Omega-1)^{3/2}}{3\,R^2\,\pi\,(2\,n+1)} \tag{5.102}$$

One might now reasonably argue, based on the previous observations, that the acoustic black hole effect may be observed if a high-frequency solution is obtained for the second branch. In fact, a high-frequency solution was obtained, but as the second branch becomes completely dispersionless (linear) shortly after its cut-on at $\Omega = 1$, the high-frequency solution was simply a linear function of Ω, independent of t. Because of this, the acoustic black hole effect can be confirmed not to appear for the second branch.

5.5 Answering SRQ 3

For which geometries does the acoustic black hole effect appear, and what causes the effect to be absent in some cases? Which assumptions can be employed to make the effect appear in the absent cases?

In this chapter, the acoustic black hole effect was investigated, starting from a simple case of a flat plate carrying flexural waves. The analysis showed how the effect appeared for this simple case, and how the terms in the differential equations of motion gave rise to the effect. The analysis was then extended to a curved shell, and it was observed how the analysis of this geometry was functionally identical to the analysis of the full cylindrical shell.

As the acoustic black hole effect had been observed for the plate, and not in the cylindrical shell, it was attempted to pinpoint which terms (or couplings) in the equations caused the effect to be absent. Starting from the simplest case of $m = 0$, it was observed how a material assumption of $\nu = 0$ could uncouple the flexural motion from the longitudinal, making the equation for the cylindrical shell equivalent to that of a simple beam on a Winkler foundation. It was then shown how the acoustic black hole effect was present under this material assumption with $m = 0$ in the low-frequency range. Next, the equations of motion for the cylindrical shell were investigated for $m > 0$. It was discussed, that the equation governing the flexural motion contained terms related to the membrane forces in the shell, which were not present in the case of the flat plate (together with the Poisson-coupling terms which were also present for $m = 0$).

It was postulated that the removal of these terms may lead to the acoustic black hole effect. To remove these terms, the equations of motion were derived rigorously through Hamilton's principle assuming $\epsilon_2, \nu = 0$. From this derivation, it was shown how the membrane terms could be condensed from the equation by setting strain in the circumferential direction to zero. However, the following asymptotic analysis showed how the acoustic black hole effect was not present in the low-frequency range for $m > 0$ in spite of these newly introduced material- and kinematic assumptions.

Modal coefficient analysis was performed next, which showed how the low-frequency wave motion was governed by a substantial amount of longitudinal motion, and how for increasing frequency, the wave motion started becoming almost purely flexural. As the acoustic black hole effect is expected to be most pronounced for flexural motion, a high-frequency solution was sought for the dispersion equation. This was obtained using a frequency scaling approach together with the dominant balance method. The analysis showed how the acoustic black hole effect was present in the high-frequency range for $m > 0$, using power-law termination profiles where $h \to 0$. A termination profile with $n > 2/5$ was predicted to be sufficient for the effect to appear, but this would violate the underlying assumption of low NWV, and so a power-law termination profile with $n > 2$ is concluded to be sufficient for the effect to appear.

A high-frequency solution was then obtained for the original shell model, with no material- or kinematic assumptions. Here it was found that the acoustic black hole effect was present when using power-law termination profiles where $h \to 0$ for $n \geq 2$. Finally, the cylindrical shell was investigated for waves traveling in the circumferential direction by investigating the dispersion characteristics of the circumferential wavenumber. This was done for the curved plate geometry, setting $k = 0$. It was found that the effect does appear when employing a power-law termination profile where $h(\theta) \to 0$.

6 Answering the Main Research Question

The three Sub Research Questions have now been answered in chapters 3, 4, and 5 respectively. Now the Main Research Question will now be answered, based on the conclusions of the previous three Sub Research Questions. The Main Research Question is repeated as:

How can the acoustic black hole effect be modeled for elastic cylindrical shells, through the framework of thin shell theory?

It was discussed how the acoustic black hole effect can be obtained through a gradual reduction in the flexural rigidity of the waveguide, typically obtained from a gradual reduction in thickness. It was discussed how the model validity relied on an assumption of low Normalized Wave number Variation, and how this assumption was violated if the termination profile was too abrupt. It was shown how the acoustic black hole effect could be analyzed by the divergent nature of the anti-derivative of the wavenumber, in the idealized case of $h \to 0$. If instead, a residual height is present at the tip of the termination profile, numerical evaluations of the reflection coefficient provide insight into the performance of the given termination profile.

The Goldenveizer-Novozhilov cylindrical shell model was analyzed using asymptotic approximations in the low-frequency range. The asymptotic approximation for the breathing mode was obtained by using ν^2 as the expansion parameter, while the approximations for the bending and ovalling mode were obtained by using Ω as the expansion parameter, offset with the cut-on frequency of each respective branch. The subsequent analysis showed that the acoustic black hole effect was not present in the low-frequency range for any m-spectrum if termination profiles where the shell thickness was reduced to zero ($h \to 0$) were used. However, if a termination profile was used, where both shell- thickness, and radius went to zero ($h, R \to 0$), the effect was observed through numerical evaluation of the reflection coefficient in the low-frequency range.

It was observed how the acoustic black hole effect may be obtained in the low-frequency range with $m = 0$, if Poisson effects are neglected. From a high-frequency solution, the acoustic black hole effect was observed for the full cylindrical shell for power-law termination profiles having $n \geq 2$ where $h \to 0$. Finally, it was observed how the effect may be obtained for waves traveling in the circumferential direction also.

This thesis has successfully demonstrated the feasibility of modeling the acoustic black hole effect for cylindrical shells, a significant advancement beyond previous studies limited to beams and flat plates. The observation, that a power-law termination profile with $n \geq 2$ is sufficient to obtain the acoustic black hole effect in the cylindrical shell corresponds well with the observations originally made by M. A. Mironov in [9] investigating a beam model, and the observations made in [28] analyzing the flat plate, where in both cases it was concluded how $n \geq 2$ would cause the effect to appear.

In contrast to the previously analyzed models that showed the effect to be present across the entire frequency range, the current findings suggest the acoustic black hole effect in cylindrical shells to be present predominantly at higher frequencies. This is a result of the flexural wave motion of the cylindrical shell being strongly coupled with the longitudinal motion in the low-frequency range. With higher frequency, the wave motion becomes more purely flexural, allowing the acoustic black hole effect to appear, which serendipitously coincides well with the requirement of low Normalized Wave number Variation.

7 Conclusion

Like a modern-day California Gold Rush, the academic community has sprung into action, analyzing the acoustic black hole effect through numerical models. They have developed models, which allow us to analyze phenomena of acoustic black holes with remarkable speed and which would have taken countless hours to analyze analytically. There is no doubt, that numerical solutions are the way of the modern engineer, and with the tools available today, a thesis like the current text may seem more like a mathematical exercise, than an attempt to further the field of acoustic black holes. The analytical approach does however provide something one can never hope to obtain from a sparse matrix or a color-plot.

If you asked a monkey to go to the moon, he would undoubtedly find the tallest tree he could, and climb it. From up there he would look disappointed to the sky. He might also be able to spot a slightly taller tree in the distance and decide to climb that next; "surely I'll get to the moon eventually" he thinks to himself. But if we ever want to get that monkey to the moon, we have to stick him in a rocket, and before then, we have to *invent a rocket*. Sometimes the only way forward is to think in completely new directions, and we are able to do that through a rigorous understanding of the underlying problem.

Analyzing a problem solely based on numerical models is like building a rocket without a blueprint. You may be able to get the job done quicker without a pesky inspector breathing down your neck; especially if you have built a similar rocket previously. But without a sound understanding of *why* the rocket you have built doesn't just fall out of the sky, you can never hope to build a bigger and better rocket in the future. Designing the blueprint - developing the analytical understanding - is why we as engineers are able to build a better rocket tomorrow.

Throughout this thesis, the acoustic black hole effect has been investigated for cylindrical shells, using a theoretical, analytical, and academically motivated approach. It has been shown, that there is an analytical basis for the acoustic black hole effect in cylindrical shells, and that the effect can be obtained in a similar manner as for beams and plates. An interesting property of the cylindrical shell is, however, that the effect should not be expected in the low-frequency range, even if a termination profile could be designed, resulting in sufficiently low Normalized Wave number Variation at lower frequencies.

This means, that if an engineer wishes to exploit the acoustic black hole effect at lower frequencies, he can not simply employ a termination profile that gives low Normalized Wave number Variation in the desired frequency range. He would instead have to conceive of some way, of making the wave motion almost purely flexural in this low-frequency range, for the effect to be obtainable. One might imagine a series of longitudinal cuts into the end of the acoustic black hole termination, turning it into a number of beam-like acoustic black holes. Maybe these beam-like acoustic black holes should be placed standing radially from the pipe, so that they may also be excited by torsional vibrations. Who knows? Maybe the monkey is about to invent a rocket.

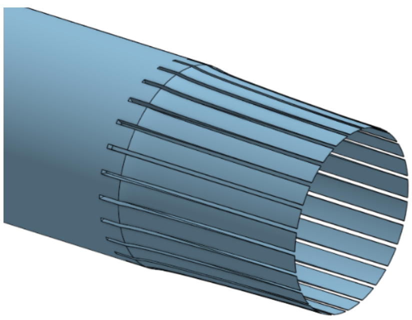

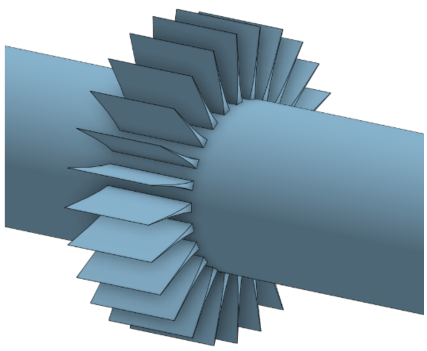

8 Future Work

Throughout this thesis, very little effort has been spent discussing the industrial applicability of acoustic black holes in cylindrical shells. One of the biggest points of critique for the current state of acoustic black hole technology, is the limited range of industrial applicability, due to the physical dimensions and the effective frequency ranges. Also, the use of unit-less parameters for the analysis in this thesis, makes it difficult to relate the analyzed geometries to real-world components. All of the conclusions in Chapter 5, stating that the acoustic black hole effect is present, do so based on analytical calculations on a termination profile geometry which is impossible to manufacture. In future work, a greater focus may be directed toward designing acoustic black holes for real-world mechanical systems, keeping in mind physical dimensions, manufacturability, and structural rigidity. Additionally, maybe acoustic black holes should not be restricted to be an integral part of a waveguide, but instead be manufactured as a separate component, intended to be mounted to a waveguide or mechanical system as a retrofit part.

At the end of Chapter 5, it was shown how the acoustic black hole effect may be obtained in cylindrical shells, in the idealized case where the shell thickness goes to zero. As a next step, it would be interesting to investigate the non-ideal case where the termination profile has a non-zero h_r-value. This could potentially be done through numerical evaluation of the reflection coefficient or using some elaborate numerical model. Additionally, performing sensitivity studies to investigate how sensitive the obtained vibration mitigation is to changes in termination profile geometry and residual height at the tip of the termination, may give a future design engineer the perspective to design acoustic black holes where performance is balanced against the presumably high manufacturing costs.

Many cylindrical shell structures used in industry are either submerged in or filled with fluid and the shell thickness is often too large to adhere to Love's first approximation. For the technology to be applied in industry, the effect should be investigated and proven for thicker shells as well as shells with heavy fluid loading. The inclusion of fluid loading in the analysis may even open new doors for applying acoustic black holes for mitigation of e.g. pressure pulsations in the fluid.

Acoustic black hole technology has, maybe due to its name, been viewed as a means for sound- and vibration mitigation, but it may have much more far-reaching applicability outside of this area. It has already been investigated for energy harvesting, but one could imagine the technology to be employed in anything from ultrasonic welding, to hearing aids, Hi-Fi tweeter design, and ultrasonic transducers. We have just begun to scratch the surface, and it all starts with a rigorous understanding of the underlying physics and vibration theory.

Bibliography

[1] L. Cremer, M. Heckl, and B.A.T. Petersson. *Structure-Borne Sound*. Springer, 2005. 3rd.

[2] Adrien Pelat, François Gautier, Stephen C. Conlon, and Fabio Semperlotti. The acoustic black hole: A review of theory and applications. *Journal of Sound and Vibration*, 476, June 2020. doi: 10.1016/j.jsv.2020.115316. URL https://doi.org/10.1016/j.jsv.2020.115316.

[3] Philip A. Feurtado, Stephen C. Conlon, and Fabio Semperlotti. A normalized wave number variation parameter for acoustic black hole design. *The Journal of the Acoustical Society of America*, 136(2): EL148–EL152, August 2014. doi: 10.1121/1.4890205. URL https://doi.org/10.1121/1.4890205.

[4] Victor V. Krylov. Acoustic black holes: recent developments in the theory and applications. *IEEE Transactions on Ultrasonics, Ferroelectrics, and Frequency Control*, 61(8):1296–1306, August 2014. doi: 10.1109/tuffc.2014.3036. URL https://doi.org/10.1109/tuffc.2014.3036.

[5] Victor V. Krylov. Acoustic black holes for flexural waves: A smart approach to vibration damping. *Procedia Engineering*, 199:56–61, 2017. doi: 10.1016/j.proeng.2017.09.150. URL https://doi.org/10.1016/j.proeng.2017.09.150.

[6] Kaushik Sampath, Caleb F. Sieck, Matthew D. Guild, and Charles Rohde. Incorporating acoustic black holes in hydrofoils. *The Journal of the Acoustical Society of America*, 146(4):2838–2838, October 2019. doi: 10.1121/1.5136837. URL https://doi.org/10.1121/1.5136837.

[7] E.P. Bowyer and V.V. Krylov. Damping of flexural vibrations in turbofan blades using the acoustic black hole effect. *Applied Acoustics*, 76:359–365, February 2014. doi: 10.1016/j.apacoust.2013.09.009. URL https://doi.org/10.1016/j.apacoust.2013.09.009.

[8] Jie Deng, Oriol Guasch, and Ling Zheng. A semi-analytical method for characterizing vibrations in circular beams with embedded acoustic black holes. *Journal of Sound and Vibration*, 476:115307, June 2020. doi: 10.1016/j.jsv.2020.115307. URL https://doi.org/10.1016/j.jsv.2020.115307.

[9] M. A. Mironov. Propagation of flexural wave in a plate whose thickness decreases smoothly to zero in a finite interval. *Academy of Sciences of the USSR*, 34, 1988.

[10] Wei Huang, Hongli Ji, Jinhao Qiu, and Li Cheng. Analysis of ray trajectories of flexural waves propagating over generalized acoustic black hole indentations. *Journal of Sound and Vibration*, 417: 216–226, March 2018. doi: 10.1016/j.jsv.2017.12.012. URL https://doi.org/10.1016/j.jsv.2017.12.012.

[11] Benjamin B. Støttrup, Sergey Sorokin, and Horia D. Cornean. A rigorous approach to optimal profile design for acoustic black holes. *The Journal of the Acoustical Society of America*, 149(1):447–456, January 2021. doi: 10.1121/10.0003337. URL https://doi.org/10.1121/10.0003337.

[12] Angelis Karlos, Stephen J. Elliott, and Jordan Cheer. Higher-order WKB analysis of reflection from tapered elastic wedges. *Journal of Sound and Vibration*, 449:368–388, June 2019. doi: 10.1016/j.jsv.2019.02.041. URL https://doi.org/10.1016/j.jsv.2019.02.041.

[13] Rasmus Nielsen and Sergey Sorokin. The WKB approximation for analysis of wave propagation in curved rods of slowly varying diameter. *Proceedings of the Royal Society A: Mathematical, Physical and Engineering Sciences*, 470(2167):20130718, July 2014. doi: 10.1098/rspa.2013.0718. URL https://doi.org/10.1098/rspa.2013.0718.

[14] Kasper S. Sørensen, Horia D. Cornean, and Sergey Sorokin. Optimal profile design for acoustic black holes using timoshenko beam theory. *The Journal of the Acoustical Society of America*, 153(3): 1554–1563, March 2023. doi: 10.1121/10.0017322. URL https://doi.org/10.1121/10.0017322.

[15] C. A. McCormick. *OPTIMIZATION OF ACOUSTIC BLACK HOLES FOR VIBRATION REDUCTION*, 2021. URL https://etda.libraries.psu.edu/files/final_submissions/24837.

[16] Arthur W. Leissa. *Vibration of shells*. JOHN WILEY SONS, INC., 1973. NASA SP-288.

[17] Singiresu S. Rao. *Vibration of Continuous Systems*. JOHN WILEY SONS, INC., 2007. 1st.

[18] P. Gardonio F.J. Fahy. *Sound and Structural Vibration*. Academic Press, 2006. 2nd.

[19] R. Chapling. Asymptotic methods: A course in part ii of the mathematical tripos. University of Cambridge, England, 2016.

[20] E.J. Hinch. *Pertubation Methods*. Cambridge University Press, 1991. First Edition.

[21] S. V. Sorokin. An introduction to the theory of wave propagation in elastic cylindrical shells filled with an acoustic medium. Lecture Notes.

[22] Lasse S. Ledet and Sergey V. Sorokin. Bi-orthogonality relations for fluid-filled elastic cylindrical shells: Theory, generalisations and application to construct tailored green's matrices. *Journal of Sound and Vibration*, 417:315–340, March 2018. doi: 10.1016/j.jsv.2017.12.010. URL https://doi.org/10.1016/j.jsv.2017.12.010.

[23] S.V. Sorokin, J.B. Nielsen, and N. Olhoff. Green's matrix and the boundary integral equation method for the analysis of vibration and energy flow in cylindrical shells with and without internal fluid loading. *Journal of Sound and Vibration*, 271(3-5):815–847, April 2004. doi: 10.1016/s0022-460x(03)00755-7. URL https://doi.org/10.1016/s0022-460x(03)00755-7.

[24] Jie Deng, Oriol Guasch, Laurent Maxit, and Zheng Ling. Annular acoustic black holes to reduce propagative bloch- floquet flexural waves in periodically supported cylindrical shells. 05 2019.

[25] Jie Deng, Oriol Guasch, Laurent Maxit, and Ling Zheng. Vibration of cylindrical shells with embedded annular acoustic black holes using the rayleigh-ritz method with gaussian basis functions. *Mechanical Systems and Signal Processing*, 150:107225, March 2021. doi: 10.1016/j.ymssp.2020.107225. URL https://doi.org/10.1016/j.ymssp.2020.107225.

[26] Dayuan Zheng, Jingtao Du, Yang Liu, and Wensheng Zhao. Dynamic behavior and power flow analyses of a cylindrical shell structure embedded with acoustic black holes. *Applied Acoustics*, 208:109349, June 2023. doi: 10.1016/j.apacoust.2023.109349. URL https://doi.org/10.1016/j.apacoust.2023.109349.

[27] MATLAB. *Symbolic Math Toolbox*, 2023. URL https://se.mathworks.com/products/symbolic.html.

[28] D.J. O'Boy, V.V. Krylov, and V. Kralovic. Damping of flexural vibrations in rectangular plates using the acoustic black hole effect. *Journal of Sound and Vibration*, 329(22):4672–4688, October 2010. doi: 10.1016/j.jsv.2010.05.019. URL https://doi.org/10.1016/j.jsv.2010.05.019.

[29] Clive L. Dym and Irving H. Shames. *Solid Mechanics*. Springer New York, 2013. doi: 10.1007/978-1-4614-6034-3. URL https://doi.org/10.1007/978-1-4614-6034-3.

[30] Abhijit Sarkar and Venkata R. Sonti. Asymptotic analysis for the coupled wavenumbers in an infinite fluid-filled flexible cylindrical shell: The beam mode. *Journal of Sound and Vibration*, 319(1-2):646–667, January 2009. doi: 10.1016/j.jsv.2008.06.008. URL https://doi.org/10.1016/j.jsv.2008.06.008.

Appendix A: Terms from the low-frequency asymptotic approximations

A

A.1 Terms of the $m = 0$ analysis

$$x_0 = \Omega \tag{A.1}$$

$$x_1 = \frac{\Omega}{2(1 - \Omega^2 + \Omega^4 t^2)} \tag{A.2}$$

A.2 Terms of the $m = 1$ analysis

First branch

$$x_0 = \left(\frac{-2}{\nu^2 t^2 + \nu^2 - t^2 - 1} \right)^{1/4} \tag{A.3}$$

$$x_1 = -\frac{-2\,\nu^2\,t^2 + 2\,\nu^2 - 4\,\nu\,t^4\,{x_0}^4 - 4\,\nu\,t^2\,{x_0}^4 + 7\,\nu\,t^2 + 3\,\nu + 4\,t^4\,{x_0}^4 + 4\,t^2\,{x_0}^4 - 9\,t^2 - 5}{4\,x_0\,(t^2+1)^2\,(\nu-1)^2\,(\nu+1)} \tag{A.4}$$

Second branch

$$x_0 = 2^{3/4} \sqrt{\frac{(1-\nu)^{1/2}(4t^2 + \nu + 3)}{5\nu^2 + 2\nu t^2 + 2\nu - 10t^2 - 7}} \tag{A.5}$$

$$x_1 = -(2^{1/4}(1-\nu)^{1/2}(48\nu^5 t^2 - 121\nu^5 + 96\nu^4 t^4 - 320\nu^4 t^2 - 159\nu^4 - 384\nu^3 t^6 - 1444\nu^3 t^4 \tag{A.6}$$

$$-720\nu^3 t^2 + 134\nu^3 + 240\nu^2 t^6 + 1276\nu^2 t^4 + 1424\nu^2 t^2 + 418\nu^2 + 544\nu t^6 + 1204\nu t^4 + 608\nu t^2 \tag{A.7}$$

$$+3\nu - 656t^6 - 1388t^4 - 1040t^2 - 275))/(2(-(1-\nu)^{3/2}(5\nu^3 + 22\nu^2 t^2 + 17\nu^2 + 8\nu t^4 + 4\nu t^2 \tag{A.8}$$

$$-\nu - 40t^4 - 58t^2 - 21))^(1/2)(5\nu^2 + 2\nu t^2 + 2\nu - 10t^2 - 7)^2) \tag{A.9}$$

Third branch

$$x_0 = \frac{2^{3/4}\,\sqrt{\sqrt{t+1}\,\left(\nu + 14\,t + 2\,\nu\,t - \nu\,t^2 + 5\,t^2 - 8\,t^3 + 3\right)}}{\sqrt{t+1}\,\left(-2\,\nu^2\,t^2 + 2\,\nu^2 - 8\,\nu\,t^3 - \nu\,t^2 - 2\,\nu\,t + \nu + 16\,t^3 + 7\,t^2 + 6\,t + 1\right)} \tag{A.10}$$

A.3 Terms of the $m = 2$ analysis

First branch

$$
\begin{aligned}
&x_0 = [-(4\Omega_{C1}(10\nu - 4\Omega_{C1}^2\nu + 40\nu t^2 + 14\Omega_{C1}^2 - 3\Omega_{C1}^4 - 76t^2 + 40\Omega_{C1}^2 t^2 - 10))\\
&/(2\Omega_{C1}^4 t^2 + 8\Omega_{C1}^2\nu^2 t^4 + 16\Omega_{C1}^2\nu t^2 + \Omega_{C1}^2\nu - 8\Omega_{C1}^2 t^4 - 40\Omega_{C1}^2 t^2 - \Omega_{C1}^2 + 16\nu^3 t^4\\
&-4\nu^3 t^2 + \nu^3 - 16\nu^2 t^4 + 4\nu^2 t^2 - \nu^2 - 16\nu t^4 - 68\nu t^2 - \nu + 16t^4 + 68t^2 + 1)]^{1/4}
\end{aligned}
$$

$$
\begin{aligned}
&x_1 = (2^{1/2}(-240\Omega_{C2}^6\nu t^4 - 60\Omega_{C2}^6\nu t^2 + 48\Omega_{C2}^6 t^4 + 180\Omega_{C2}^6 t^2 + 192\Omega_{C2}^4\nu^3 t^6 + 48\Omega_{C2}^4\nu^3 t^4\\
&-960\Omega_{C2}^4\nu^2 t^6 - 128\Omega_{C2}^4\nu^2 t^4 + 20\Omega_{C2}^4\nu^2 t^2 + 6\Omega_{C2}^4\nu^2 + 3648\Omega_{C2}^4\nu t^6 - 344\Omega_{C2}^4\nu t^4 - 66\Omega_{C2}^4\nu t^2\\
&-24\Omega_{C2}^4\nu - 2880\Omega_{C2}^4 t^6 + 984\Omega_{C2}^4 t^4 - 146\Omega_{C2}^4 t^2 + 18\Omega_{C2}^4 + 448\Omega_{C2}^2\nu^4 t^6\\
&-16\Omega_{C2}^2\nu^4 t^4 + 6\Omega_{C2}^2\nu^4 - 2720\Omega_{C2}^2\nu^3 t^6 + 248\Omega_{C2}^2\nu^3 t^4 - 72\Omega_{C2}^2\nu^3 t^2 - 26\Omega_{C2}^2\nu^3\\
&+6368\Omega_{C2}^2\nu^2 t^6 - 1048\Omega_{C2}^2\nu^2 t^4 - 268\Omega_{C2}^2\nu^2 t^2 + 5\Omega_{C2}^2\nu^2 - 8416\Omega_{C2}^2\nu t^6 + 7816\Omega_{C2}^2\nu t^4\\
&+1536\Omega_{C2}^2\nu t^2 + 44\Omega_{C2}^2\nu + 4320\Omega_{C2}^2 t^6 - 7384\Omega_{C2}^2 t^4 - 1196\Omega_{C2}^2 t^2 - 29\Omega_{C2}^2 + 128\nu^5 t^6\\
&-64\nu^5 t^4 + 16\nu^5 t^2 - 2\nu^5 - 960\nu^4 t^6 + 128\nu^4 t^4 - 32\nu^4 t^2 - 7\nu^4 + 2816\nu^3 t^6 - 928\nu^3 t^4\\
&+232\nu^3 t^2 + 22\nu^3 - 1152\nu^2 t^6 + 4544\nu^2 t^4 + 448\nu^2 t^2 - 4\nu^2 - 2944\nu t^6 - 12832\nu t^4 - 1544\nu t^2\\
&-20\nu + 2112t^6 + 9152t^4 + 880t^2 + 11)^{1/2})/(2(\nu^3 - \nu^2 - \nu + \Omega_{C2}^2(\nu - 1)\\
&+2t^2(\Omega_{C2}^4 + 8\Omega_{C2}^2\nu - 20\Omega_{C2}^2 - 2\nu^3 + 2\nu^2 - 34\nu + 34) + 8t^4(\nu^2 - 1)(\Omega_{C2}^2 + 2\nu - 2) + 1))
\end{aligned}
$$

Second branch

$$
\begin{aligned}
&x_0 = (2(-\Omega_{C2}(10\nu - 4\Omega_{C2}^2\nu + 40\nu t^2 + 14\Omega_{C2}^2 - 3\Omega_{C2}^4 - 76t^2 + 40\Omega_{C2}^2 t^2 - 10)\\
&(-4\Omega_{C2}^4\nu t^2 - \Omega_{C2}^4\nu + 20\Omega_{C2}^4 t^2 + 3\Omega_{C2}^4 - 8\Omega_{C2}^2\nu^2 t^2 + 2\Omega_{C2}^2\nu^2 + 52\Omega_{C2}^2\nu t^2\\
&+9\Omega_{C2}^2\nu - 132\Omega_{C2}^2 t^2 - 11\Omega_{C2}^2 - 144\nu t^2 + 144t^2))^{(}1/2))/(t^2(4\Omega_{C2}^4\nu - 20\Omega_{C2}^4\\
&+8\Omega_{C2}^2\nu^2 - 52\Omega_{C2}^2\nu + 132\Omega_{C2}^2 + 144\nu - 144) - 9\Omega_{C2}^2\nu + \Omega_{C2}^4\nu + 11\Omega_{C2}^2 - 3\Omega_{C2}^4 - 2\Omega_{C2}^2\nu^2)
\end{aligned}
$$

$$
\begin{aligned}
&x_1 = (2\Omega_{C2}^4 t^2 x_0^4 - 30\Omega_{C2}^4 - 16\Omega_{C2}^3\nu t^2 x_0^2 - 4\Omega_{C2}^3\nu x_0^2 + 80\Omega_{C2}^3 t^2 x_0^2 + 12\Omega_{C2}^3 x_0^2 + 8\Omega_{C2}^2\nu^2 t^4 x_0^4\\
&+16\Omega_{C2}^2\nu t^2 x_0^4 + \Omega_{C2}^2{}_0^4 - 24\Omega_{C2}^2\nu - 8\Omega_{C2}^2 t^4 x_0^4 - 40\Omega_{C2}^2 t^2 x_0^4 + 240\Omega_{C2}^2 t^2 - \Omega_{C2}^2 x_0^4 + 84\Omega_{C2}^2\\
&-16\Omega_{C2}\nu^2 t^2 x_0^2 + 4\Omega_{C2}\nu^2 x_0^2 + 104\Omega_{C2}\nu t^2 x_0^2 + 18\Omega_{C2}\nu x_0^2 - 264\Omega_{C2} t^2 x_0^2 - 22\Omega_{C2} x_0^2\\
&+16\nu^3 t^4 x_0^4 - 4\nu^3 t^2 x_0^4 + \nu^3 x_0^4 - 16\nu^2 t^4 x_0^4 + 4\nu^2 t^2 x_0^4 - \nu^2 x_0^4 - 16\nu t^4 x_0^4 - 68\nu t^2 x_0^4 + 80\nu t^2\\
&-\nu x_0^4 + 20\nu + 16t^4 x_0^4 + 68t^2 x_0^4 - 152t^2 + x_0^4 - 20)/(8x_0\Omega_{C2}^4\nu t^2 + 2x_0\Omega_{C2}^4\nu - 40x_0\Omega_{C2}^4 t^2\\
&-6x_0\Omega_{C2}^4 + 16x_0\Omega_{C2}^2\nu^2 t^2 - 4x_0\Omega_{C2}^2\nu^2 - 104x_0\Omega_{C2}^2\nu t^2 - 18x_0\Omega_{C2}^2\nu + 264x_0\Omega_{C2}^2 t^2 + 22x_0\Omega_{C2}^2 + 288x_0\nu t^2 - 288x_0 t^2)
\end{aligned}
$$

Third branch

$$
\begin{aligned}
&x_0 = (2(-\Omega_{C2}(10\nu - 4\Omega_{C2}^2\nu + 40\nu t^2 + 14\Omega_{C2}^2 - 3\Omega_{C2}^4 - 76t^2 + 40\Omega_{C2}^2 t^2 - 10)\\
&(-4\Omega_{C2}^4\nu t^2 - \Omega_{C2}^4\nu + 20\Omega_{C2}^4 t^2 + 3\Omega_{C2}^4 - 8\Omega_{C2}^2\nu^2 t^2 + 2\Omega_{C2}^2\nu^2 + 52\Omega_{C2}^2\nu t^2\\
&+9\Omega_{C2}^2\nu - 132\Omega_{C2}^2 t^2 - 11\Omega_{C2}^2 - 144\nu t^2 + 144t^2))^{(}1/2))/(t^2(4\Omega_{C2}^4\nu - 20\Omega_{C2}^4\\
&+8\Omega_{C2}^2\nu^2 - 52\Omega_{C2}^2\nu + 132\Omega_{C2}^2 + 144\nu - 144) - 9\Omega_{C2}^2\nu + \Omega_{C2}^4\nu + 11\Omega_{C2}^2 - 3\Omega_{C2}^4 - 2\Omega_{C2}^2\nu^2)
\end{aligned}
$$

Appendix B: Expanded equation for flat plate

B

$$
\begin{aligned}
&\Big[\mathrm{D}_w(x)\Big(B(x)\,\mathrm{e}^{\mathrm{I}k_p S(x)}\,k_y^4\,\mathrm{e}^{\mathrm{I}k_y(y-y_0)}\,\mathrm{e}^{-\mathrm{I}\omega t}+\nu\Big(-\Big(\frac{d^2}{dx^2}B(x)\Big)\mathrm{e}^{\mathrm{I}k_p S(x)}\,k_y^2\,\mathrm{e}^{\mathrm{I}k_y(y-y_0)}\,\mathrm{e}^{-\mathrm{I}\omega t}-2\,\mathrm{I}\Big(\frac{d}{dx}B(x)\Big)k_p\Big(\frac{d}{dx}S(x)\Big)\mathrm{e}^{\mathrm{I}k_p S(x)}\,k_y^2\,\mathrm{e}^{\mathrm{I}k_y(y-y_0)}\,\mathrm{e}^{-\mathrm{I}\omega t}-\mathrm{I}\,B(x)\,k_p\Big(\frac{d^2}{dx^2}S(x)\Big)\mathrm{e}^{\mathrm{I}k_p S(x)}\,k_y^2\,\mathrm{e}^{\mathrm{I}k_y(y-y_0)}\,\mathrm{e}^{-\mathrm{I}\omega t}\\
&+B(x)\,k_p^2\Big(\frac{d}{dx}S(x)\Big)^2\mathrm{e}^{\mathrm{I}k_p S(x)}\,k_y^2\,\mathrm{e}^{\mathrm{I}k_y(y-y_0)}\,\mathrm{e}^{-\mathrm{I}\omega t}\Big)\Big)+\Big(\frac{d^2}{dx^2}\mathrm{D}_w(x)\Big)\Big(\Big(\Big(\frac{d^2}{dx^2}B(x)\Big)\mathrm{e}^{\mathrm{I}k_p S(x)}\,\mathrm{e}^{\mathrm{I}k_y(y-y_0)}\,\mathrm{e}^{-\mathrm{I}\omega t}+2\,\mathrm{I}\Big(\frac{d}{dx}B(x)\Big)k_p\Big(\frac{d}{dx}S(x)\Big)\mathrm{e}^{\mathrm{I}k_p S(x)}\,\mathrm{e}^{\mathrm{I}k_y(y-y_0)}\,\mathrm{e}^{-\mathrm{I}\omega t}+\mathrm{I}\,B(x)\,k_p\Big(\frac{d^2}{dx^2}\\
&S(x)\Big)\mathrm{e}^{\mathrm{I}k_p S(x)}\,\mathrm{e}^{\mathrm{I}k_y(y-y_0)}\,\mathrm{e}^{-\mathrm{I}\omega t}-B(x)\,k_p^2\Big(\frac{d}{dx}S(x)\Big)^2\mathrm{e}^{\mathrm{I}k_p S(x)}\,\mathrm{e}^{\mathrm{I}k_y(y-y_0)}\,\mathrm{e}^{-\mathrm{I}\omega t}-\nu\,B(x)\,\mathrm{e}^{\mathrm{I}k_p S(x)}\,k_y^2\,\mathrm{e}^{\mathrm{I}k_y(y-y_0)}\,\mathrm{e}^{-\mathrm{I}\omega t}\Big)+2\Big(\frac{d}{dx}\mathrm{D}_w(x)\Big)\Big(\Big(\Big(\frac{d^3}{dx^3}B(x)\Big)\mathrm{e}^{\mathrm{I}k_p S(x)}\,\mathrm{e}^{\mathrm{I}k_y(y-y_0)}\,\mathrm{e}^{-\mathrm{I}\omega t}+3\,\mathrm{I}\Big(\frac{d^2}{dx^2}B(x)\Big)k_p\Big(\frac{d}{dx}\\
&S(x)\Big)\mathrm{e}^{\mathrm{I}k_p S(x)}\,\mathrm{e}^{\mathrm{I}k_y(y-y_0)}\,\mathrm{e}^{-\mathrm{I}\omega t}+3\,\mathrm{I}\Big(\frac{d}{dx}B(x)\Big)k_p\Big(\frac{d^2}{dx^2}S(x)\Big)\mathrm{e}^{\mathrm{I}k_p S(x)}\,\mathrm{e}^{\mathrm{I}k_y(y-y_0)}\,\mathrm{e}^{-\mathrm{I}\omega t}-3\Big(\frac{d}{dx}B(x)\Big)k_p^2\Big(\frac{d}{dx}S(x)\Big)^2\mathrm{e}^{\mathrm{I}k_p S(x)}\,\mathrm{e}^{\mathrm{I}k_y(y-y_0)}\,\mathrm{e}^{-\mathrm{I}\omega t}+\mathrm{I}\,B(x)\,k_p\Big(\frac{d^3}{dx^3}S(x)\Big)\mathrm{e}^{\mathrm{I}k_p S(x)}\,\mathrm{e}^{\mathrm{I}k_y(y-y_0)}\,\mathrm{e}^{-\mathrm{I}\omega t}\\
&-3\,B(x)\,k_p^2\Big(\frac{d^2}{dx^2}S(x)\Big)\Big(\frac{d}{dx}S(x)\Big)\mathrm{e}^{\mathrm{I}k_p S(x)}\,\mathrm{e}^{\mathrm{I}k_y(y-y_0)}\,\mathrm{e}^{-\mathrm{I}\omega t}-\mathrm{I}\,B(x)\,k_p^3\Big(\frac{d}{dx}S(x)\Big)^3\mathrm{e}^{\mathrm{I}k_p S(x)}\,\mathrm{e}^{\mathrm{I}k_y(y-y_0)}\,\mathrm{e}^{-\mathrm{I}\omega t}-\nu\Big(\frac{d}{dx}B(x)\Big)\mathrm{e}^{\mathrm{I}k_p S(x)}\,k_y^2\,\mathrm{e}^{\mathrm{I}k_y(y-y_0)}\,\mathrm{e}^{-\mathrm{I}\omega t}-\mathrm{I}\,\nu\,B(x)\,k_p\Big(\frac{d}{dx}S(x)\Big)\mathrm{e}^{\mathrm{I}k_p S(x)}\,k_y^2\,\mathrm{e}^{\mathrm{I}k_y(y-y_0)}\,\mathrm{e}^{-\mathrm{I}\omega t}\Big)\\
&+\mathrm{D}_w(x)\Big(\Big(\Big(\frac{d^4}{dx^4}B(x)\Big)\mathrm{e}^{\mathrm{I}k_p S(x)}\,\mathrm{e}^{\mathrm{I}k_y(y-y_0)}\,\mathrm{e}^{-\mathrm{I}\omega t}+\mathrm{I}\,B(x)\,k_p\Big(\frac{d^4}{dx^4}S(x)\Big)\mathrm{e}^{\mathrm{I}k_p S(x)}\,\mathrm{e}^{\mathrm{I}k_y(y-y_0)}\,\mathrm{e}^{-\mathrm{I}\omega t}-\mathrm{I}\,\nu\,B(x)\,k_p\Big(\frac{d^2}{dx^2}S(x)\Big)\mathrm{e}^{\mathrm{I}k_p S(x)}\,k_y^2\,\mathrm{e}^{\mathrm{I}k_y(y-y_0)}\,\mathrm{e}^{-\mathrm{I}\omega t}+B(x)\,k_p^4\Big(\frac{d}{dx}S(x)\Big)^4\mathrm{e}^{\mathrm{I}k_p S(x)}\,\mathrm{e}^{\mathrm{I}k_y(y-y_0)}\,\mathrm{e}^{-\mathrm{I}\omega t}\\
&+4\,\mathrm{I}\Big(\frac{d^3}{dx^3}B(x)\Big)k_p\Big(\frac{d}{dx}S(x)\Big)\mathrm{e}^{\mathrm{I}k_p S(x)}\,\mathrm{e}^{\mathrm{I}k_y(y-y_0)}\,\mathrm{e}^{-\mathrm{I}\omega t}-2\,\mathrm{I}\,\nu\Big(\frac{d}{dx}B(x)\Big)k_p\Big(\frac{d}{dx}S(x)\Big)\mathrm{e}^{\mathrm{I}k_p S(x)}\,k_y^2\,\mathrm{e}^{\mathrm{I}k_y(y-y_0)}\,\mathrm{e}^{-\mathrm{I}\omega t}+4\,\mathrm{I}\Big(\frac{d}{dx}B(x)\Big)k_p\Big(\frac{d^3}{dx^3}S(x)\Big)\mathrm{e}^{\mathrm{I}k_p S(x)}\,\mathrm{e}^{\mathrm{I}k_y(y-y_0)}\,\mathrm{e}^{-\mathrm{I}\omega t}-6\,\mathrm{I}\,B(x)\,k_p^3\Big(\frac{d}{dx}\\
&S(x)\Big)^2\mathrm{e}^{\mathrm{I}k_p S(x)}\,\mathrm{e}^{\mathrm{I}k_y(y-y_0)}\,\mathrm{e}^{-\mathrm{I}\omega t}\Big(\frac{d^2}{dx^2}S(x)\Big)-12\Big(\frac{d}{dx}B(x)\Big)k_p^2\Big(\frac{d^2}{dx^2}S(x)\Big)\Big(\frac{d}{dx}S(x)\Big)\mathrm{e}^{\mathrm{I}k_p S(x)}\,\mathrm{e}^{\mathrm{I}k_y(y-y_0)}\,\mathrm{e}^{-\mathrm{I}\omega t}-4\,\mathrm{I}\Big(\frac{d}{dx}B(x)\Big)k_p^3\Big(\frac{d}{dx}S(x)\Big)^3\mathrm{e}^{\mathrm{I}k_p S(x)}\,\mathrm{e}^{\mathrm{I}k_y(y-y_0)}\,\mathrm{e}^{-\mathrm{I}\omega t}-4\,B(x)\,k_p^2\Big(\frac{d^3}{dx^3}S(x)\Big)\Big(\frac{d}{dx}\\
&S(x)\Big)\mathrm{e}^{\mathrm{I}k_p S(x)}\,\mathrm{e}^{\mathrm{I}k_y(y-y_0)}\,\mathrm{e}^{-\mathrm{I}\omega t}-3\,B(x)\,k_p^2\Big(\frac{d^2}{dx^2}S(x)\Big)^2\mathrm{e}^{\mathrm{I}k_p S(x)}\,\mathrm{e}^{\mathrm{I}k_y(y-y_0)}\,\mathrm{e}^{-\mathrm{I}\omega t}-6\Big(\frac{d^2}{dx^2}B(x)\Big)k_p^2\Big(\frac{d}{dx}S(x)\Big)^2\mathrm{e}^{\mathrm{I}k_p S(x)}\,\mathrm{e}^{\mathrm{I}k_y(y-y_0)}\,\mathrm{e}^{-\mathrm{I}\omega t}-\nu\Big(\frac{d^2}{dx^2}B(x)\Big)\mathrm{e}^{\mathrm{I}k_p S(x)}\,k_y^2\,\mathrm{e}^{\mathrm{I}k_y(y-y_0)}\,\mathrm{e}^{-\mathrm{I}\omega t}+\nu\,B(x)\,k_p^2\Big(\frac{d}{dx}\\
&S(x)\Big)^2\mathrm{e}^{\mathrm{I}k_p S(x)}\,k_y^2\,\mathrm{e}^{\mathrm{I}k_y(y-y_0)}\,\mathrm{e}^{-\mathrm{I}\omega t}+6\,\mathrm{I}\Big(\frac{d^2}{dx^2}B(x)\Big)k_p\Big(\frac{d^2}{dx^2}S(x)\Big)\mathrm{e}^{\mathrm{I}k_p S(x)}\,\mathrm{e}^{\mathrm{I}k_y(y-y_0)}\,\mathrm{e}^{-\mathrm{I}\omega t}\Big)\Big]+2\,(1-\nu)\Big[\Big(\frac{d}{dx}\mathrm{D}_w(x)\Big)\Big(-\Big(\frac{d}{dx}B(x)\Big)\mathrm{e}^{\mathrm{I}k_p S(x)}\,k_y^2\,\mathrm{e}^{\mathrm{I}k_y(y-y_0)}\,\mathrm{e}^{-\mathrm{I}\omega t}-\mathrm{I}\,B(x)\,k_p\Big(\frac{d}{dx}\\
&S(x)\Big)\mathrm{e}^{\mathrm{I}k_p S(x)}\,k_y^2\,\mathrm{e}^{\mathrm{I}k_y(y-y_0)}\,\mathrm{e}^{-\mathrm{I}\omega t}\Big)+\mathrm{D}_w(x)\Big(-\Big(\frac{d^2}{dx^2}B(x)\Big)\mathrm{e}^{\mathrm{I}k_p S(x)}\,k_y^2\,\mathrm{e}^{\mathrm{I}k_y(y-y_0)}\,\mathrm{e}^{-\mathrm{I}\omega t}-2\,\mathrm{I}\Big(\frac{d}{dx}B(x)\Big)k_p\Big(\frac{d}{dx}S(x)\Big)\mathrm{e}^{\mathrm{I}k_p S(x)}\,k_y^2\,\mathrm{e}^{\mathrm{I}k_y(y-y_0)}\,\mathrm{e}^{-\mathrm{I}\omega t}-\mathrm{I}\,B(x)\,k_p\Big(\frac{d^2}{dx^2}S(x)\Big)\mathrm{e}^{\mathrm{I}k_p S(x)}\,k_y^2\,\mathrm{e}^{\mathrm{I}k_y(y-y_0)}\,\mathrm{e}^{-\mathrm{I}\omega t}\\
&+B(x)\,k_p^2\Big(\frac{d}{dx}S(x)\Big)^2\mathrm{e}^{\mathrm{I}k_p S(x)}\,k_y^2\,\mathrm{e}^{\mathrm{I}k_y(y-y_0)}\,\mathrm{e}^{-\mathrm{I}\omega t}\Big)\Big]-\rho_w\,h_w\,B(x)\,\mathrm{e}^{\mathrm{I}k_p S(x)}\,\mathrm{e}^{\mathrm{I}k_y(y-y_0)}\,\omega^2\,\mathrm{e}^{-\mathrm{I}\omega t}=0
\end{aligned}
$$

Appendix C: 3D plots of dispersion branches m = 0

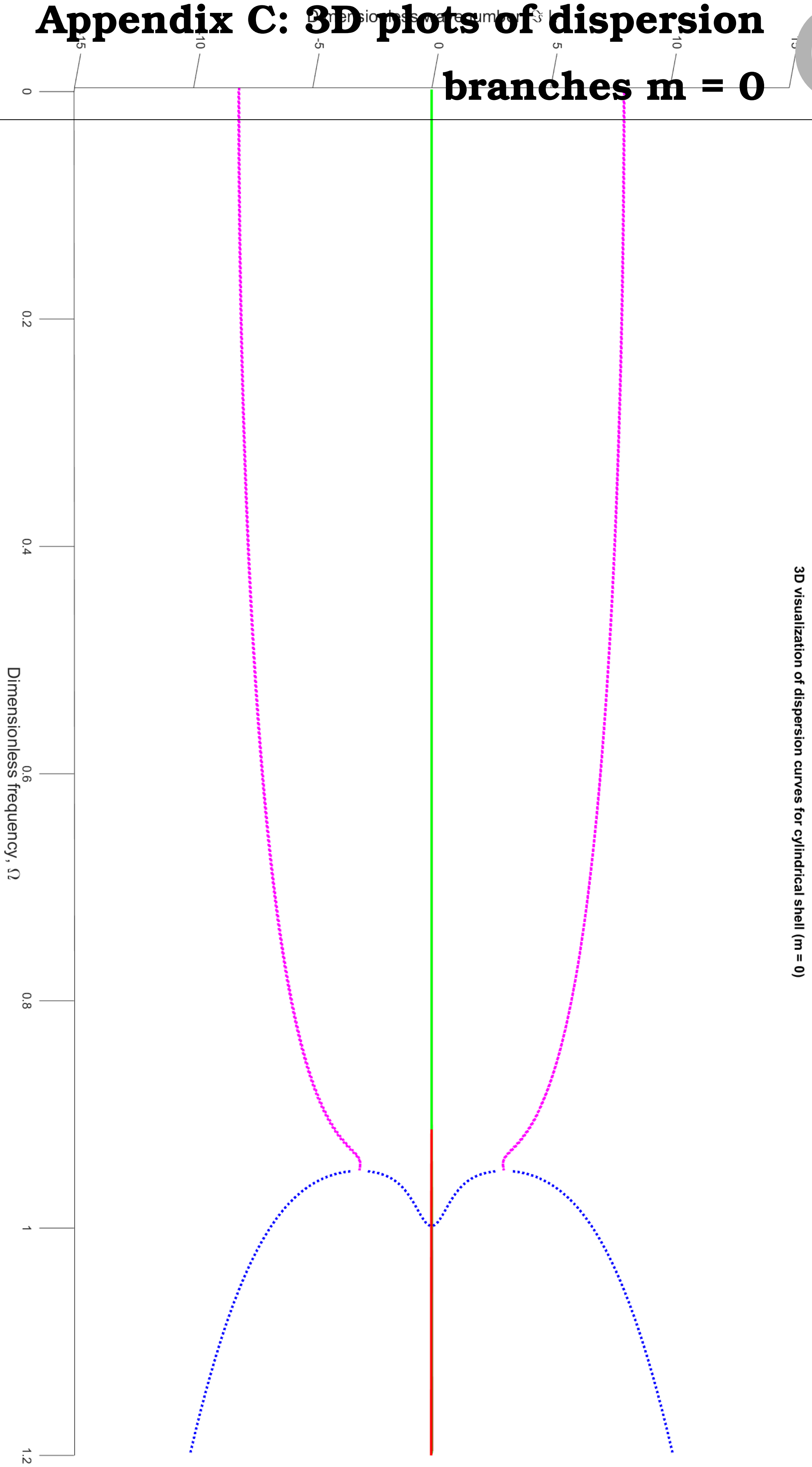

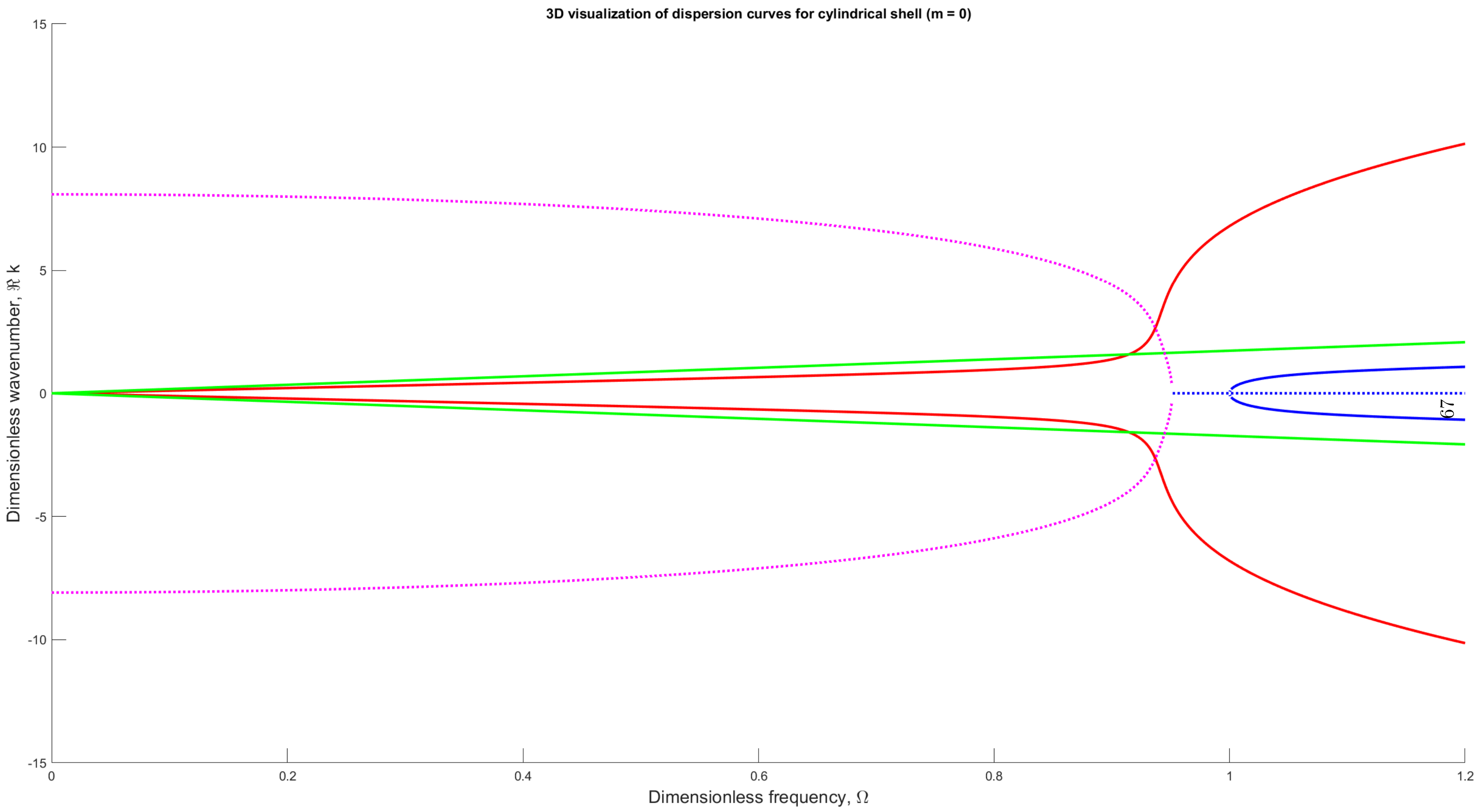
3D visualization of dispersion curves for cylindrical shell (m = 0)
Dimensionless wavenumber, ℜ k
Dimensionless frequency, Ω
15
10
5
0
-5
-10
-15
0
0.2
0.4
0.6
0.8
1
1.2

3D visualization of dispersion curves for cylindrical shell (m = 0)

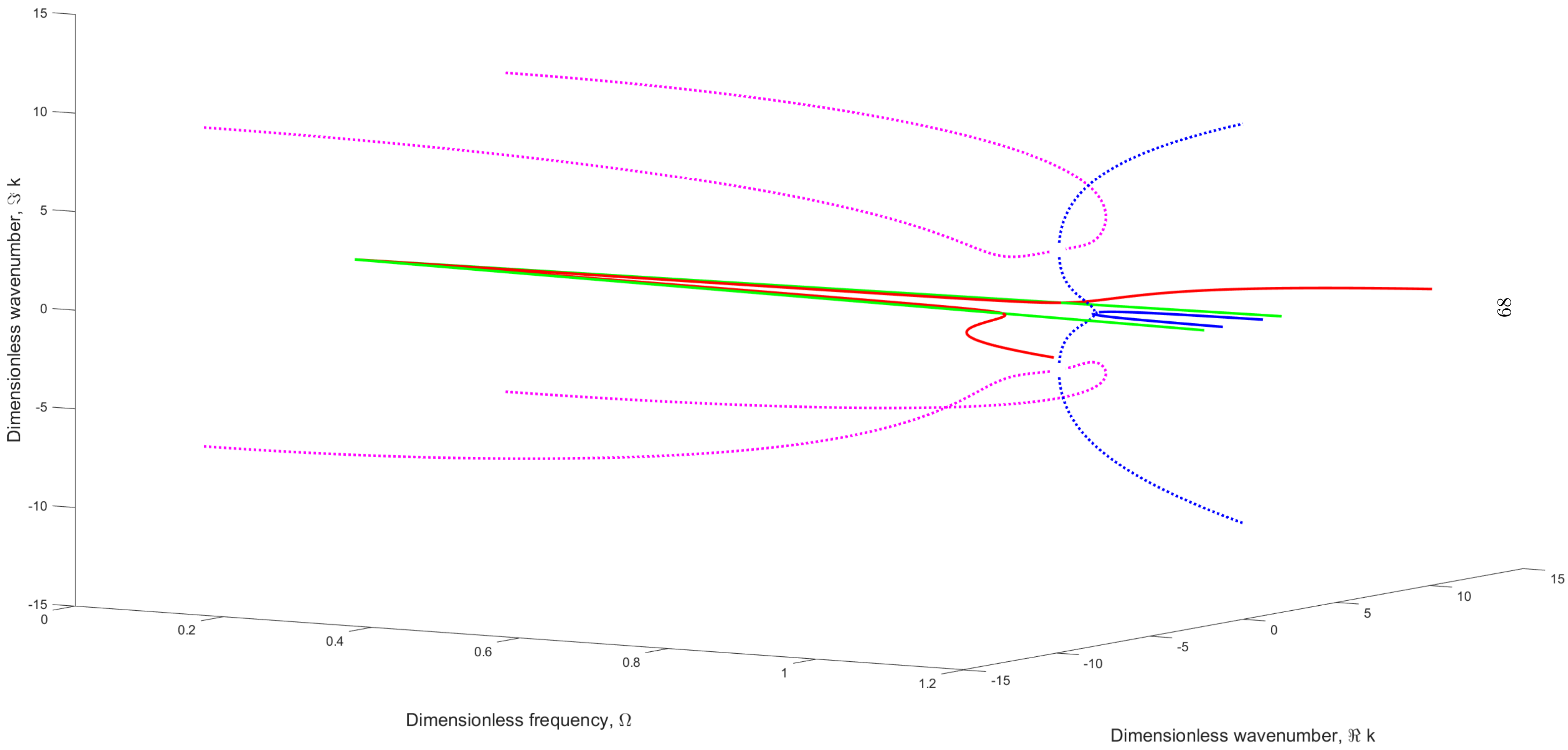

Appendix D: Low frequency solution for circumferential waves

The low-frequency solution for the circumferential traveling waves is first obtained for the first purely real branch starting from $(\Omega, m') = (0, 0.5)$. The expansion will be performed around Ω as (D.1), and as the branch starts from a non-zero wave number value, p_0 will be set to zero.

$$\bar{m}' = \sum_{i=0}^{p} x_i \Omega^{p_i} \tag{D.1}$$

Setting $p_0 = 0$ lets one determine the first constant x_0, by balancing terms at the $\mathcal{O}(\Omega^0)$ order. The first term is written out as (D.2) but is not plotted against the numerical solution as it is simply a constant.

$$x_0 = \frac{\theta_0}{\pi} \tag{D.2}$$

The second constant, x_1, is found by setting $p_1 = 1$, and balancing terms at the $\mathcal{O}(\Omega^2)$ order. x_1 is written out as (D.3), and is plotted against the numerical solution in Figure D.1

$$x_1 = \frac{\sqrt{2}\,\theta_0\,\sqrt{t^2+1}}{2\,t\,\pi} \tag{D.3}$$

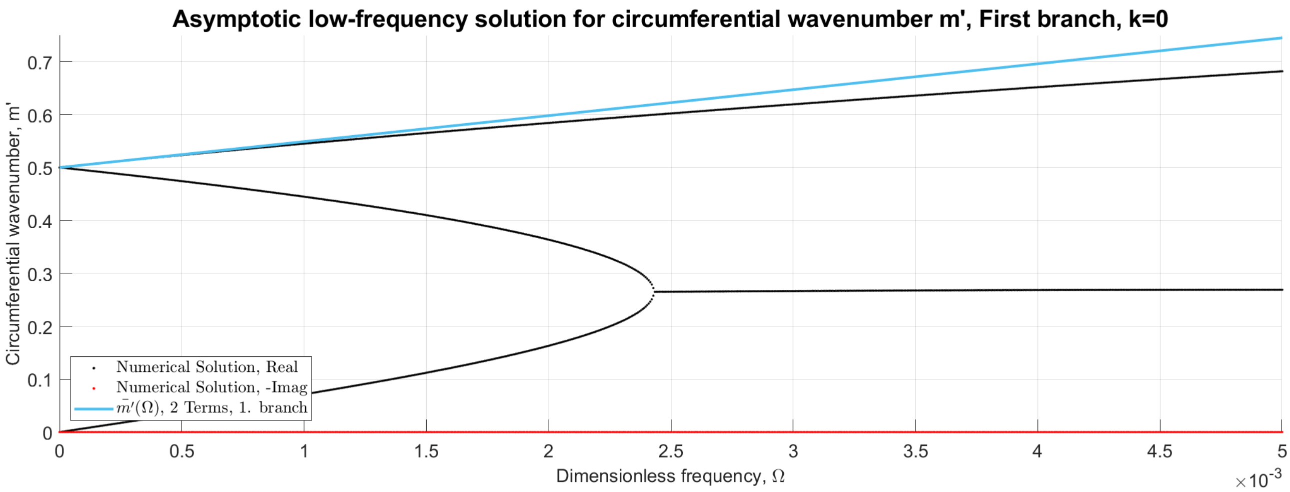

Figure D.1: Low-frequency asymptotic solution for circumferential wave numbers m', first branch, 2 terms.

The third constant, x_2, is found by setting $p_2 = 2$, and balancing terms at the $\mathcal{O}(\Omega^4)$ order. x_2 is written out as (D.4), and is plotted against the numerical solution in Figure D.2.

$$x_2 = -\frac{\theta_0}{2\,\pi\,t^2} \tag{D.4}$$

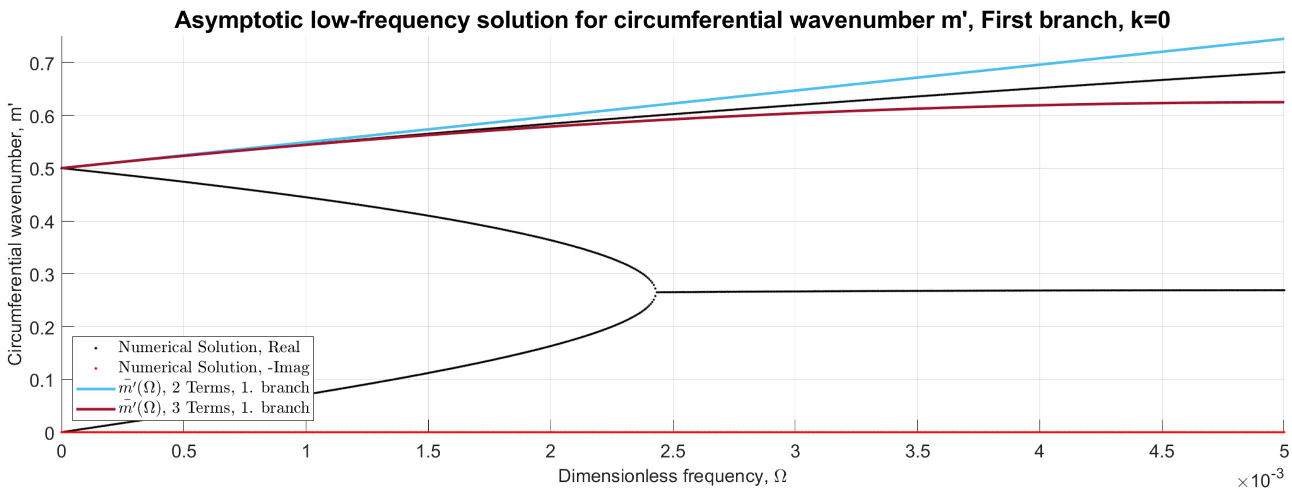

Figure D.2: Low-frequency asymptotic solution for circumferential wave numbers m', first branch, 3 terms.

The asymptotic approximation for the first branch in the low-frequency range is then given as (D.5).

$$\bar{m}' = \frac{\theta_0}{\pi} - \frac{\Omega^2\,\theta_0}{2\,t^2\,\pi} + \frac{\sqrt{2}\,\Omega\,\theta_0\,\sqrt{t^2+1}}{2\,t\,\pi} \tag{D.5}$$

The low-frequency solution for the second branch is obtained from an expansion around an offset Ω-value as (D.6), where Ω_C is the cut-on frequency of the given branch. The cut-on frequency is determined by solving the dispersion equation for values of Ω, when $m' = 0$. Only one real positive root exists, which is constant $\Omega_C = 1$.

$$\bar{m}' = \sum_{i=0}^{p} x_i(\Omega - \Omega_C)^{p_i} \tag{D.6}$$

The first term, x_0, is found by setting $p_0 = 1/2$, and balancing terms at the $\mathcal{O}(\Omega^1)$ order. x_0 is written out as (D.7), and is plotted against the numerical solution in Figure D.3.

$$x_0 = \frac{\sqrt{2}\,\theta_0}{\pi} \tag{D.7}$$

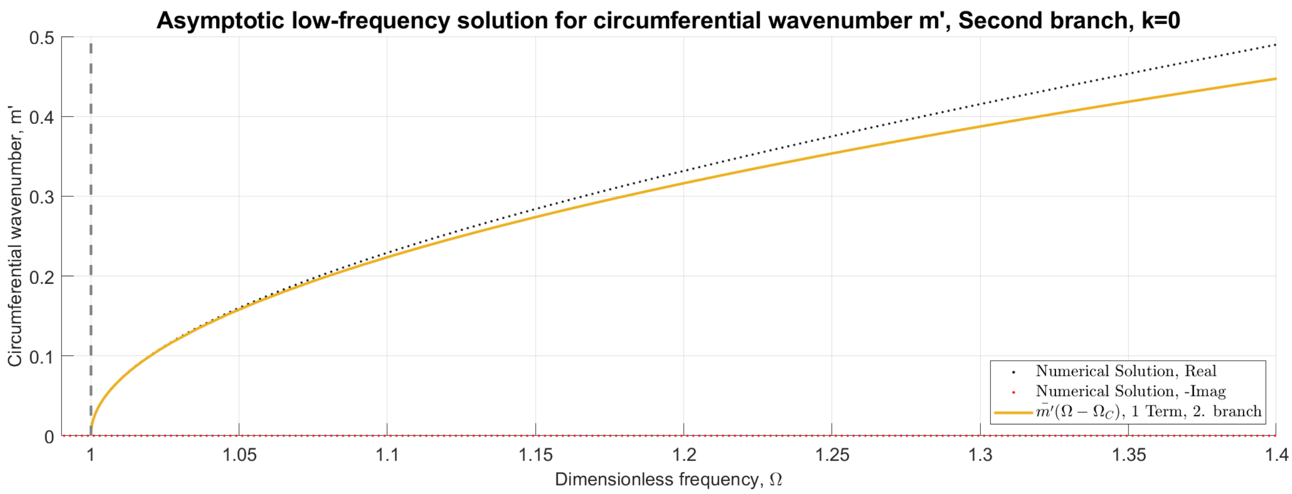

Figure D.3: Low-frequency asymptotic solution for circumferential wave numbers m', second branch, 1 term.

The second term, x_1, is found by setting $p_1 = 3/2$, and balancing terms at the $\mathcal{O}(\Omega^2)$ order. x_1 is written out as (D.8), and is plotted against the numerical solution in Figure D.4.

$$x_1 = -\frac{\sqrt{2}\,\theta_0\,\left(16\,\pi^4\,t^2 - \pi^4\right)}{4\,\pi^5} \tag{D.8}$$

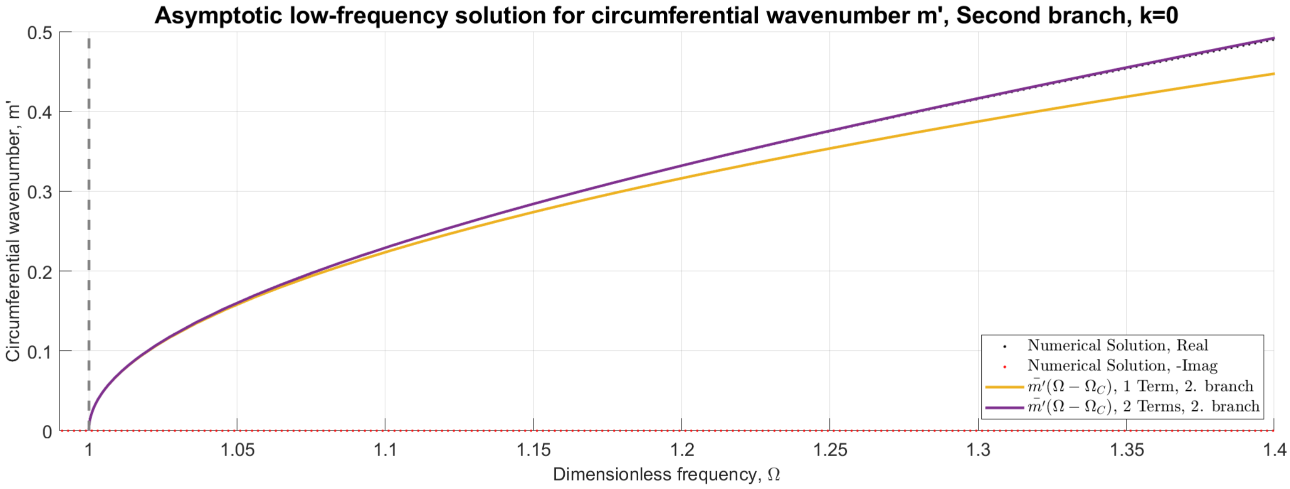

Figure D.4: Low-frequency asymptotic solution for circumferential wave numbers m', second branch, 2 terms.

The asymptotic approximation for the second branch in the low-frequency range is then given as (D.9).

$$\bar{m}' = \Omega^{1/2}\,\frac{\sqrt{2}\,\theta_0}{\pi} - \Omega^{3/2}\,\frac{\sqrt{2}\,\theta_0\,\left(16\,t^2 - 1\right)}{4\,\pi} \tag{D.9}$$

Appendix E: A short note on the scaling approach

E

In Chapter 5, a frequency scaling approach was employed to obtain an asymptotic solution for the high-frequency regime of the dispersion branches. Little effort was put into explaining the method, and this appendix will (hopefully) serve as an explanation of the method, and provide some intuition on the underlying ideas.

When we want to study bacteria we grab our microscope, and when we want to study the moon we grab a telescope. In much the same way, when we wish to study a part of an equation which is very small or very large, we need to "grab the correct scope". This is done thru appropriate re-scaling of the problem. In general, the idea is to recast the equation in terms of cleverly scaled coordinates, so that the parts of the equation that are of most interest to us, are presented in the greatest detail.

The explanation will take point of departure in a simple equation, to simplify the calculations. The equation in question will be (E.1), which can be seen plotted in the range $x \in [0, 5]$ in Figure E.1 for $\epsilon = 0.1$.

$$f(x) = -x^{-3} + 2x^{-2} - \epsilon x \tag{E.1}$$

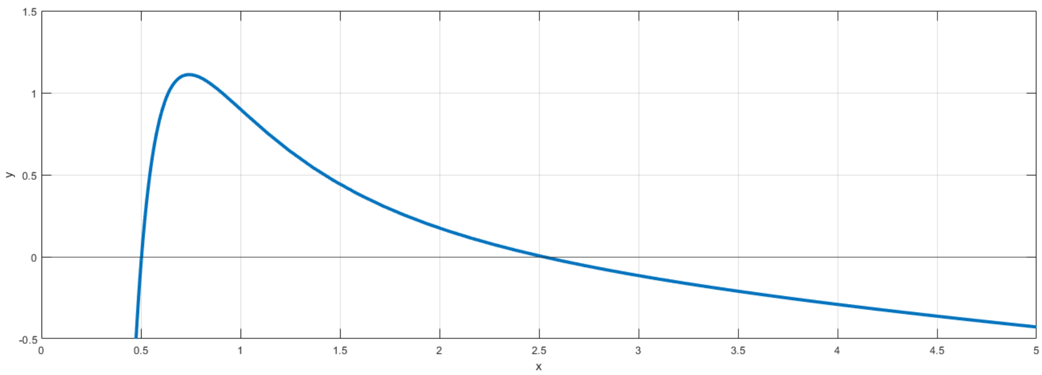

Figure E.1: Equation (E.1) plotted for $\epsilon = 0.1$.

From a simple investigation of the figure and equation, it becomes apparent how different regions of the graph are dominated by different terms in the equation. Around $x = 0$, the first term dominates, as this term will be numerically large compared with the other terms. It is also apparent how the graph has a large positive slope, which matches with the term $-x^{-3}$. At $x = 0.5$, the second term starts to become the largest term in the equation, and as a result, the graph starts to attain a negative slope at around $x = 0.7$. Then at $x = \frac{2}{\epsilon}^{1/3}$, the third term starts to dominate the equation. It can be seen how the graph seems to have a linear tendency with increasing x, which matches the linearity of the third term.

Let us attempt to use asymptotic analysis to find the roots of the equation. As usual, an expansion parameter is identified which is comparably small to the other parameters in the equation. Using ϵ as the expansion parameter, an expansion is proposed starting from $\epsilon = 0$. Employing this expansion gives (E.2), which shows us that an approximation of a root can be found by balancing the two first terms, which were seen to dominate the equation in the lower range of x. In this range, the third term of the equation is quite small, and can reasonably be neglected without a huge loss of accuracy. In fact, the approximation has a root at $x = 0.5$, and Looking at the graph it can be seen how this solution is fairly accurate. For $\epsilon = 0.1$, the solution is off by less than 0.7%. If more terms are included in the series, the accuracy of the solution should be expected to go up, and an increasingly good approximation of the root around $x = 0.5$ is found. However, at no point will the approximation yield information on the second root around $x = 2.5$ (See Figure E.1). Another approach must therefore be employed to obtain an approximation for this second root.

$$f(x) = -x^{-3} + 2x^{-2} \tag{E.2}$$

From (E.2) an approximate root was obtained by balancing two terms which dominated the equation in the lower range of x. Unsurprisingly this yielded an expression for the root located around the same range. In the low range of x, the first two terms were large compared with the third term, and so one could reasonably neglect the third term from the equation. However, as x increases, the first two terms decrease, and so for larger values of x, one cannot neglect the contribution of the third term anymore. If one wishes to obtain an approximation for the root around $x = 2.5$, one must balance terms which dominate the equation in that range of x. Returning to (E.1), it can be seen how the second and third terms may be good candidates for such a balance. At around $x = 2.5$, the first term will be an order of magnitude smaller than the remaining two terms, and so it will contribute very little to the location of the root. To see in a more rigorous sense, why the second and third terms should be balanced, we exploit a scaling approach. The idea is to express the equation in terms of new and re-scaled coordinated X and $F(X)$

For the second and third terms to balance each other, it can be seen how x must be around the order of $\epsilon^{-1/3}$. This would similarly result in $f(x)$ being of order ϵ^2. Based on this information, a scaling is proposed as (E.3).

$$x = \epsilon^{-1/3} X; \qquad\qquad f(x) = \epsilon^2 F(X) \tag{E.3}$$

Substituting this scaling into (E.1), the re-scaled equation is obtained as (E.4).

$$F(X) = \epsilon^{-1} X^{-3} + 2X^{-2} \epsilon^{-4/3} - X \epsilon^{-4/3} \tag{E.4}$$

Now it can be seen, how for small values of ϵ, the second and third terms in the re-scaled equation are much larger than the first term, and so it is obvious that the balance should occur between those two. This gives (E.5) when one returns to the original coordinates, x and $f(x)$. This approximation has a root at $x = 20^{1/3} \approx 2.71$ for $\epsilon = 0.1$, which is seen to be a fair approximation to the exact root at $x = 2.52$.

$$F(x) \approx 2X^{-2} \epsilon^{-4/3} - X \epsilon^{-4/3} \rightarrow f(x) \approx 2x^{-2} - \epsilon x \tag{E.5}$$

The presented example was simple enough to see that the balance should be made between the second and third terms to obtain the approximation for the second root. One can however easily imagine a scenario, where the equation is too elaborate for this sort of direct and manual identification of appropriate terms for the balance. Imagine e.g. the dispersion equation for the cylindrical shell investigated in Chapter 5. We knew nothing about which terms dominated in which frequency-ranges, or even how many terms should be included in the balancing. We did however know something about the nature of the solution, as we knew the flexural wave numbers to be approximately proportional to the frequency thru $k \simeq \sqrt{\Omega}$. This allowed an appropriate scaling of the equation to be employed, which yielded an asymptotic approximation of the flexural wave numbers with very little effort.